UNIVERSITY OF CALIFORNIA, SAN DIEGO

Two Dimensional Materials for Sensing and Energy Applications

A dissertation submitted in partial satisfaction of the requirements

for the degree Doctor of Philosophy

in

Materials Science and Engineering

by

Cihan Kuru

Committee in charge:

Prabhakar R. Bandaru, Chair
Gaurav Arya
Renkun Chen
Vlado A. Lubarda
Jie Xiang

2015

The dissertation of Cihan Kuru is approved, and it is acceptable in quality and form for publication on microfilm and electronically:

Chair

University of California, San Diego

2015

DEDICATION

Dedicated to

my parents, Rahim Kuru and Cevher Kuru

TABLE OF CONTENTS

LIST OF FIGURES

LIST OF TABLES

ACKNOWLEDGEMENTS

I would like to acknowledge and thank my current advisor Professor Prabhakar R. Bandaru and my previous advisor Professor Sungho Jin for their guidance and support during the course of my PhD studies. I would like to thank the committee members for their helpful comments and suggestions. I also would like to acknowledge and thank the following individuals for their help and contributions to this study: Chulmin Choi, Serdar Yavuz, Duyoung Choi, Alireza Kargar, Eric Martinez, Cyrus Rustomji, Teak Young Kim, Chin Hung Liu, Young Jin Kim, Gunwoo Kim, Joon Lee and Michael Hwang.

Chapter 1, in part, has been published in Journal of Nanoscience and Nanotechnology in 2015 by Cihan Kuru, Duyoung Choi, Chulmin Choi, Young Jin Kim and Sungho Jin. The dissertation/thesis author was the primary investigator and author of this paper.

Chapter 2, in part, has been published in Advanced Science in 2015 by Cihan Kuru, Chulmin Choi, Alireza Kargar, Duyoung Choi, Young Jin Kim, Chin Hung Liu, Serdar Yavuz and Sungho Jin. Chapter 2, in part, has been submitted to Nanotechnology by Cihan Kuru, Duyoung Choi, Alireza Kargar, Chin Hung Liu, Serdar Yavuz, Edward Choi, Sungho Jin and Prabhakar R. Bandaru. The dissertation/thesis author was the primary investigator and author of these papers.

Chapter 3, in part, has been accepted for publication in Journal of Nanoscience and Nanotechnology. Cihan Kuru, Serdar Yavuz, Alireza Kargar, Duyoung Choi, Chulmin Choi, Cyrus Rustomji, Sungho Jin and Prabhakar R. Bandaru. The dissertation/thesis author was the primary investigator and author of this paper.

VITA

2007 Bachelor of Science, Balikesir University

2011 Master of Science, University of California, San Diego

2015 Doctor of Philosophy, University of California, San Diego

PUBLICATIONS

- C. Kuru**,** C. Choi, A. Kargar, D. Choi, Y. J. Kim, C. H. Liu, S. Yavuz and S. Jin. MoS_2 Nanosheet–Pd Nanoparticle Composite for Highly Sensitive Room Temperature Detection of Hydrogen. *Advanced Science,* 2015, **2**, 4.

- C. Kuru, D. Choi, C. Choi, Y. J. Kim, S. Jin. Palladium Decorated Graphene-Nanoribbon Network for Enhanced Gas Sensing. *Journal of Nanoscience and Nanotechnology,* 2015, **15**, 2464.

- C. Kuru, S. Yavuz, A. Kargar, D. Choi, C. Choi, C. Rustomji, S. Jin, P. Bandaru. Enhanced Power Conversion Efficiency of Graphene/Silicon Heterojunction Solar Cells Through NiO Induced Doping. *Journal of Nanoscience and Nanotechnology,* in press.

- C. Kuru, D. Choi, A. Kargar, C. H. Liu, S. Yavuz, C. Choi, S. Jin, P. R. Bandaru. High-Performance Flexible Hydrogen Sensor Made of WS_2 Nanosheet-Pd Nanoparticle Composite Film. *Nanotechnology,* submitted.

- D. Choi, C. Kuru, C. Choi, K. Noh, S. K. Hong, S. Das, W. Choi, S. Jin. Nanopatterned Graphene Field Effect Transistor Fabricated Using Block Co-polymer Lithography. *Materials Research Letters,* 2014, **2**, 131.

- D. Choi, C. Kuru, C. Choi, K. Noh, S. K. Hong, S. Das, W. Choi, S. Jin. Unusually High Optical Transparency in Hexagonal Nano-Patterned Graphene with Enhanced Conductivity by Chemical Doping. *Small,* 2015, **11**, 3143.

- D. Choi, C. Kuru, Y. Kim, G. Kim, T. Kim, R. Chen and S. Jin. Uniformly Nanopatterned Graphene Field-Effect Transistors with Enhanced Properties**.** *Nanoscale Research Letters,* 2015, **10**, 1.

- C. Choi, K. Noh, C. Kuru, L. H. Chen, T. Y. Seong, S. Jin. Fabrication of Patterned Magnetic Nanomaterials for Data Storage Media. *Journal of the Minerals, Metals & Materials Society,* 2012, **64**, 1165.

ABSTRACT OF THE DISSERTATION

Two Dimensional Materials for Sensing and Energy Applications

by

Cihan Kuru

Doctor of Philosophy in Materials Science and Engineering

University of California, San Diego, 2015

Professor Prabhakar R. Bandaru, Chair

Since the discovery of graphene in 2004, two dimensional materials (2D) have become the focus of tremendous research owing to their unprecedented properties. Atomically thin nature of 2D materials gives rise to unique physicochemical properties, which makes them attractive for flexible electronics, chemical and biological sensing, energy storage, and solar cells. In this dissertation, sensing and energy related applications of 2D materials are studied.

In chapter 1, graphene based ammonia sensors are presented, in which nano-structuring graphene significantly improves the sensitivity towards ammonia due to the formation of highly reactive edge defects. It was found that sensitivity could be further enhanced by decoration of Pd nanoparticles on the nano-structured graphene.

In chapter 2, hydrogen sensors based on solution processed transition metal dichalcogenides (TMDs) nanosheets-Pd nanoparticles composites are introduced. The sensors can detect hydrogen at room temperature with high sensitivities. The ease of fabrication holds a great potential for low-cost and scalable manufacturing of chemical sensors.

In chapter 3, the fabrication and characterization of graphene/Si heterojunction solar cells are described and various methods to improve the power conversion efficiency (PCE) are presented. A single layer graphene is highly transparent; therefore suitable as a transparent Schottky electrode for solar cells. However, the PCEs of the pristine graphene/Si solar cells are low due to the high sheet resistance of graphene as well as the low Schottky barrier height between pristine graphene and Si. We improved the PCE by a magnitude of order (achieving 9% PCE) with Au nanoparticle decoration followed by a nitric acid treatment owing to the dramatic reduction in the series resistance of the cells and the enhanced Schottky barrier height. Furthermore, we used NiO as a transparent and stable hole doping material for graphene, in which NiO doped cell shows enhanced PCE with high stability.

In chapter 4, MoS_2 nanosheet-Ru nanoparticle composite is introduced as a highly efficient catalyst for hydrogen evolution reaction. The MoS_2-Ru composite shows much smaller onset potential and Tafel slope compared to pristine MoS_2 nanosheets indicating its superior catalytic performance for hydrogen evolution. The fabrication and characterization of the composite is described and its enhanced catalytic performance is discussed.

CHAPTER 1: GRAPHENE BASED AMMONIA SENSORS

1.1 Introduction

Graphene, two dimensional (2D) hexagonally arranged carbon atoms, has drawn tremendous attention owing to its exceptional electronic, optical and mechanical properties [1-3]. The energy band structure of graphene has a linear dispersion implying that electrons in graphene behave as massless fermions and the valance and conduction bands touch in k-space indicating that graphene is a zero band gap material [4, 5]. The electronic mobilities of graphene in excess of 200,000 $cm^2V^{-1}s^{-1}$ have been achieved, which makes it desirable for next generation electronic devices [6-8]. However, its zero band gap nature hinders its application to digital devices. In order to circumvent this problem graphene nano-structures such as graphene nanoribbons and nanomesh have been realized [9, 10]. When graphene is patterned into narrow nanostructures, a band gap is opened due to the quantum confinement effect providing high on/off current ratios and low off state current, which are required for digital electronics [11, 12]. Even though a band gap is introduced through graphene nano-patterning, high mobility of graphene is diminished due to the excess amount of edge defects formed during the fabrication of graphene nano-structures [13, 14]. Fabricating graphene field effect transistors (FET) with high on/off ratio and mobility still remains as a challenge.

Graphene can be produced by mechanical exfoliation technique using a piece of scotch tape, which results in single crystalline, micron sized graphene flakes [15-17]. Reina *at all* have developed a technique to grow graphene on nickel films by Chemical Vapor Deposition (CVD) and were able to transfer it onto arbitrary substrates [18].

This method provides large area, multilayer graphene sheets with a polycrystalline structure. Later on, single layer graphene has been successfully grown on copper foils by taking advantage of low carbon solubility of copper, which impedes multilayer graphene growth [19]. Furthermore, chemical exfoliation methods have been developed in order to produce graphene flakes. Hummers method has been widely used, in which bulk graphite is oxidized by strong oxidizers resulting in an increased interlayer spacing of graphite [20]. After mild sonication in water, bulk graphite oxide can be readily exfoliated to aqueous suspensions of graphene oxide flakes, which then can be reduced to graphene by hydrazine exposure or thermal annealing [21, 22]. On the other hand, lithium intercalation, solvent assisted exfoliation and electrochemical exfoliation methods have been used to produce colloidal graphene dispersions, which results in higher quality graphene flakes [23-25].

Graphene is of great interest for the development of chemical sensors owing to its high surface-to-volume ratio, which enables high sensitivity. The most widely utilized gas detection mechanism of graphene is based on the conductance change due to the adsorbed gas molecules, which can either dope graphene or change the mobility of charge carriers [26, 27]. Since the conductivity depends on both the concentration of charge carriers and mobility, a change of either one results in variations of conductivity. Pristine graphene gas sensors have been used to detect toxic gas species such as ammonia and nitrogen dioxide, in which an increase of conductivity was observed when exposed to nitrogen dioxide (NO_2) and a decrease of conductivity when exposed to ammonia (NH_3) [28-30]. Since graphene is initially p-doped due to the adsorbed oxygen molecules in air, exposure to electron-withdrawing NO_2 molecules increases the number of hole carriers in

graphene increasing the conductivity while electron-donating NH_3 molecules depletes the hole carriers resulting in a decrease of conductivity. Meanwhile, gas sensors utilizing reduced graphene oxide (RGO) have been widely studied. It has been reported that defective structure of RGO and the remaining functional groups such as carboxylic acid, epoxy and alcohol groups promote adsorption of gas species making RGO a promising candidate for chemical sensing [31-34]. RGO is also advantageous in terms of easy fabrication, scalability, low cost and ability to tune its electrical properties. Decorating graphene with metal nanoparticles is an efficient method to enhance gas sensitivity and selectivity. For example, palladium (Pd) doped graphene sheets have been used for the detection of hydrogen, in which reversible formation of palladium hydride compounds provides a selective sensing mechanism [35, 36]. Besides, graphene/metal oxide hybrids have been developed in order to eliminate high operation temperature of metal oxide sensors, in which metal oxide nanoparticles serve as the adsorption sites for gas species while graphene provides good electrical conductivity [37, 38]. Moreover, three dimensional graphene structures such as graphene nanowalls and graphene foam have been used to build gas sensors, in which increased surface area leads to enhanced sensitivity [39, 40]. Furthermore, it was reported that nano-patterned graphene is an ideal sensing platform due to the presence of active adsorption sites for gas species [41]. Paul *et all* was able to detect NO_2 and NH_3 using graphene nanomesh with detection limits of 15 ppb and 160 ppb, respectively [42].

In this chapter, the fabrication of graphene nano-structures and their chemical sensing properties are presented. NH_3 is highly toxic and exposure at concentrations above 50 ppm can cause serious respiratory problems [43]. Many explosives contain

ammonium nitride and its slow degradation releases small amount of NH_3; therefore, detection of ammonia could be used to determine the presence of explosives [44]. On the other hand, NH_3 in human breath can be an indicator of a kidney disorder or stomach bacterial infection [45]. In these regards, detection of NH_3 at low concentrations is essential. We have developed novel fabrication techniques to create large area graphene nano-structures and achieved an enhanced sensitivity towards NH_3 by utilizing nano-structured graphene.

1.2 Pd decorated graphene nanoribbon network for enhanced ammonia sensing

A. Experimental Methods

Single layer, CVD grown graphene on copper (Cu) foil was purchased from ACS Materials. Poly(methyl methacrylate) (PMMA) was spin coated on graphene/Cu at 4000 rpm for 45 seconds and baked at 150 ^{o}C for 5 minutes. Next, PMMA/graphene/Cu was placed on a glass slide upside down and taped from the edges. Oxygen (O_2) plasma etching was performed in a Trion Reactive Ion Etching system in order to remove the undesired graphene grown on the backside of the Cu foil. Then, PMMA/graphene/Cu was cut into pieces of 1 cm x 1 cm and left floating on the surface of 0.1 M ammonium persulfate to etch away the Cu foil. After completely etching the Cu foil, floating PMMA/graphene was picked up with a piece of silicon (Si) substrate and transferred to deionized (DI) water to clean residual chemicals. PMMA/graphene was then picked up with a Si substrate coated with 300 nm thick silicon dioxide (SiO_2) layer and allowed to dry in air overnight. Finally, PMMA layer was removed in acetone leaving only graphene on the substrate.

The fabrication process of graphene nanoribbon (GNR) network is illustrated in Figure 1.1. Silver nanowires (Ag NWs) having an average diameter of 90 nm and length of 25 µm were purchased from Blue Nano. Ag NWs in ethanol with a concentration of 10 mg/mL was coated on graphene by dip coating method. 10 nm thick Ti adhesion layer and 150 nm thick Au thin film contacts were sputtered on Ag NWs/graphene sample by employing a shadow mask. The channel length and width of the device is 3 mm and 10 mm, respectively. Subsequently, O_2 plasma etching was applied at 25 W and 15 °C with a 50 sccm O_2 flow rate for 30 seconds to form the GNR network. RF power was kept as low as possible to avoid any damage to the Ag NWs as they easily break down at higher powers. Ag NWs were removed by etching in 0.5 M ammonium persulfate for 2 hours and cleaned in DI water for an hour. Finally, the samples were annealed in flowing nitrogen (N_2) at 300 °C for 2 hours to remove any residual chemicals and reduce the contact resistance. In order to decorate GNR network with palladium (Pd) or platinum (Pt) nanoparticles, 1 nm thick Pd or Pt was evaporated on GNR network by a Temescal electron beam evaporation system. Gas sensing measurements were performed with certified, 50 ppm NH_3 gas in N_2, which was procured from Praxair. The GNR network gas sensor was mounted on a homemade chip carrier and placed inside a 50 cm^3 glass chamber with a gas inlet and outlet.

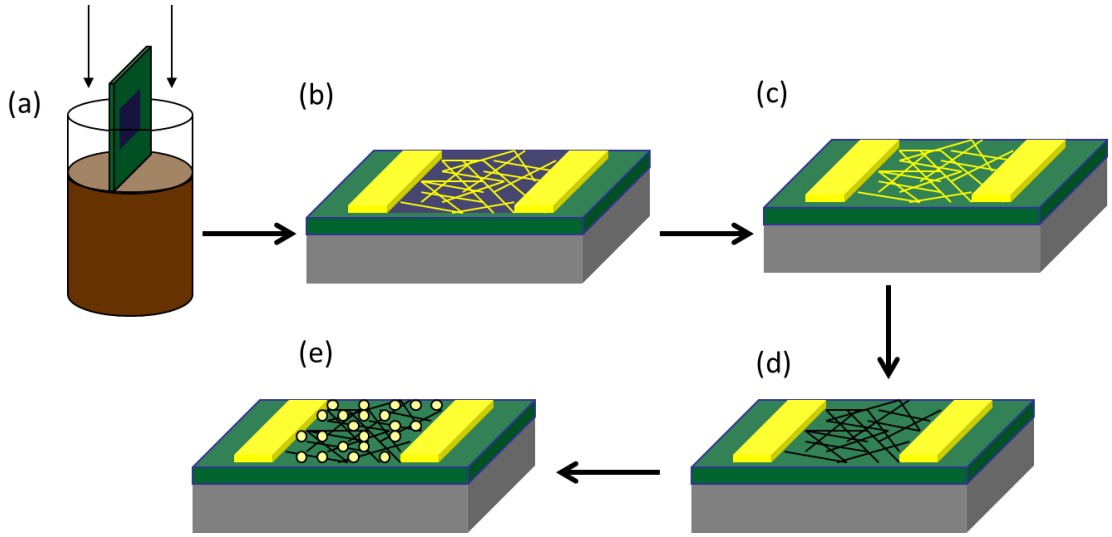

Figure 1.1: Schematic depiction of the fabrication process of metal nanoparticle decorated GNR network. (a) Dip coating of Ag NWs on graphene. (b) Sputter deposition of Ti/Au contacts. (c) O_2 plasma etching of unprotected graphene regions. (d) Removal of Ag NWs by ammonium per sulfate and subsequent cleaning in DI water and annealing at 300 ^{o}C for 2 h. (e) Evaporation of 1nm thick Pd or Pt on GNR network.

During the measurements 50 ppm NH_3 in N_2 was flowed with 200 standard cubic centimeters per minute (sccm) flow rate, which was controlled by a gas flow meter. The gas mixture was purged into the chamber with 10 minutes intervals followed by recovery in air for 10 minutes. Resistance was monitored and recorded by a digital multimeter (Keithley, 2100) in combination with software obtained from the company's website. Raman analysis was performed by Renishow RM1000 with a wavelength of 514 nm.

B. Results and Discussion

Raman spectroscopy is a powerful, noninvasive technique to characterize graphene. Raman spectra of the single layer CVD grown graphene sample utilized is shown in Figure 1.2, in which the main Raman features of pristine graphene are observed; D (1341 cm^{-1}) peak related to defects, G (1586 cm^{-1}) peak associated with bond

stretching of carbon atoms and 2D (2682 cm^{-1}) peak originated from the double resonance process [46]. As shown, the small intensity ratio of D peak to G peak (I_D/I_G, 0.28) indicates a low defect density in graphene [47]. Also, the intensity of G peak is smaller than the half intensity of 2D peak (intensity ratio of 2D peak to G peak, I_{2D}/I_G, 5.8), with the 2D peak being sharp and symmetric suggesting that graphene is predominantly single layer [48].

After dip coating, Ag NWs form a continuous network shape structure on graphene (Figure 1.3a). The coverage density of NWs can be adjusted by changing the density of NWs in ethanol or repeating the dip coating process many times. Figure 1.3b and 1.3c illustrate the final GNR network pattern with low and high magnification, respectively. After the removal of Ag NWs mask by chemical etching, a network of GNRs with an average width of 90 nm remains. Figure 1.3d shows the GNR network after 1 nm Pd deposition. At this thickness, it is seen that Pd is deposited as nanoparticles by decorating the GNR network. This approach of using straight and rigid metal nanowires placement as a reliable mask to pattern graphene into a nanoribbon network, as is demonstrated in this work, is a convenient and fast technique. We were also able to produce as small as 40 nm wide GNRs using this technique (Figure 1.4). For the gas sensors, we deliberately chose somewhat larger diameter of Ag NWs as a mask material for the GNR network because GNRs with smaller width tend to have higher electronic noise since they are more susceptible to edge defects [49].

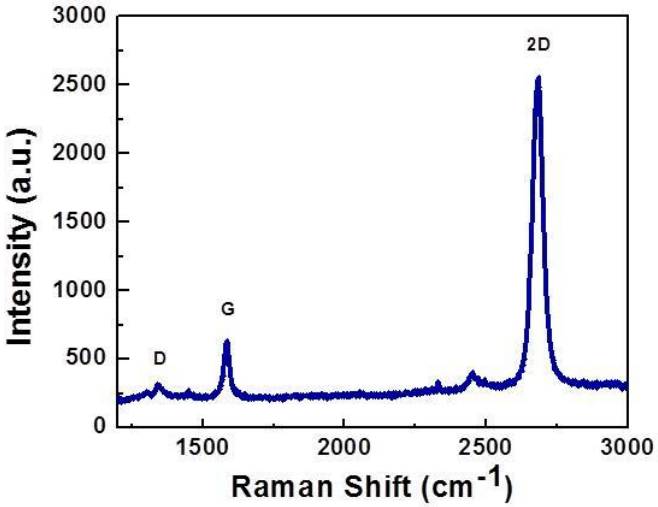

Figure 1.2: Raman spectra of single layer CVD grown graphene.

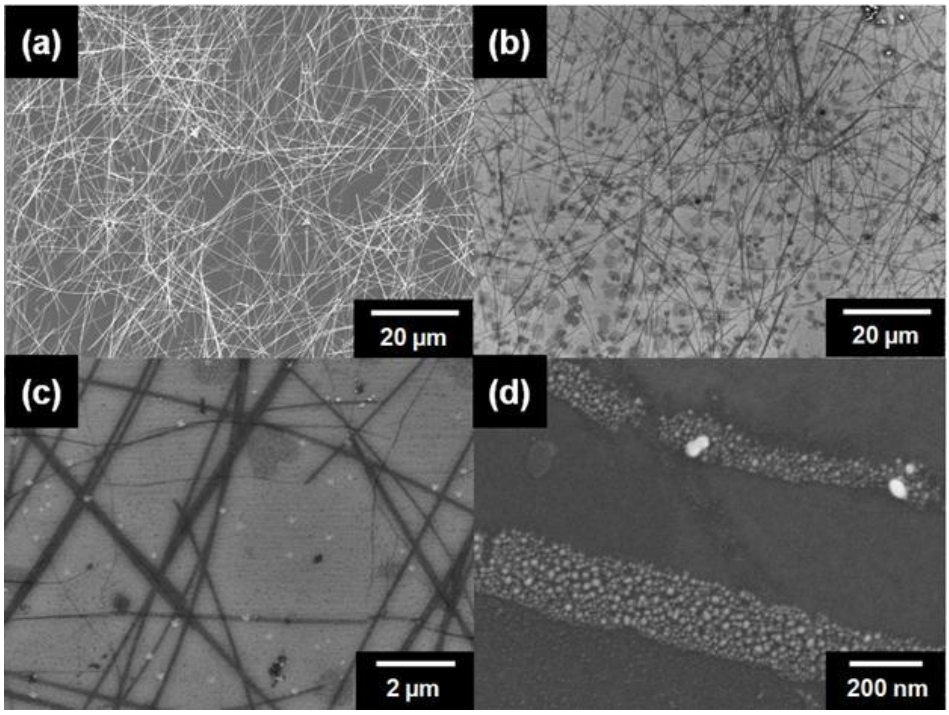

Figure 1.3: Scanning electron microscope (SEM) images of (a) coated 90 nm Ag NWs (b) the GNR network with low magnification (c) the GNR network with high magnification (d) Pd nanoparticle decorated the GNR network.

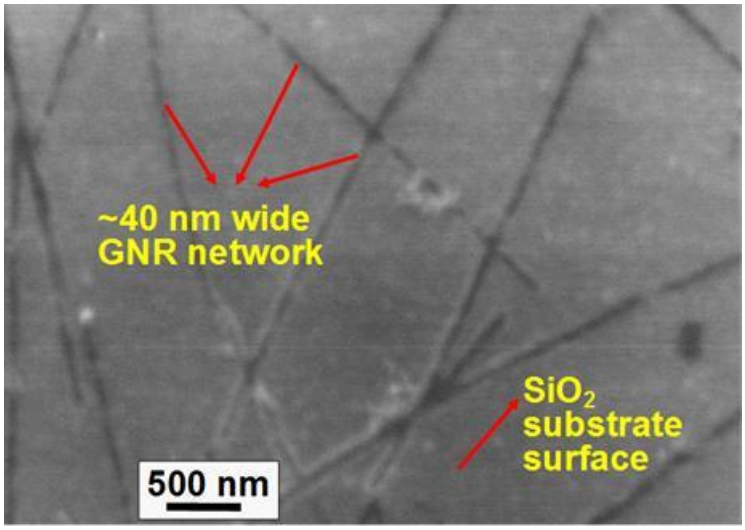

Figure 1.4: SEM image of around 40 nm wide GNR network.

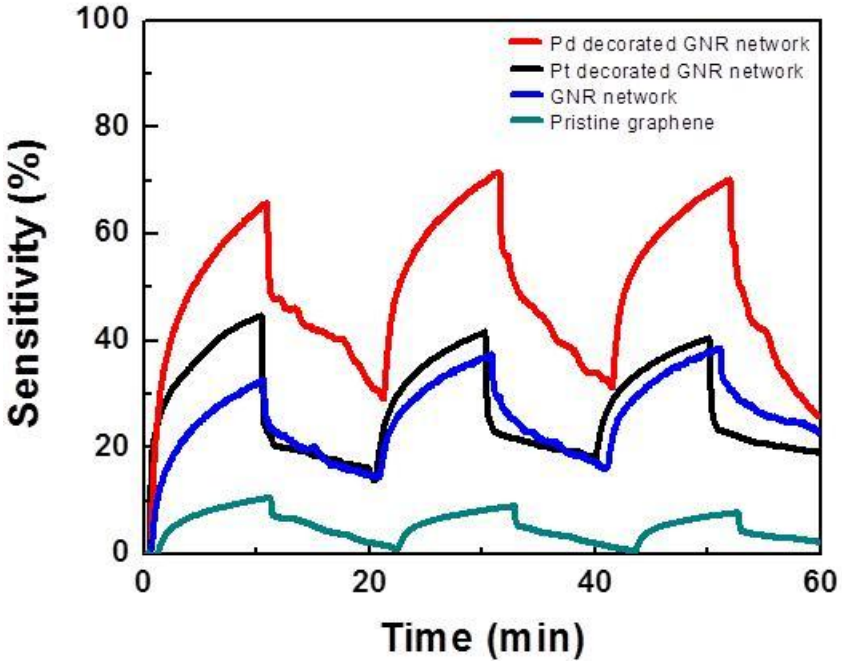

Figure 1.5: Comparative gas sensing performance of the graphene sensors with 50 ppm NH_3.

Figure 1.5 illustrates the comparative gas sensing behavior of pristine (non-patterned) graphene layer, the GNR network, Pt and Pd nanoparticle decorated GNR networks. The sensitivity of a gas sensor is defined as $S = (R_2 - R_1)/R_1 X100$, where R_1 and R_2 is the initial and final resistance of the sensor, respectively. Pd nanoparticle decorated GNR network exhibits the highest sensitivity followed by Pt decorated GNR network, the GNR network and pristine graphene with sensitivities of 65%, 45%, 33% and 10%, respectively. The increase of resistance is attributed to the decrease in the number of charge carriers in graphene. The pristine graphene, GNR network and metal decorated GNR network samples are initially p-doped due to the adsorbed O_2 molecules in air. As the NH_3 molecules adsorb on graphene, they transfer electrons to the graphene decreasing the total amount of doping. The GNR network sample exhibits three fold improved sensitivity as compared to the pristine graphene due to the excess amount of oxidized edge defects introduced during the O_2 plasma etching process, which are favorable adsorption sites for gas molecules. Zanolli investigated the sensing ability of oxygenated defects in carbon nanotubes towards various gases (NO_2, NH_3, CO, and CO_2) and found the presence of oxygenated defects in carbon nanotubes results in an increase in binding energies of the gases and improved charge transfer between carbon nanotubes and gas molecules leading to enhanced sensitivity [50]. The gas sensitivity is further improved upon decoration Pd or Pt nanoparticles on the GNR network. The discrepancy in sensitivities of Pd and Pt decorated GNR network sensors may be resulted from the morphology differences of 1nm thick Pd and Pt or their different degree of interaction with NH_3. Additionally, metal nanoparticle decorated GNR sensors show faster response to NH_3. The electrical resistance of Pd decorated GNR network, Pt decorated GNR

network, the GNR network and pristine graphene increased by 29 %, 26 %, 13 % and 4 % in 1 minute, respectively. The high sensitivity of the metal nanoparticle decorated GNR network could be explained by the presence of highly reactive oxidized edges of GNRs, which can adsorb NH_3 molecules more strongly as well as the change in the amount of doping from the metal nanoparticles upon NH_3 exposure. It is known that NH_3 is a reducing gas [51]; therefore, when adsorbed on the surface of the Pd nanoparticles, electrons will flow into Pd decreasing its work function. The energy band diagram of Pd/graphene is shown in Figure 1.6 before and after NH_3 exposure. Before the exposure, Pd has a higher work function ($W_{Pd}\approx5.1$ eV) [52] than GNRs ($W_{GNR}\approx4.58$ eV) [53], which leads to electron transfer from the GNR network into Pd nanoparticles creating more holes in the GNR network. This is consistent with the resistance measurements of Pd decorated GNR network sample, in which the resistance of the GNR network decreased from 269 KΩ to 162 KΩ after Pd nanoparticle decoration. During the exposure of NH_3, the work function of Pd is lowered below that of the GNR network and in this case, electrons flow into the GNR network channel, thus decreasing the net amount of charge carriers in GNR network and increasing its resistance.

All sensor devices tested show good repeatability and reversibility in air. After flowing NH_3/N_2 gas mixture for 10 minutes, gas flow was stopped and air was allowed to get into the chamber. The sensors exhibited around 50% recovery after 10 minutes and returned to 90% of their initial resistance after an hour. When air is introduced into the test chamber, we observe a sharp decrease of resistance followed up by a slower recovery.

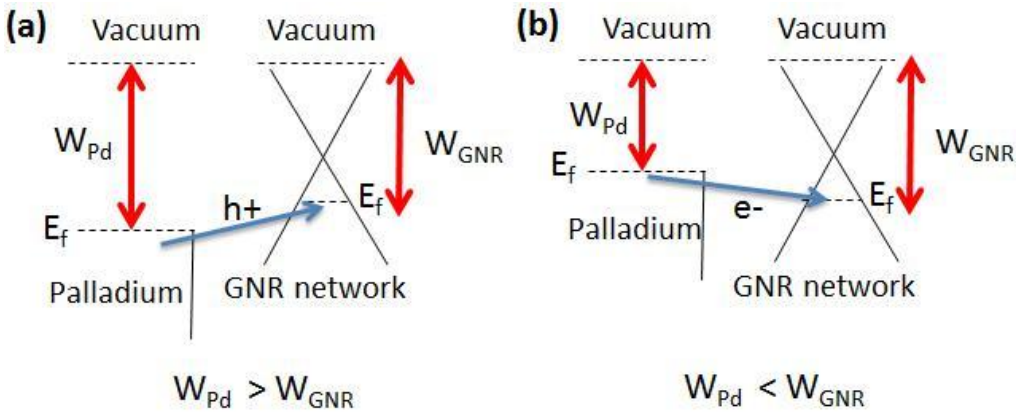

Figure 1.6: Energy band diagram of Pd nanoparticle decorated GNR network (a) before NH_3 exposure (b) during NH_3 exposure.

The sharp decrease is because of the O_2 molecules in air sticking on the unoccupied sites of graphene compensating some of the depleted holes. The following slower recovery is caused by O_2 molecules in air interacting with NH_3 molecules and causing them to be released from the graphene surface. We also tried to recover the sensors in pure N_2 environment; however, the sensors exhibit very little recovery signifying that O_2 is necessary for the recovery of the sensors.

1.3 Nano-structured graphene by emloying dewetted Ni thin films as an etch mask

A. Experimental Methods

Graphene was transferred on SiO_2 coated Si substrates by previously described PMMA transfer method. Figure 1.7 illustrates the flow of the fabrication process. First, nickel (Ni) films were evaporated on graphene by Temescal Electron Beam Evaporator, in which the thickness was monitored by a thickness sensor. Ni/graphene films were then annealed in 5% flowing H_2/N_2 gas in a Lindberg Mini Tube Furnace. After the dewetting

of the Ni films, uncovered regions of graphene were removed by O_2 plasma etching at 30 W RF power for 40 seconds in a Trion Reactive Ion Etching system. Subsequently, Ni was removed by concentrated nitric acid leaving a continuous network of graphene nano-structures. The samples were then cleaned in DI water and annealed at 400 ^oC in N_2 atmosphere for 2 hours to clean the residual nitric acid molecules. Raman measurements were conducted by a Renishow RM1000 with a wavelength of 514 nm. For gas sensing measurements, Ti/Au electrodes (10/150 nm) were deposited on the nano-structured graphene by masking the channel region (2 mm length and 10 mm width) with a piece of Teflon tape. Gas sensing measurements were carried out with certified, 50 ppm NH_3 gas in N_2, which was obtained from Praxair. The sensor devices were mounted on a homemade chip carrier and placed inside a 50 cm^3 glass chamber with a gas inlet and outlet. During the measurements 50 ppm NH_3 in N_2 was flowed with 200 sccm flow rate, which was controlled by a gas flow meter. For transport measurements, FET devices with a channel length and width of 5 μm and 10 μm, respectively, was fabricated by UV lithography, subsequent evaporation of 10/100 nm Ti/Au and lift off process. A second UV lithography process and O_2 plasma etching were performed to define the 10 um wide graphene channel. Transport measurements were carried out by Agilent B1500 Semiconductor Device Analyzer in ambient conditions.

B. Results and Discussion

Two dimensional metal thin films are metastable, when heated; they undergo structural changes in order to minimize the free energy of film/substrate system, a process called dewetting [54].

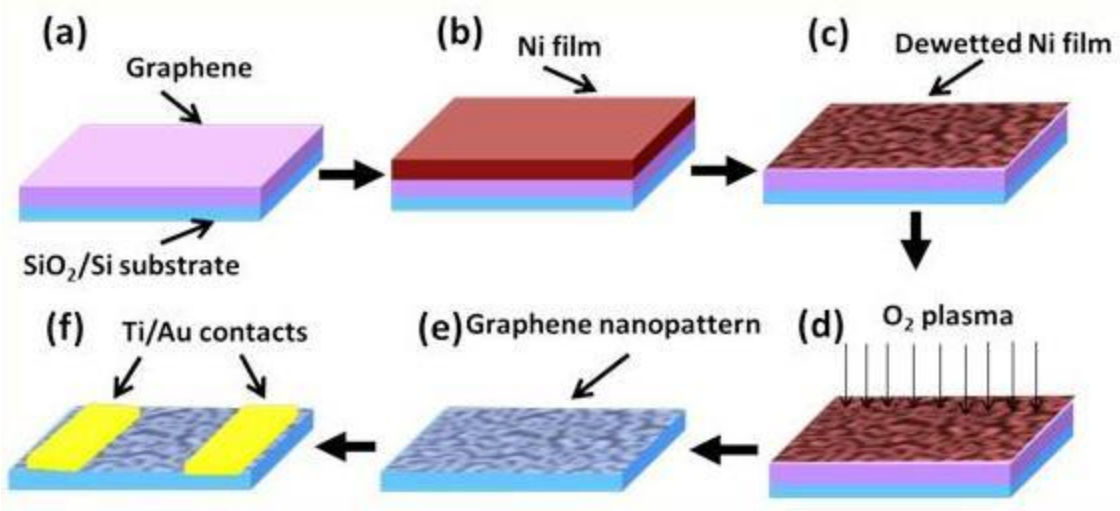

Figure 1.7: Schematic depiction of the fabrication process of nano-structured graphene by employing dewetted Ni thin films as an etch mask.

Many studies have been done in order to elucidate the dewetting mechanism of thin films [55-57]. Dewetting can be considered as a two-step process of void nucleation and following void growth [58]. Void nucleation is believed to be induced by defects, grain boundary triple points, pinholes and gas bubbles [59]. In this study, we use the dewetting of Ni thin films as a self-assembly process to create Ni nano-structures, which is then employed as an etch mask to obtain graphene nano-structures. We chose Ni as the metal film for dewetting since we could deposit well controlled ultra-thin continuous Ni films, and also it doesn't require a high temperature to dewet. Figure 1.8 shows the structure evolution of 5 nm thick Ni film deposited on graphene, which was annealed at 300 ^{o}C under 5% H_2/N_2 gas flow. As-deposited Ni film is continuous as seen in Figure 1.8a. When the Ni film is annealed, voids are formed in the film (Figure 1.8b). With further annealing, voids begin to grow resulting in a porous yet a continuous film. Such a

continuous nano-structured network of Ni mask is essential as the underlying graphene network also needs to be continuous for any charge transport device (Figure 1.8c). Further annealing causes a formation of discrete Ni nano-islands (Figure 1.8d). H_2 gas was found to be crucial for the formation of such nano-structures on graphene as we were unsuccessful to dewed Ni films on graphene in pure N_2 environment. This can be explained by the formation of nickel hydride in H_2 environment, which results in an increase in the free energy of Ni/graphene system favoring the dewetting of Ni film [60]. Table 1.1 shows the optimum annealing temperature and time for the dewetting of Ni films at various thicknesses, which was obtained experimentally. It appears that a thinner Ni film takes a shorter time and lower temperature for dewetting while a thicker film requires a longer time and higher temperature for the desired degree of dewetting to form continuous Ni nano-structures. In order to obtain a continuous network of Ni nano-structures, we carefully optimized the temperature and time. Figure 1.9 shows the SEM images of the dewetted Ni films as well as the final graphene nano-structures obtained by employing the dewetted Ni films as an etch mask. As shown in the micrographs, the dewetted Ni films form irregular, interconnected nano-structures, whose widths have a distribution in size. As we reduce the thickness of Ni film, the width dimension of Ni nano-structures also decreases and the density of the nickel nano-structures increases. We have performed Raman spectroscopy measurements in order to evaluate the structural properties of nano-structured graphene.

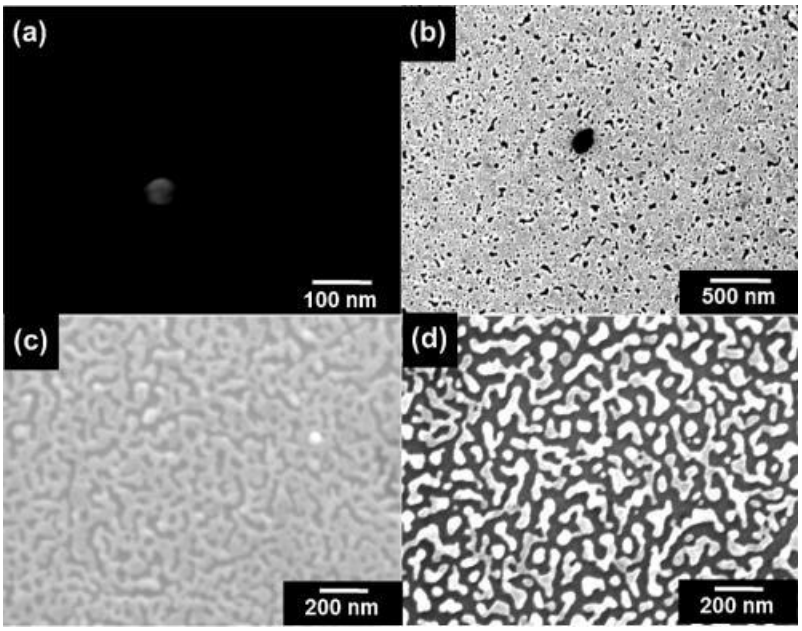

Figure 1.8: Structure evolution of dewetted 5nm thick Ni film. (a) As-deposited. (b) Annealed at 300 ^{o}C for 5 minutes. (c) Annealed at 300 ^{o}C for 10 minutes. (c) Annealed at 300 ^{o}C for 20 minutes.

Table 1.1: Optimum temperature and time values for the dewetting of Ni thin films.

Thickness of Ni film (nm)	Optimum annealing temperature (^{o}C)	Optimum annealing time (minutes)
10	400	15
5	300	10
3	250	8

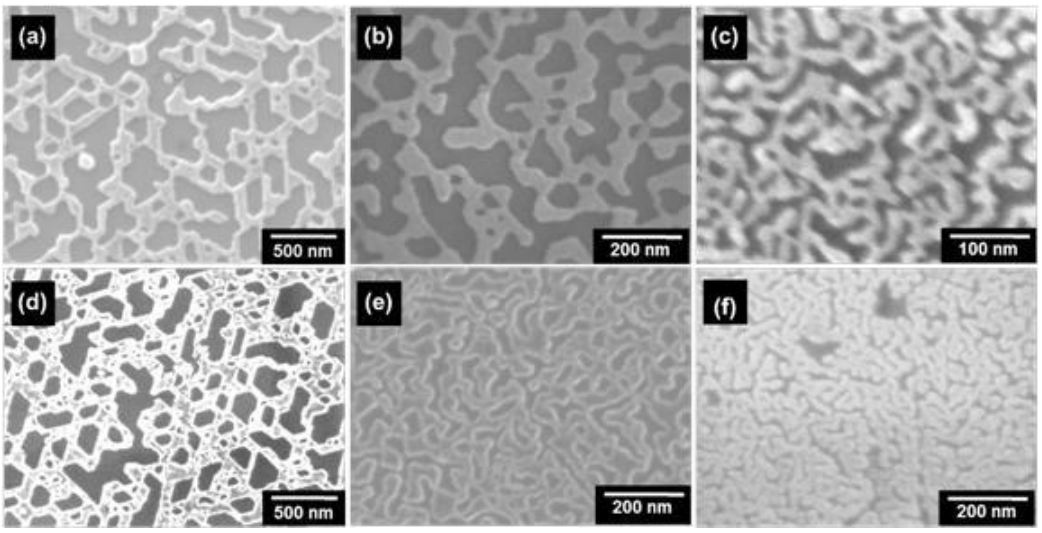

Figure 1.9: SEM images of (a) 10 nm thick, (b) 5 nm thick, (c) 3 nm thick dewetted Ni films and the corresponding final nano-structures of graphene obtained by employing (d) 10 nm Ni, (e) 5 nm Ni, (f) 3nm Ni films.

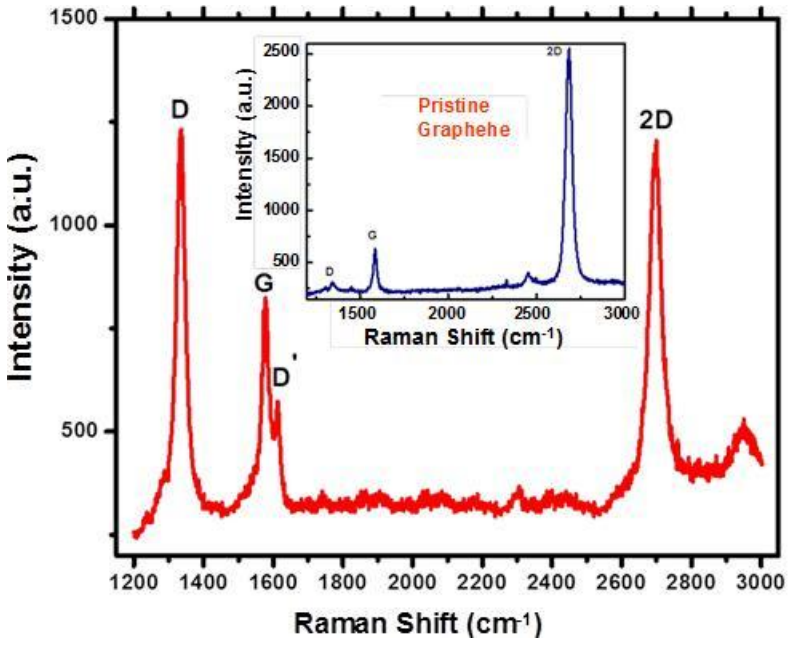

Figure 1.10: Raman spectra of pristine (Inset) and nano-structured graphene.

Figure 1.10 shows the Raman spectra of pristine and nano-structured graphene, in which the main Raman features of graphene is observed for both samples. The intensity of D peak dramatically increases for the nano-stuructured graphene signifying the formation of excess number of edge defects [47]. Furthermore, we confirmed an additional defect related peak denoted as $D^{'}$ at a frequency of around 1627 cm^{-1} for the nano-structured graphene, which is originated from increased amount of disorder [61]. Moreover, the positions of G and 2D peaks shifted from 1586 cm^{-1} to 1593 cm^{-1} and from 2682 cm^{-1} to 2700 cm^{-1}, respectively. The upshift in the positions of G and 2D peaks is attributed to strong hole doping by oxidation of graphene edges due to the O_2 plasma and nitric acid exposure [62, 63].

We have also conducted electrical transport measurements of pristine and nano-structured graphene in a FET device geometry. Figure 1.11 shows drain current-drain voltage and drain current-gate voltage characteristics of pristine and nano-structured graphene obtained by employing 5 nm thick Ni film. While the pristine graphene shows linear I-V behavior (Inset Figure 1.11a), the nano-structured graphene shows significantly nonlinear characteristics (Figure 1.11b) indicating the formation of a Schottky barrier due to the semiconducting nature of the nano-structured graphene [64]. An electronic band gap is opened when graphene is patterned into narrow graphene nanoribbons due to the quantum confinement of charge carriers [65]. The magnitude of the band gap inversely scales with the size of the nanoribbon width [31].

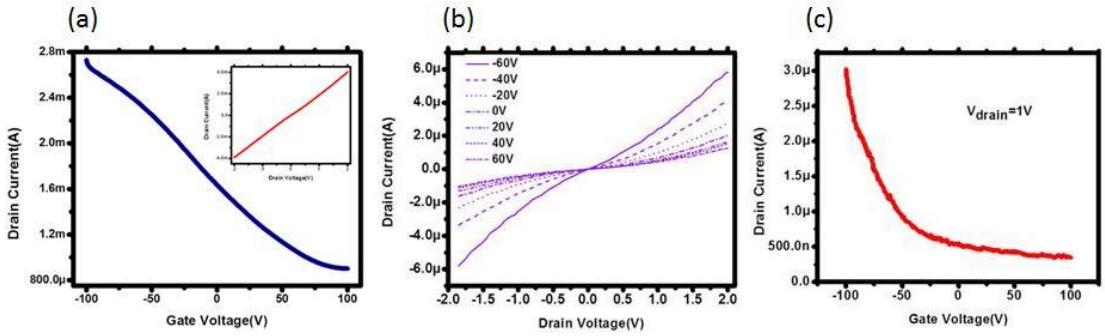

Figure 1.11: (a) Drain Current-Gate Voltage curve of pristine graphene (Inset shows the Drain Current-Drain Voltage curve). (b) Drain Current-Drain Voltage characteristics of nano-structured graphene at different gate voltages. (b) Drain Current-Gate Voltage behavior of nano-structured graphene.

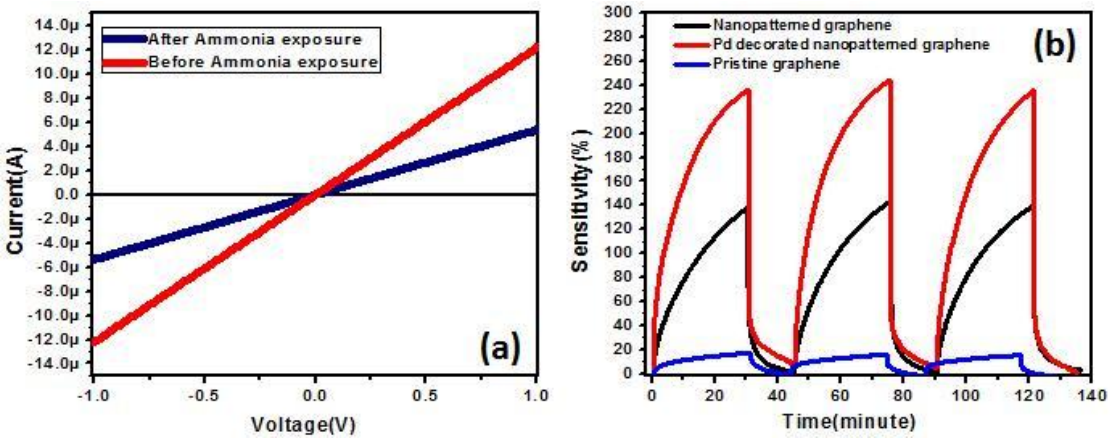

Figure 1.12: (a) Current-Voltage characteristic of nano-structured graphene before and after ammonia exposure. (b) NH_3 sensing performance of pristine, nano-structured and Pd decorated nano-structured graphene sensors.

The drain currrent-gate voltage curves of the FET devices fabricated from pristine and the nano-structured graphene show on/off current ratios of 3 and 10, respectively, signifying that a slight band gap is opened upon nano-structuring of graphene (Figure 1.11c).

For the sensing experiments, we used the nano-structured graphene obtained by employing 10 nm thick Ni thin films as it leads to uniform graphene nano-structures in large area. Figure 1.12a exhibits the current-voltage characteristics of nano-structured graphene before and after ammonia exposure, in which a linear I-V response is obtained suggesting the contacts are ohmic and the sensor response is governed by the graphene channel itself. Figure 1.12b compares the NH_3 sensing behavior of pristine, the nano-structured and the Pd decorated nano-structured graphene, in which the sensor devices were exposed to 50 ppm NH_3 gas for 30 minutes, followed by air for the recovery. When exposed to NH_3, all sensor devices exhibited an increase of resistance due to the electron donating nature of NH_3, which causes depletion of holes in initially p-doped graphene. The pristine graphene sensor shows only 15% change of resistance in 30 minutes whereas the resistance of the nano-structured graphene increases by about 140%. The significant increase in sensitivity is attributed to the chemically active edges of graphene nano-structures, where NH_3 molecules can adsorb more strongly and as a result donate electrons more efficiently. Decoration of the nano-structured graphene with Pd nanoparticles further increased the sensitivity up to 240%. These results are consistent with Pd decorated graphene nanoribbon network sensors. However, nano-structured graphene sensors fabricated by employing the dewetted Ni thin films show higher sensitivity to NH_3, which could be resulted from the fact that this method can produce

higher density of graphene nano-structures. The sensors shows complete recovery in 15 minutes after air is introduced into the chamber. O_2 molecules in air help the desorption of NH_3 recovering the depleted holes, in turn decreasing the resistance to its original state.

1.4 Summary

In summary, we have developed scalable and facile nano-structuring techniques for graphene, which could be useful for electronic and sensing applications. Patterning graphene into narrow nano-structures results in opening of a slight electronic band-gap, which is verified by electronic transport measurements, in which on/off current ratio increases from 3 to 10 after nano-patterning. Furthermore, the nano-structuring of graphene seems to be a promising method for the detection of trace amount of ammonia gas at ppm level as it provides dramatically enhanced sensing performance. Decorating the nano-patterned graphene with metal nanoparticles further increases the sensitivity providing superior sensitivity.

Chapter 1, in part, has been published in Journal of Nanoscience and Nanotechnology in 2015 by Cihan Kuru, Duyoung Choi, Chulmin Choi, Young Jin Kim and Sungho Jin. The dissertation/thesis author was the primary investigator and author of this paper.

CHAPTER 2: HYDROGEN SENSORS BASED ON TRANSITION METAL DICHALCOGENIDES

2.1 Introduction

Hydrogen, a clean and abundant energy source, has been utilized in fuel cells to generate electricity with the aim of reducing the dependence on fossil fuels. However, hydrogen is a colorless, odorless, tasteless, flammable and explosive gas, which arises some safety concerns. For the safe implementation of fuel cells, hydrogen leaks have to be detected before hydrogen concentration reaches a hazardous level [66, 67]. Metal oxide sensors [68-70] can detect hydrogen with high sensitivity; however, they suffer from high power consumption due to their high operation temperature (typically above 300 ^{o}C) and they have poor hydrogen selectivity. Pd-based sensors, where Pd thin films [71] or nanostructures [72] such as Pd nanowires (NWs) are used as the sensing material are capable of room temperature operation with good selectivity; yet their sensitivity is somewhat low and they undergo mechanical degradations during hydrogen adsorption/desorption [73]. Decoration of Pd nanoparticles on graphene [74, 75], Si NWs [76] or carbon nanotubes (CNTs) [77, 78] circumvents the problem of mechanical degradation and has the benefit of increasing the sensitivity. However, the growth of these materials requires high temperature processing, complicating the sensor fabrication and increasing the cost. Hence, developing reliable, low-cost hydrogen detection technologies which can operate at room temperature is highly desirable.

Two dimensional (2D) materials have drawn tremendous attention in recent years due to their novel and unique electronic, optical and mechanical properties [79-81].

Moreover, their high surface-to-volume ratio makes them attractive for sensing applications. Graphene, a 2D material made of carbon, has been shown to be an effective sensing platform for toxic gases such as NO_2 and NH_3 [82-85]. Decorating graphene with metal nanoparticles (NPs) such as Pt, Pd, Au or Ag increases the sensor response due to their catalytic effect [86, 87]. Moreover, Pd-decorated graphene has been demonstrated as a hydrogen sensor [88, 89], in which the modulation of Pd work function causes a change in the amount of net doping in graphene leading to a resistance change showing a response to hydrogen.

2.2 MoS_2 nanosheet-Pd nanoparticle composite for highly sensitive room temperature detection of hydrogen

Recently, molybdenum disulfide (MoS_2) has been explored for electronic applications due to its sizable band gap (1.2 eV and 1.8 eV for bulk and single layer, respectively), which enables its conductivity to be modulated by a gate voltage [90, 91]. Similar to graphene, MoS_2 has a layered structure, where each layer consists of covalently bonded Mo-S atoms and the neighboring layers attach each other by van der Waals forces [92]. MoS_2 can be obtained by mechanical or chemical exfoliation of bulk MoS_2 or can be grown by Chemical Vapor Deposition (CVD) [93-95]. Perkins *et al.* have demonstrated mechanically exfoliated single layer MoS_2 flake as a chemical sensor, in which monolayer MoS_2 shows a strong response to electron donors (triethylamine) and a lower response to electron acceptors (acetone) with detection limits of 10 ppb (parts per billion) and 500 ppm (parts per million), respectively, attributed to the n-type nature of MoS_2 [96]. However, mechanical exfoliation is a low yield method and is not suitable for

practical applications. On the other hand, CVD grown MoS_2 films have also been investigated for the gas sensing and a strong response was found towards NH_3 with a detection limit of 300 ppb [97]. Although CVD method seems to provide a solution for the scalable growth of MoS_2, high temperature growth conditions (750 °C-1000 °C) [94, 97] pose a barrier for the inexpensive fabrication of chemical sensors.

Chemical exfoliation of MoS_2 is favorable for the large scale and low-cost production of MoS_2 chemical sensors. A lithium intercalation method [98] can be used to exfoliate bulk MoS_2 crystals to produce single layer MoS_2 nanosheets. However, this method requires a long lithiation process (3 days) and results in MoS_2 nanosheets with traces of lithium particles, which degrades the MoS_2 semiconducting properties [99]. On the other hand, solvent exfoliation method [100] can provide high yield and fast production of a few layer MoS_2 nanosheets, in which the exfoliation takes place by ultrasonication of bulk MoS_2 in suitable solvents such as N-methyl-pyrorolidone (NMP) or isopropanol whose surface tension is in the range of 30-40 mJ/m^2, which facilitates the exfoliation process [101, 102].

In this work, we present solution-processed MoS_2 nanosheet–Pd nanoparticle composite for hydrogen sensing at room temperature, in which the MoS_2-Pd composite shows remarkable electrical response towards hydrogen with excellent response and recovery times. A few-layers MoS_2 nanosheets can be produced by a facile solvent exfoliation method and the MoS_2-Pd composite can be fabricated by simply drop casting of MoS_2-$PdCl_2$ solution and subsequent annealing process. The effect of annealing time on the hydrogen sensing performance of MoS_2-Pd composite is investigated. The sensing mechanism is studied by transport measurements of the MoS_2 nanosheets and MoS_2-Pd

composite by fabricating field effect transistor (FET) devices. We also compare the hydrogen sensing performance of MoS_2-Pd composite with graphene-Pd composite, fabricated in a similar fashion, revealing that the MoS_2-Pd exhibits much higher sensor response with shorter response and recovery times and indicating that 2D MoS_2 is a promising candidate for highly sensitive room temperature gas detection.

A. Experimental Methods

Materials: Bulk MoS_2 powder (5 μm powder size), N-methyl-pyrorolidone (NMP) and palladium chloride ($PdCl_2$) were purchased from Sigma Aldrich. Bulk graphite flakes were purchased from Graphene Supermarket.

Preparation of MoS_2-$PdCl_2$ and Graphene-$PdCl_2$ Solutions: 400 mg bulk MoS_2 powder was mixed with 80 mL NMP and then the mixture was probe sonicated (750W and 80% amplitude) in an ice bath for 2h to exfoliate the bulk MoS_2. The resultant solution was then centrifuged at 1500 rpm for 45 min to remove any remaining bulk particles. After that, NMP was evaporated in a vacuum oven followed by redispersion of MoS_2 nanosheets in deionized water with a concentration of 1.5 mg/mL. MoS_2-$PdCl_2$ solution was prepared by adding 30 mg $PdCl_2$ into 20 mL of MoS_2-water solution and a subsequent sonication for 30 min. Graphene-$PdCl_2$ solution was prepared by following the same procedure.

Fabrication of Hydrogen Sensors: 0.5 mL of prepared MoS_2-$PdCl_2$ and graphene-$PdCl_2$ solution was dropped on SiO_2-coated Si substrates, followed by baking on a hot plate at 100 ^oC until the solution is dried. The resultant film was then annealed in forming gas atmosphere at 400 ^oC to reduce $PdCl_2$ and remove any remaining NMP. In order to

fabricate the contacts for sensing measurements a piece of Teflon tape was used as a mask to define the channel (2 mm channel length and 1 cm width) and subsequent sputter deposition of Ti/Au (10 nm/ 150 nm) was performed. For the fabrication of MoS_2 nanosheet sensors, MoS_2 nanosheets which were dispersed in ethanol was spin coated on a SiO_2-coated Si substrate and then photolithography and following deposition of Ti/Au (10 nm/150 nm) were performed to fabricate finger electrodes.

Characterization: XRD (X-ray diffraction) measurements were conducted by a Bruker D2 Phaser X-ray diffractometer with Cu K_α (λ=0.154 nm) as the radiation source. Raman spectroscopy measurements were carried out by a Renishaw raman spectrometer at 514 nm. AFM (Atomic force microscopy) measurements were performed with a Digital Instruments 3100 microscope under tapping mode.

Sensing Measurements: 50,000 ppm of H_2 in N_2 was used as a starting gas and it was diluted with N_2 to the desired concentrations by using mass flow controllers. For the measurements, target gas was flowed with 200 sccm flow rate through a small glass chamber (10 cm^3 volume), where the sensor device is mounted, and the resistance was recorded by 2100 Keithley multimeter (Figure 2.1). For ammonia sensing measurements, 50 ppm ammonia gas in N_2 was used. For ethanol and acetone sensing measurements, the desired amount of liquid acetone and ethanol (calculated by using ideal gas law) were evaporated in a closed chamber, in which the concentrations of the solvents correspond to 50,000 ppm. For the recovery of the sensors, air was introduced into the chamber.

Fabrication of FET Devices and Transport Measurements: MoS_2 nanosheets and MoS_2 nanosheet-$PdCl_2$ dispersed in ethanol were spin coated on a SiO_2 (300 nm thick) coated Si (high doped) substrate. A subsequent annealing process at 400 ^oC in forming gas

environment was performed in order to reduce $PdCl_2$. Source and drain electrodes were fabricated by photolithography and subsequent evaporation of Ti/Au (10 nm/150 nm). Transport measurements were conducted by B1500 Agilent semiconductor device analyzer.

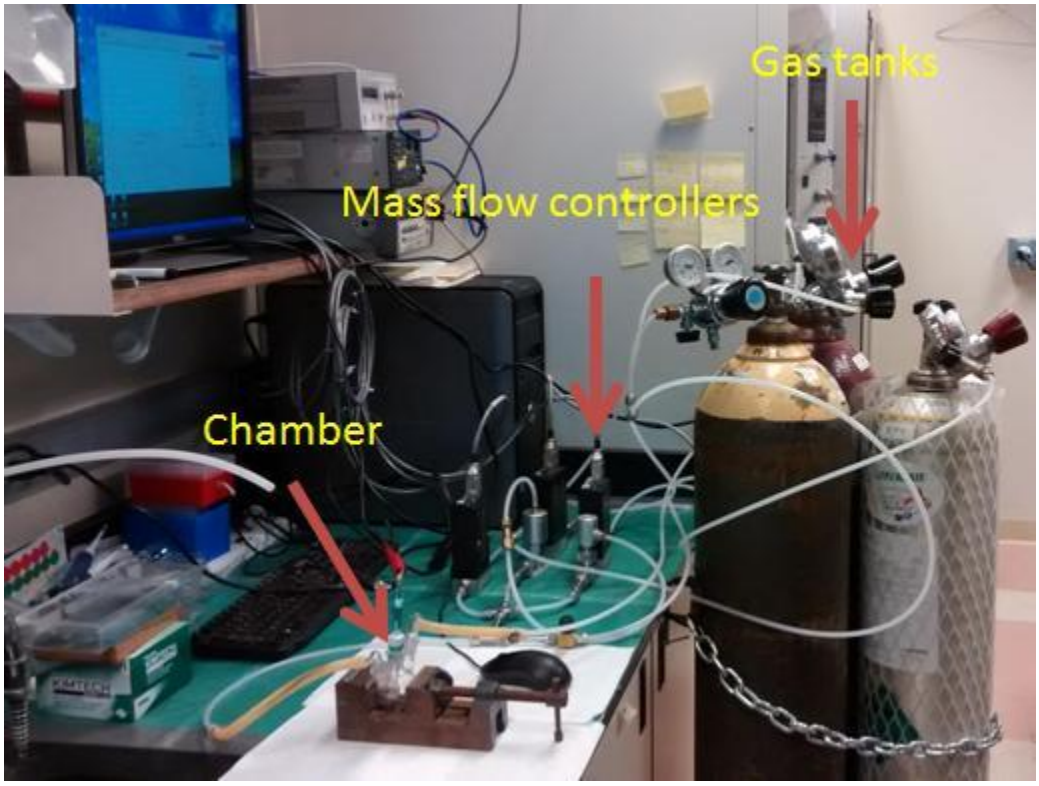

Figure 2.1: Optical image of the gas sensing set up.

B. Results and Discussion

MoS_2-Pd composite was prepared by drop casting of the MoS_2-$PdCl_2$ solution (Figure 2.2a) on SiO_2-coated Si substrates with subsequent annealing process to reduce $PdCl_2$ (see the Experimental Section for details). The optical image of sensor device is shown in Figure 2.2b. Figure 2.2c and d show tilted-view scanning electron microscopy (SEM) images of the MoS_2-Pd composite film, in which MoS_2-Pd composite forms a continous film (around 500 nm thick) in a self-assembled manner. From the top-wiev SEM image (Figure 2.2e), it is clear that MoS_2 nanosheets are highly exfoliated as they appear transparent. Figure 2.2f illustrates the schematic diagram of the MoS_2-Pd composite, in which Pd NPs (20 nm-100 nm diameter) are sandwiched by MoS_2 nanosheets.

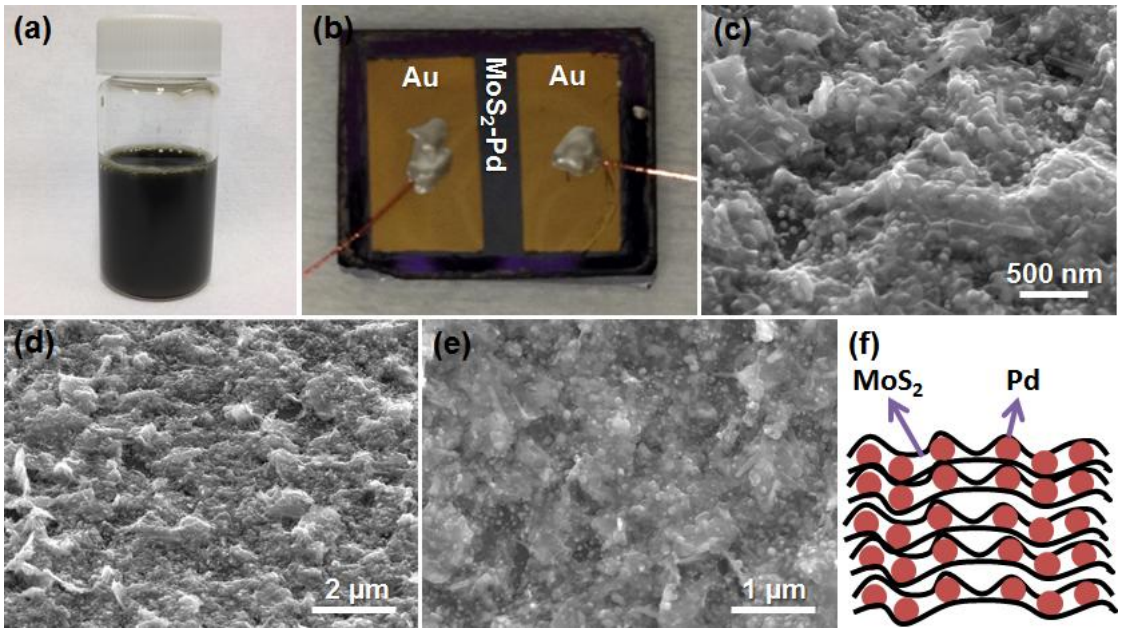

Figure 2.2: Optical image of (a) MoS_2-$PdCl_2$ solution and (b) MoS_2-Pd composite sensor device. (c) High and (d) low magnification tilted-view, and (e) top-view SEM images of MoS_2-Pd composite. (f) Schematic illustration of MoS_2-Pd composite.

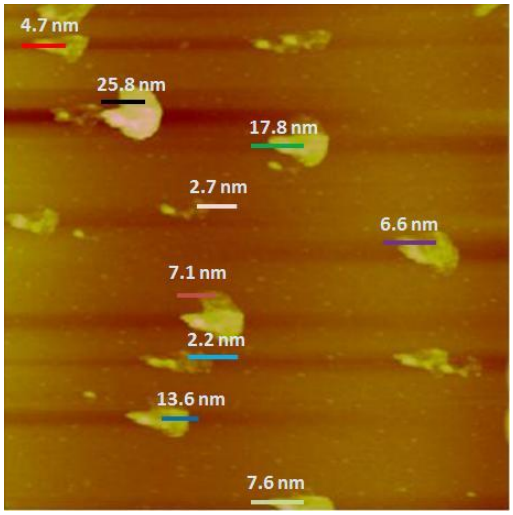

Figure 2.3: AFM image of MoS_2 flakes dispersed on a Si substrate.

In order to further understand the layered structure of MoS_2, AFM measurements and thickness analysis of the MoS_2 flakes dispersed on a Si substrate were carried out. We measured the thicknesses of 9 MoS_2 flakes, in which we found that the thicknesses of the flakes range from 2.2 nm to 25.8 nm (Figure 2.3), with the majority of the flakes having a thickness less than 10 nm. By considering the thickness of the single layer MoS_2 being 0.65 nm [103], the number of layers is estimated to range from 3 to 40.

X-ray diffraction (XRD) analyses (Figure 2.4) were carried out in order to evaluate the crystal structure of bulk MoS_2 powder and the MoS_2-Pd composite. XRD pattern of bulk MoS_2 powder shows the main peaks of molybdenite-2H, in which a strong peak is observed at $2\theta \approx 14.4^{o}$ (002), indicating that MoS_2 powder is highly crystalline [104]. On the other hand, the MoS_2-Pd composite exhibited only one pronounced peak,

(002) peak, with a much smaller intensity compared to bulk MoS_2 indicating that MoS_2 is highly exfoliated after ultrasonication [105, 106]. The small (002) peak can be attributed to the fact that MoS_2 nanosheets are precluded from restacking by Pd NPs. Furthermore, we observed an additional peak for MoS_2-Pd composite at $2\theta \approx 41^o$, which corresponds to (111) plane of fcc Pd. To further analyze the MoS_2, Raman spectroscopy measurements were performed (Figure 2.5), in which the characteristic Raman shifts of the MoS_2 (E^1_{2g} and A_{1g}) [107] were observed for the both samples.

The electrical response of the sensors to H_2 was evaluated by flowing H_2 in N_2 with 200 sccm (standard cubic centimeters per minute) flow rate at room temperature. In our measurements, the effect of N_2 on sensor response is strictly eliminated by flowing N_2 prior to H_2 until the sensor response is stabilized. The MoS_2 nanosheets and MoS_2-Pd composite show a strong response to N_2, which could be explained by the fact that O_2 molecules are pushed outside of the chamber by N_2 flow, in which p-doping effect of O_2 vanishes. O_2 adsorption is known to lead a significant hole doping in graphene [108], hence a similar effect can be expected for the MoS_2. The sensor response is defined as R_1/R_2, where R_1 and R_2 are the resistance of the sensor device in N_2 and H_2, respectively. Figure 2.6a shows the electrical response of the MoS_2 nanosheets and MoS_2-Pd composite to 50,000 ppm of H_2, in which the MoS_2 nanosheets do not show any significant response to H_2 exposure (see Figure 2.6b for the zoomed-in plot to see the details of response) while the MoS_2-Pd composite shows a strong response. Pd NPs serve as the sensing material, where the work function of Pd shifts upon H_2 exposure due to the formation of PdH_x compounds [109]. H_2 molecules can dissociate on the surface of Pd and diffuse into the Pd lattice changing its work function [110]. As a result, the doping

amount in the MoS_2 is altered by changing the overall resistance of the device. The role of the MoS_2 is crucial since it serves as a platform for the attachement of the Pd NPs and provides high surface-to-volume-ratio and low charge carrier desity in the background due to its semiconducting nature, which makes it highly sensitive to H_2 exposure.

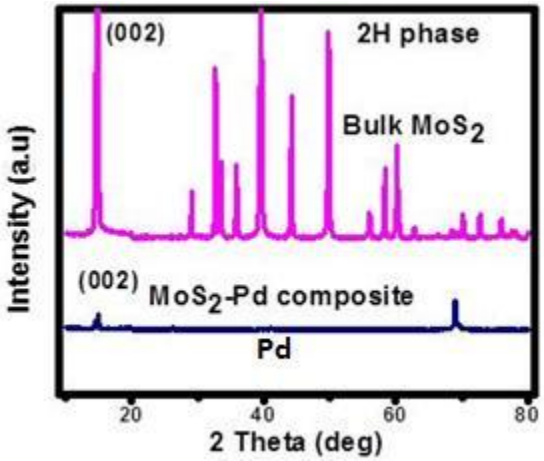

Figure 2.4: XRD patterns of bulk MoS_2 and MoS_2-Pd composite.

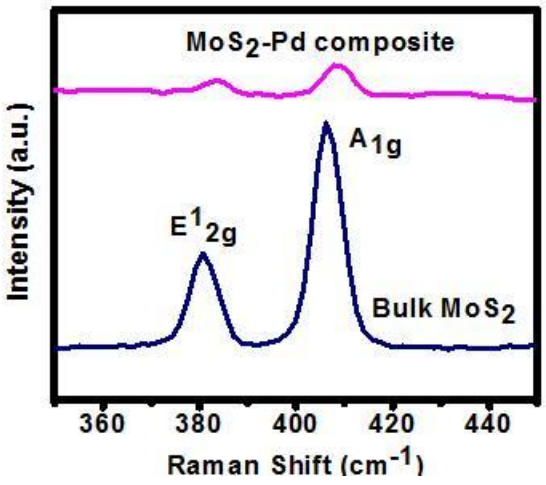

Figure 2.5: Raman spectra of bulk MoS_2 and MoS_2-Pd composite.

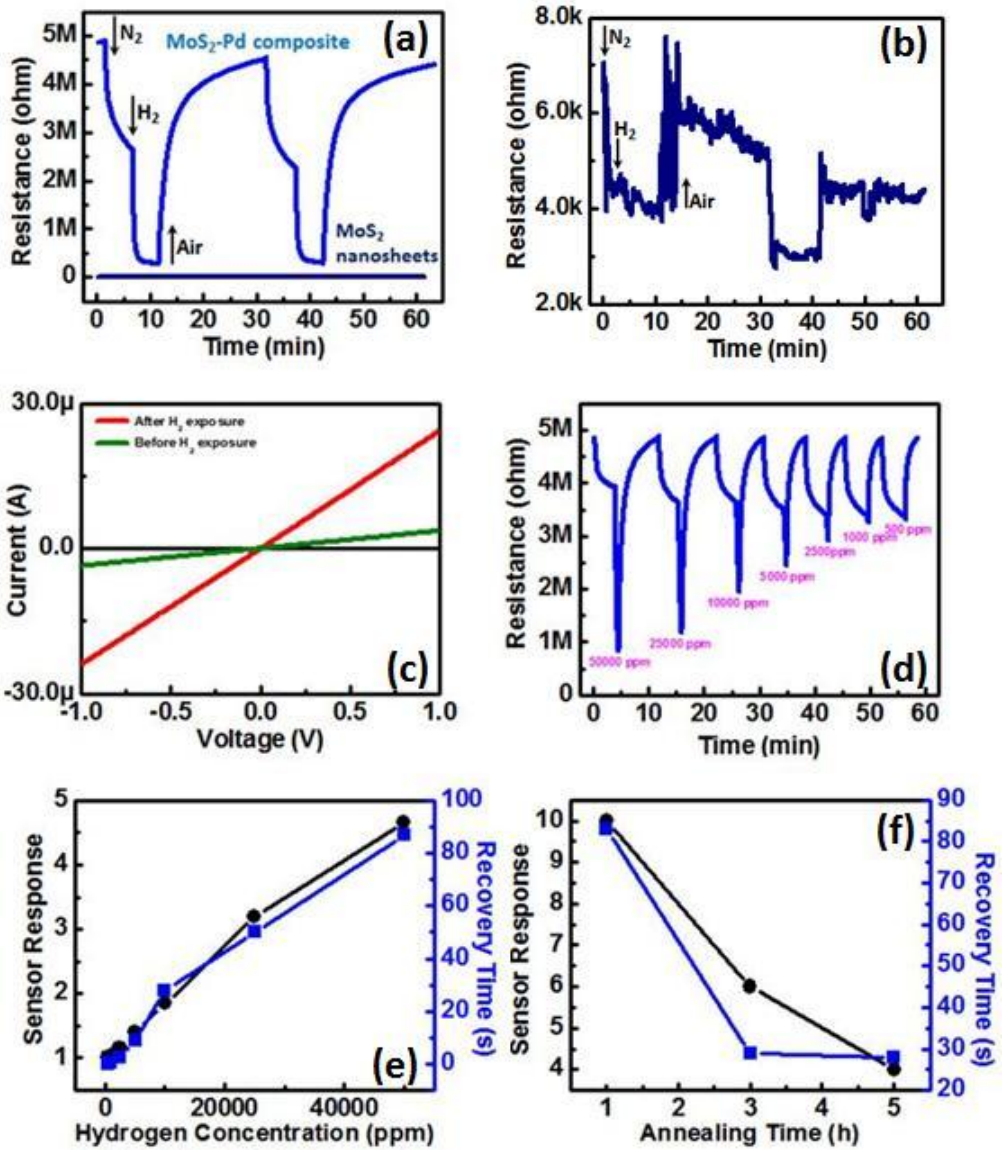

Figure 2.6: (a) Electrical responses of pristine MoS_2 nanosheets and MoS_2-Pd composite to 50,000 ppm H_2. (b) Electrical response of MoS_2 nanosheets to 50,000 ppm H_2. (c) I-V characteristics of MoS_2-Pd composite before and after H_2 exposure. (d) Electrical response of MoS_2-Pd composite exposed to different concentrations of H_2 (500 ppm-50,000 ppm) by 40s pulses. (e) Recovery time and sensor response of MoS_2-Pd composite as a function of H_2 concentration. (f) Recovery time and sensor response of MoS_2-Pd composite as a function of annealing time.

The resistance of the MoS_2-Pd composite device exhibits a sharp decrease with H_2 exposure followed by saturation, with the sensor response being about 10, and the sensor shows complete recovery in air without any heating or UV irradiation. The desorption of hydrogen atoms from Pd takes place in the presence of O_2 by forming H_2O [111], which in turn recovers the sensor. The sensor response and recovery times are defined as the amount of the time required for the sensor resistance to reach 90% of its saturation and to recover to 90% of its ground state, respectively [112]. The MoS_2-Pd composite sensor device has response and recovery times of 40 s and 83 s, respectively. I-V measurements were performed before and after H_2 exposure (Figure 2.6c), in which linear I-V responses are obtained. This ensures that no Schottky barrier forms between Ti/Au contacts and MoS_2-Pd composite and the channel itself is responsible for the resistance change upon H_2 exposure rather than the modulation of Schottky barrier height. We also performed sensing measurements at different concentrations of H_2, ranging from 50,000 ppm to 500 ppm by 40 s pulses (Figure 2.6d). Figure 2.6e shows the recovery time and sensor response as a function of H_2 concentration, in which both the recovery time and sensor response decrease with the decreasing H_2 concentration. As the partial pressure of H_2 is decreased, the amount of hydrogen uptake into the Pd NPs is reduced resulting in a lower sensor response. The sensor response exhibits almost a linear trend for concentrations of 500 ppm-25,000 ppm and tends to deviate to a saturation trend at higher concentrations.

The effect of annealing time on the sensor characteristics of the MoS_2-Pd composite was investigated. Figure 2.6f shows the recovery time and sensor response of the MoS_2-Pd composite sensors annealed for various time durations.

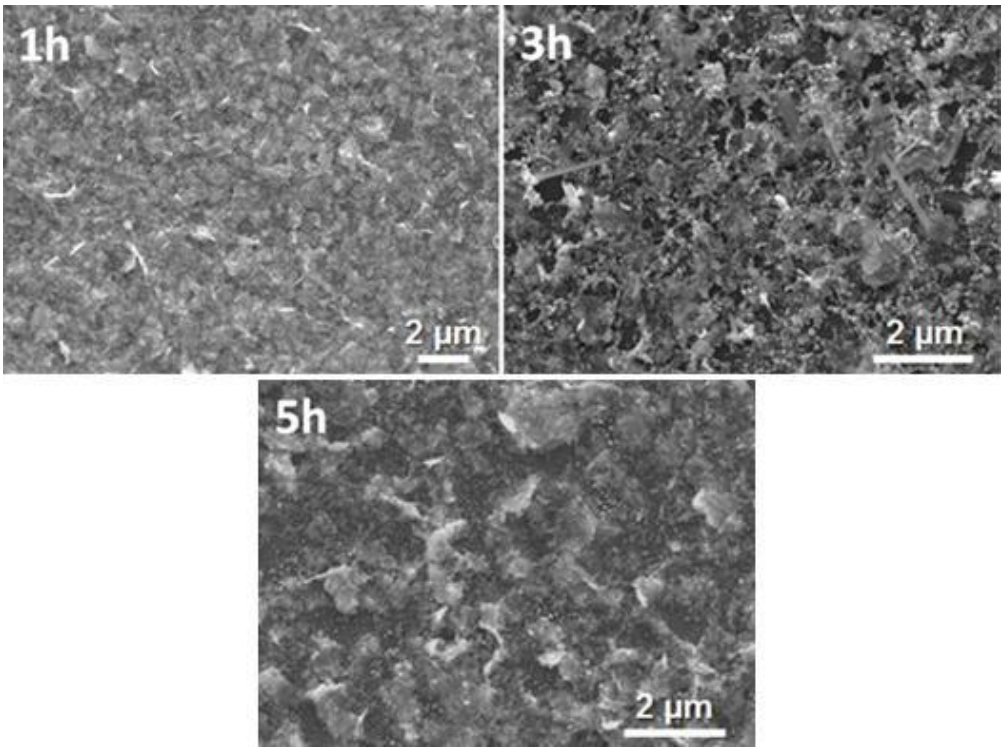

Figure 2.7: SEM images of MoS_2-Pd composites annealed at 500^o C for (a) 1h, (b) 3h and (c) 5 h.

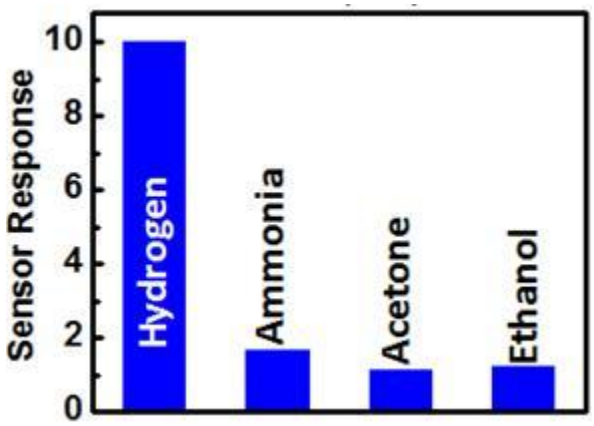

Figure 2.8: Cross-sensitivity of MoS_2-Pd composite to 50,000 ppm hydrogen, 50 ppm ammonia, 50,000 ppm acetone and ethanol.

Increasing the annealing time significantly improves the recovery of the sensor at the expense of reduced sensor response. For example, the recovery times/sensor responses are 83 s/10, 29 s/6, 28 s/4 for 1 h, 3 h and 5 h annealed samples, respectively. The SEM analysis (Figure 2.7) of the samples show that annealing changes the morphology of the film into a more spaced structure, which helps the recovery of the sensors. On the other hand, reduced sensor response could be explained by the fact that annealing turns MoS_2 flakes into a more agglomerated structure resulting in a decrease in the number of Pd NPs which contact to MoS_2 flakes.

We also investigated the cross-sensitivity of MoS_2-Pd composite to ammonia, ethanol and acetone. As shown in Figure 2.8, the sensor exhibits a sensor response of 10, 1.65, 1.13 and 1.22 to 50,000 ppm hydrogen, 50 ppm ammonia, 50,000 ppm acetone and ethanol, respectively, indicating that MoS_2-Pd has a little cross-sensitivity to these gases.

As a comparison, we fabricated graphene-Pd composite sensor and measured its electrical response to 50,000 ppm of H_2 (Figure 2.9), in which the graphene-Pd composite (Figure 2.10) shows a sensor response of only 1.34 with a response time of 102 s and incomplete recovery in 30 min. Unlike the MoS_2-Pd, the resistance of the graphene-Pd composite increases with H_2 exposure indicating that graphene-Pd composite are initially p-doped and the reduction in the work function of Pd upon H_2 exposure leads to partial depletion of holes in graphene increasing its resistance. It is clearly seen that the MoS_2-Pd composite exhibits superior hydrogen sensing performance than its graphene counterpart indicating that MoS_2 is more promising for room temperature hydrogen detection.

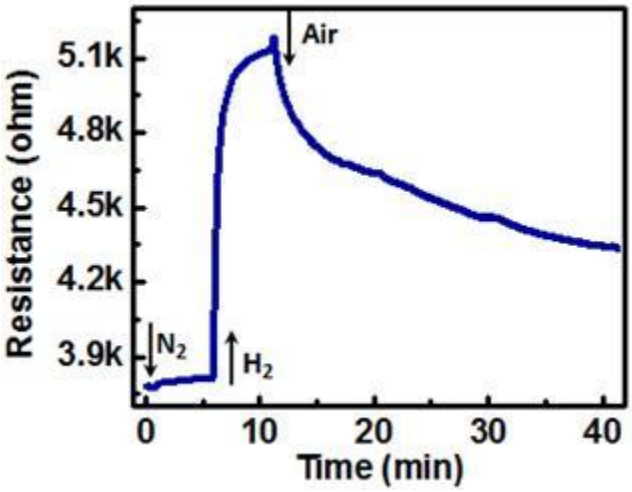

Figure 2.9: Electrical response of graphene-Pd composite to 50,000 ppm H_2.

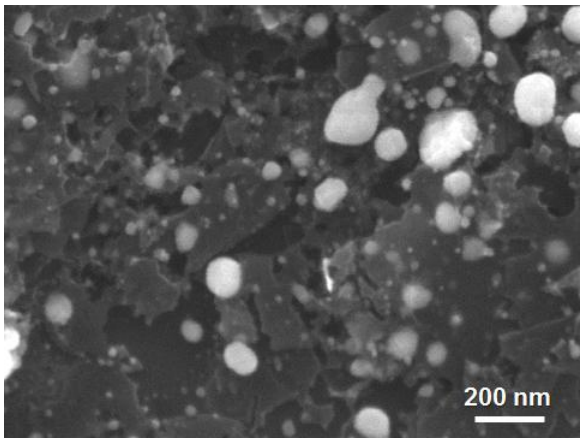

Figure 2.10: SEM image of graphene-Pd composite.

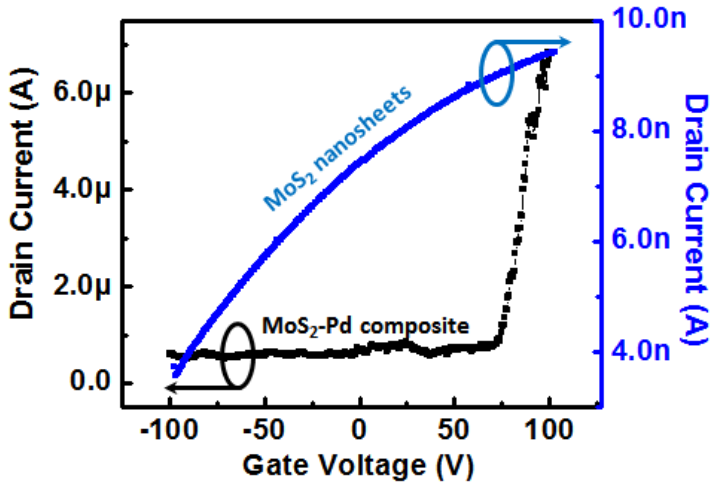

Figure 2.11: Drain current versus gate voltage of MoS_2 nanosheets and MoS_2-Pd composite.

In order to elucidate the sensing mechanism of the MoS_2-Pd composite, transport measurements were carried out by fabricating FET devices. Figure 2.11 shows the transport data of the MoS_2 nanosheets and MoS_2-Pd composite, in which the MoS_2 nanosheets and MoS_2-Pd composite both show n-type transport behavior with a large shift to the positive side in threshold voltage for the MoS_2-Pd composite. This indicates Pd NPs have a p-doping effect on MoS_2 causing partial depletion of electrons. Based on these results, we believe that the work function of Pd is higher than that of MoS_2 before H_2 exposure, which is consistant with the reported work function values of Pd (5.1 eV-5.6 eV) [113, 114] and MoS_2 (4.3 eV-5.2 eV) [115, 116]. After H_2 exposure, the work function of Pd decreases significantly resulting in a recovery of depleted electrons in MoS_2, which in turn reduces the overall resistance.

2.3 High-performance flexible hydrogen sensor made of WS_2 nanosheet-Pd nanoparticle composite film

Flexible hydrogen sensors offer the advantages of light-weight, high mechanical durability and wider range of applications, where flexibility is needed. For example, flexible hydrogen sensors can be useful as they could be utilized by wrapping around gas pipelines to monitor leaks. In this paper, we study an example of TMD-nanoparticle composite for hydrogen sensing, where chemically exfoliated WS_2 nanosheets are employed. A monolayer of WS_2 consists of a plane of W atoms sandwiched by two planes of S atoms [117]. WS_2 goes to indirect-to-direct band gap transition when exfoliated into monolayer sheets with a band gap value of 1.9 eV [118]. Moreover, 2H phase WS_2 (trigonal prismatic) is semiconducting while 1T phase (octahedral) WS_2 shows metallic behaviour [119]. Here, we present WS_2 nanosheet-Pd nanoparticle composite film fabricated on a flexible polyimide substrate for highly sensitive detection of hydrogen at room temperature. We study the sensing behaviour of the film with different concentrations of hydrogen and discuss the sensing mechanism qualitatively. Moreover, the sensing performance of the WS_2-Pd composite is compared to that of graphene-Pd composite. Furthermore, we investigate the effect of mechanical deformation on the sensor performance.

A. Experimental Methods

WS_2 nanosheet dispersion was prepared by probe sonication (Sonics, 750 W, 80% amplitude) of 400 mg of bulk WS_2 powder (Sigma Aldrich) in 80 mL of NMP (Sigma Aldrich) in an ice bath for 2 hours. The sonicated WS_2 solution was then centrifuged at

2000 rpm for 30 minutes to remove any remaining bulk WS_2 particles. After that, NMP was evaporated in a vacuum oven followed by redispersion of WS_2 nanosheets in deionized water with a concentration of 1 mg/mL. 10 mg $PdCl_2$ (Sigma Aldrich) was added into 10 mL of the WS_2 dispersion and then sonicated for 30 minutes. A few hundred µL of the WS_2-$PdCl_2$ solution (Figure 2.12a) was dropped on polyimide substrates (DuPont) and baked at 100 ^oC to remove the water. Subsequently, the casted films were annealed at 350 ^oC in N_2 environment for 1 h to reduce $PdCl_2$ to Pd and remove residual NMP. 10 nm/150 nm thick Ti/Au contacts were deposited by sputtering after defining a channel region with a 1 mm width and 10 mm length by using Teflon tape as a shadow mask. For the sensing measurements, H_2/N_2 gas mixture (Praxair) was flowed through a glass chamber (10 cm^3), where the sample is mounted. The concentration of the gas was adjusted to the desired values by diluting the starting gas (50,000 ppm H_2) with N_2 by using mass flow controllers (MKS). The total flow rate was kept at a constant value of 200 sccm (standard cubic centimeters per minute). The resistance of the sensor was recorded by a 2100 Keithley multimeter controlled by a computer interface. Scanning electron microscopy (SEM) images were taken with FEI SFEG UHR SEM. X-ray diffraction (XRD) measurements were conducted by a Bruker D2 Phaser X-ray diffractometer with Cu K-α (λ = 0.154 nm) as the radiation source. Raman spectroscopy measurements were carried out by an inVia Renishaw Raman microscope at 514.5 nm. Atomic force microscopy (AFM) image was acquired under tapping mode using a Nanoscope V multimode AFM (Bruker).

B. Results and Discussion

Figure 2.12b shows the optical image of the sensor device in bent state, clearly exhibiting its flexibility. We chose polyimide as the substrate since it can resist temperatures up to 400 ^{o}C enabling sensor operation under high environmental temperatures as well. The AFM image of WS_2 nanosheets dispersed on a Si substrate and the height profile of the corresponding line tracks are given in Figure 2.12c and d, in which the thicknesses of the sheets range from 3 to 50 nm and the lateral size varies between 50 to 500 nm. From the AFM analysis, it appears that laterally smaller sheets (smaller than 100 nm) have thicknesses less than 10 nm while the larger ones are relatively thicker.

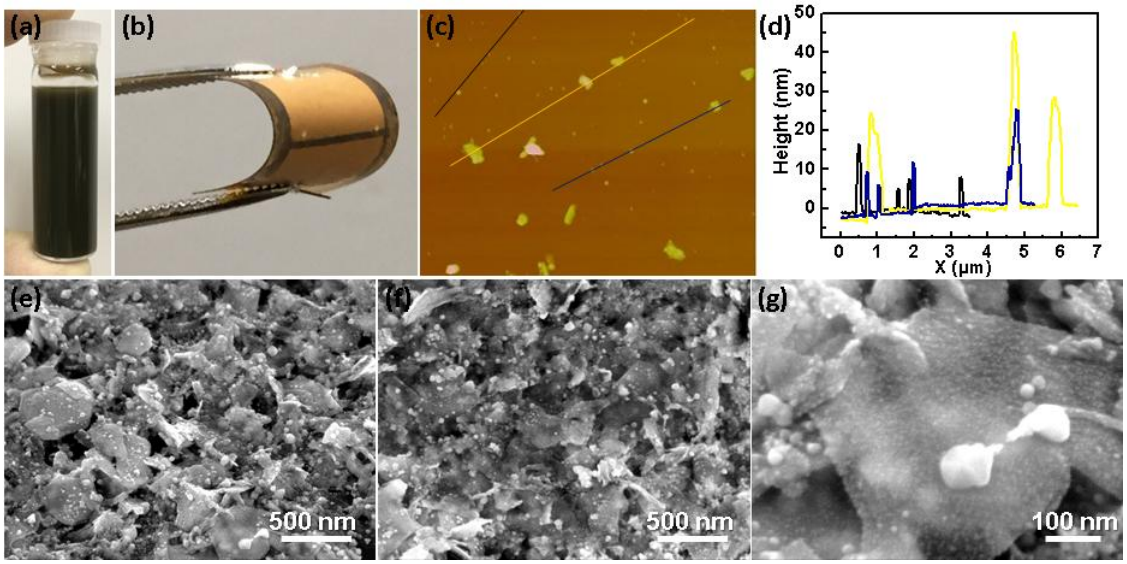

Figure 2.12: Optical image of (a) WS_2-$PdCl_2$ solution and (b) flexible WS_2 nanosheet-Pd nanoparticle composite hydrogen sensor. (c) AFM image of exfoliated WS_2 nanosheets dispersed on a Si substrate. (d) Height profile of the corresponding line tracks. Low magnification (e) tilted and (f) top-view, and (g) high magnification SEM images of WS_2 nanosheet-Pd nanoparticle composite film.

Low magnification tilted and top-view SEM images (Figure 2.12 e and f) show that WS_2-Pd composite forms a continuous film with a porous structure, which is favourable for gas sensing as it enhances response and recovery time. High magnification SEM image (Figure 2.12g) displays very fine Pd nanoparticles (~5 nm in diameter) and somewhat larger ones (~20-100 nm in diameter) adhered on the surface of WS_2 nanosheets with a good coverage. Pd ions in WS_2-$PdCl_2$ solution can anchor on the defects of WS_2, where unbound sulphur atoms exist and nucleate to form the nanoparticles [120]. For the best hydrogen sensing performance, it is important to maximize the density of the Pd nanoparticles without percolation. Otherwise, the conduction will be through the Pd nanoparticles due to low conductivity of WS_2 nanosheets. The cross-sectional SEM image shows that the average thickness of the film is around 2 μm (Figure 2.13).

We performed Raman spectroscopy and X-ray diffraction measurements to evaluate the structural properties of the WS_2-Pd composite film. Raman spectra of the bulk WS_2 and exfoliated WS_2 nanosheets dispersed on a SiO_2 coated Si substrates are given in Figure 2.14a, in which two main Raman features are observed for the both samples; a combination of in-plane E^1_{2g} mode and a second order longitudinal acoustic mode 2LA(M) appears at ~352 cm^{-1} and an out-of- plane A_{1g} mode at ~422 cm^{-1} [121, 122]. Figure 2.14b shows the X-ray diffraction patterns of the bulk WS_2 and WS_2 nanosheet-Pd nanoparticle composite film, corresponding to 2H phase WS_2. Note that some of the peaks disappear after exfoliation.

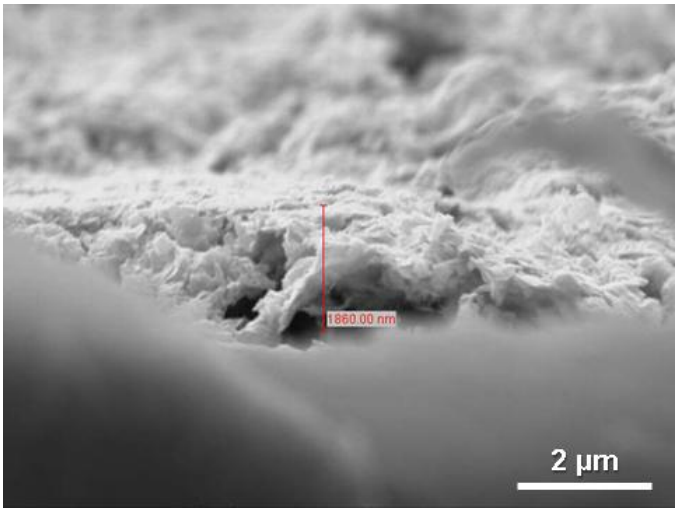

Figure 2.13: The cross-section SEM image of the WS_2-Pd composite film.

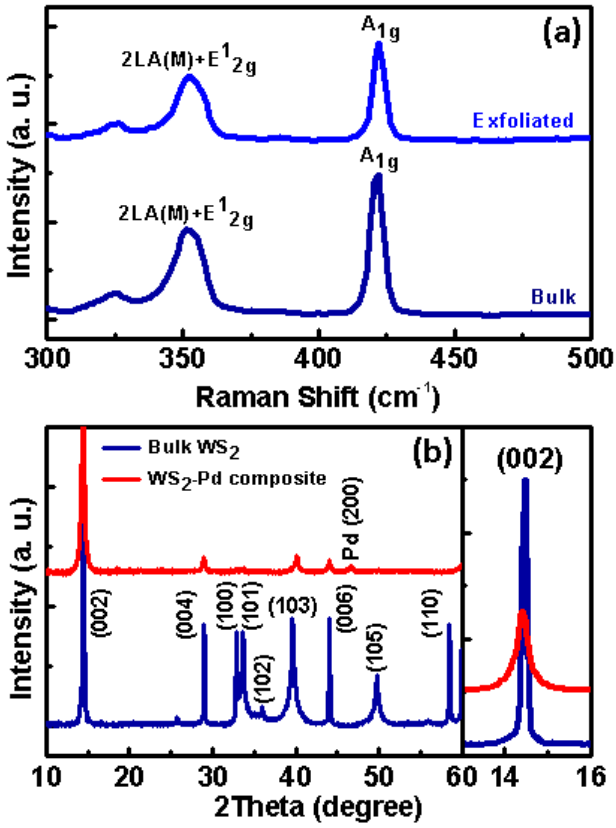

Figure 2.14: (a) Raman spectra of bulk and exfoliated WS_2. (b) XRD patterns of bulk WS_2 and WS_2-Pd composite.

Even after exfoliation, the intensity of the (002) peak remains considerably high suggesting that WS_S flakes tend to restack in the [002] direction. Moreover, there is a slight shift to lower angle in the position of the (002) peak due to the increased interlayer spacing. Furthermore, we observed an additional peak for the WS_2-Pd composite film, which corresponds to (200) plane of (fcc) Pd.

Prior to hydrogen sensing measurements, the chamber was purged with pure N_2 until the resistance of the sensor is stabilized in order to minimize the effect of N_2 (background gas) on the sensor response. Figure 2.15a shows the electrical response of the sensor to 50,000 ppm H_2 gas, in which the resistance decreases abruptly upon H_2 exposure followed by a slower decrease and saturation within a few minutes. When the H_2 flow is stopped and air is introduced into the chamber, the sensor shows a complete recovery. The sensitivity is defined as

$$S = R_1/R_2$$

where $R_1$and R_2 is the initial and the final resistance of the sensor, respectively. The response time is given as the elapsed time for the sensor to reach 90% of its total response and the recovery time to return to 90% of its initial resistance [123]. The WS_2-Pd composite exhibits a sensitivity of ~7.8 to 50,000 ppm H_2 and a response and recovery time of 119 s and 370 s, respectively. Current-voltage (I-V) curves of the sensor before and after H_2 exposure are given in Figure 2.15b. The sensor shows linear I-V behaviour both before and after H_2 exposure indicating that the contacts are Ohmic and the sensor response is dominated by the channel itself rather than the contacts. The sensing mechanism is based on a well-known process; formation of palladium hydride in the

presence of hydrogen, which results in a significant decrease in the work function of Pd [124]. In the absence of hydrogen, the work function of Pd (5.1-5.6 eV) [125] is lower than that of WS_2 (5.89 eV) [126], causing electron doping from Pd to WS_2. During H_2 exposure, the work function of Pd is decreased resulting in further electron doping of WS_2 and a corresponding reduction of resistance. The employment of the WS_2 nanosheets is essential as they provide a platform for the attachment of the Pd nanoparticles. The WS_2-Pd composite film can be considered as a three dimensional network of Pd anchored WS_2 nanosheets with a high sensing area. Moreover, the semiconducting WS_2 is advantageous as it provides high sensitivity. The recovery of the sensor is realized in the presence of O_2 when air is introduced into the chamber. One possible recovery mechanism was proposed by Lundström *et all* [127].

$$2H(a) + O_2(g) \leftrightarrow 2OH(a) \quad (1)$$

$$H(a) + OH(a) \leftrightarrow H_2O(g) \quad (2)$$

where index a and g address to adsorbed/absorbed and gas species, respectively. Oxygen in air reacts with atomic hydrogen dissolved in Pd forming hydroxyl groups (1). The hydroxyl groups then react with atomic hydrogen to form H_2O and desorbing it from Pd (2). To evaluate repeatability, the sensor was exposed to 7 sequences of 50,000 ppm H_2 for 10 s and air for 30 s, in which the sensor shows good repeatability (Figure 2.15c). In addition, we performed sensing measurements with different concentrations of H_2 ranging from 500 ppm to 50,000 ppm (Figure 2.15d). The sensitivity increases as the concentration of H_2 is increased.

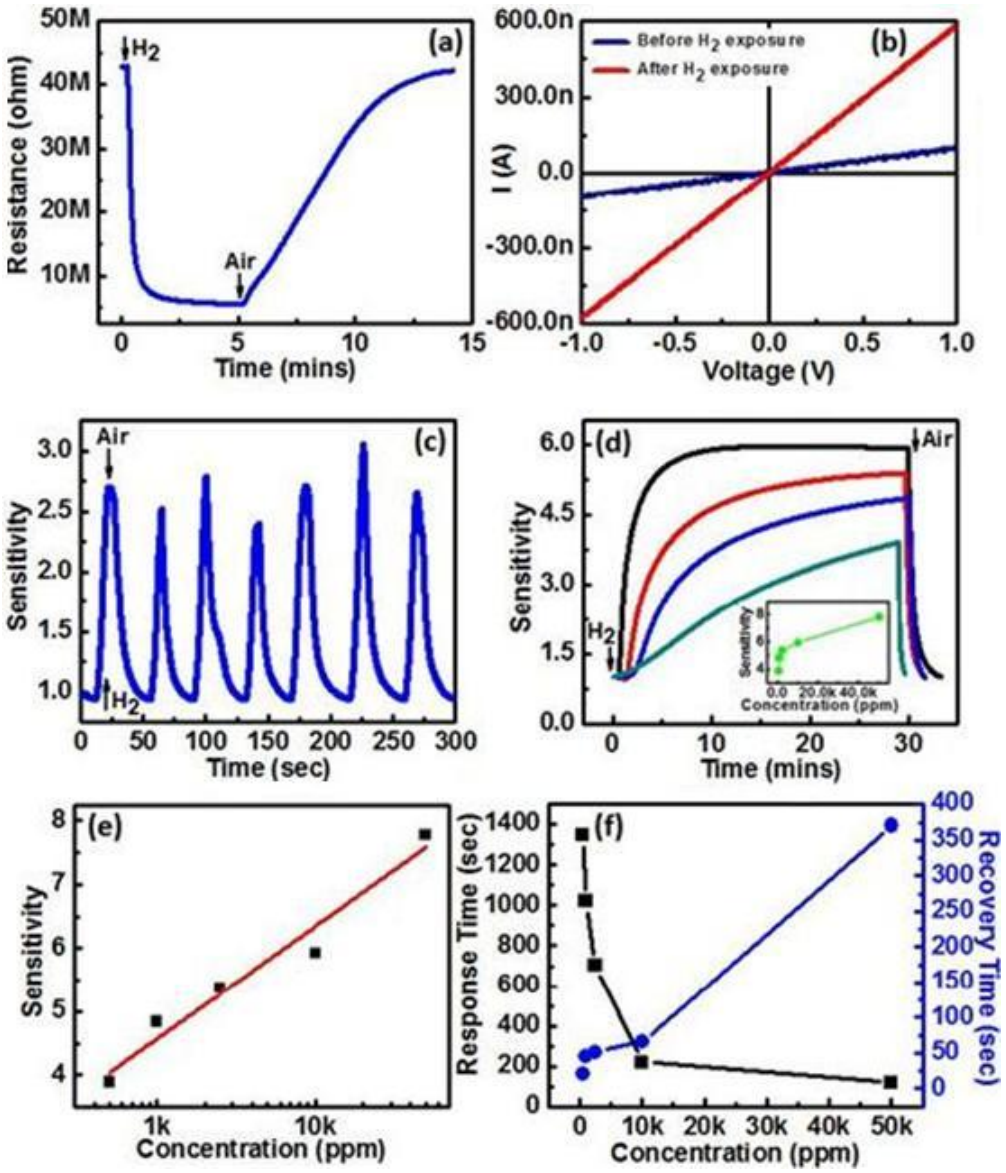

Figure 2.15: (a) Electrical response of the sensors to 50,000 ppm H_2. (b) Current-Voltage characteristics of the sensor before and after H_2 exposure. (c) Sensor response to sequences of 10 s H_2 (50,000 ppm) and 30 s air exposure. (d) Sensor response of the WS_2 nanosheet-Pd nanoparticle composite film to 10,000 ppm (black curve), 2500 ppm (red curve), 1000 ppm (blue curve) and 500 ppm (green curve) H_2. (Inset shows the sensitivity as a function of H_2 concentration.) (e) Sensitivity as a function of H_2 concentration on the logarithmic scale (f) Response and recovery time as a function of H_2 concentration.

The partial pressure of H_2 determines the total amount of H_2 uptake in Pd in accordance with the Sieverts' law [128]:

$$x = Kp^{1/2}$$

where x is the amount of hydrogen absorbed in Pd ($mol.m^{-3}$), K is the Sievert's coefficient, or hydrogen solubility in Pd at room temperature with a value of 27.1 $mol.m^{-3}.Torr^{-1/2}$, and p is the partial pressure of the hydrogen gas (Torr) and is related to the concentration in accordance with $p \sim 760H$, where H is the unitless concentration. As the concentration of H_2 is increased, its partial pressure is increased and more hydrogen is absorbed into Pd lattice causing a larger change in the work function of Pd and in the resistance of the sensor. For example, the amount of hydrogen absorbed in Pd was calculated to be 16.7 and 167 $mol.m^{-3}$ at 500 and 50,000 ppm H_2 concentrations, respectively. When the sensitivity is plotted against H_2 concentration on the logarithmic scale (Figure 2.15e), the data can be fitted into the following equation;

$$S = -0.74 + 1.77\log(H)$$

where H is the concentration of hydrogen in the unit of ppm. Based on the equation, a detectable response of S=1.03 can be achieved for 10 ppm H_2. The response and recovery time is plotted as a function of the concentration of H_2 in Figure 2.15f. The response time increases from 119 s to 1349 s as the concentration is reduced from 50,000 ppm to 500 ppm whereas the recovery time decreases from 370 s to 21 s. At equilibrium state, the hydrogen adsorption and desorption rates are equal [74]:

$$k_a p(1-\Theta)^2 = k_d \Theta^2$$

where $k_a p(1-\Theta)^2$ is the adsorption and $k_d \Theta^2$ is the desorption rate, k_a is the adsorption and k_d is the desorption rate constant, p is the partial pressure or the concentration of H_2 and $(1-\Theta)$ is the fraction of available Pd sites. Initially, the sensor response is fast because $(1-\Theta)$ is high and the response slows down as the number of available Pd sites is decreased, which results in a fin-shaped behaviour in the sensitivity-time curves. At low concentrations, the response time is significantly high due to the slow adsorption rate. On the other hand, recovery rate of the sensor is initially high, and it slows down substantially as the number of occupied Pd sites is decreased. The recovery time became dramatically shorter when the concentration of H_2 is decreased since only a smaller portion of the Pd sites are occupied.

For comparison, we also tested the hydrogen sensing performance of graphene-Pd composite film fabricated similarly to WS_2-Pd. The sensor exhibits a sensitivity of about 1.14 (Figure 2.16), which is significantly lower than that of the WS_2-Pd. The superior sensing performance of the WS_2-based sensor can be explained in terms of conductivity. The conductivity of a semiconductor is given as:

$$\sigma = q(N_e \mu_e + N_h \mu_h)$$

where q is the elementary charge, N_e and N_h are the number of electrons and holes per cm^3, μ_e and μ_h are the electron and hole mobility, respectively. By assuming that mobility change with hydrogen exposure is negligible [26], the change in conductance is dominated by the change of carrier densities. At room temperature, the number of the charge carriers which contributes to the conduction is small due to the large band gap of WS_2.

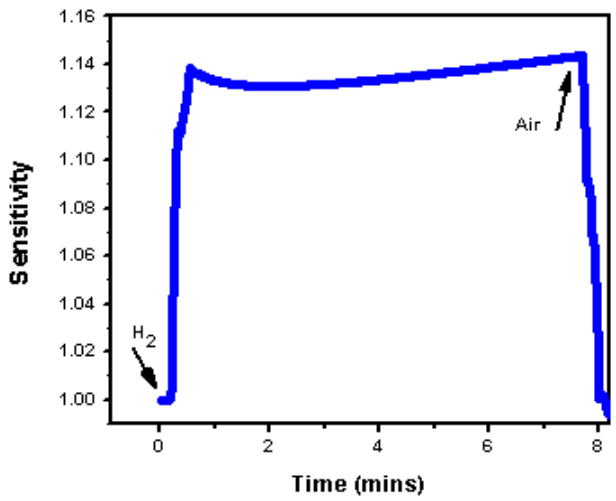

Figure 2.16: Sensing performance of graphene-Pd composite with 50,000 ppm H_2.

The density of electrons in WS_2 can be dramatically enhanced by electron doping effect of palladium hydride. On the other hand, graphene is a zero band gap material with higher density of charge carriers. The relative resistance change of the sensor upon hydrogen exposure is proportional to $\Delta N/N$, where ΔN is the change in the carrier density and N is the initial carrier density. The ΔN is equal for graphene and WS_2 since it is determined by the work function change of Pd due to hydrogen exposure. However, N is significantly lower for WS_2 due to its large band gap; therefore, the relative impact of the change of the carrier density on the conductivity is more profound for WS_2. This is consistent with the observations of Sun *et all* [129], where Pd modified semiconducting CNTs shows much higher sensitivity to hydrogen in compared to metallic CNTs.

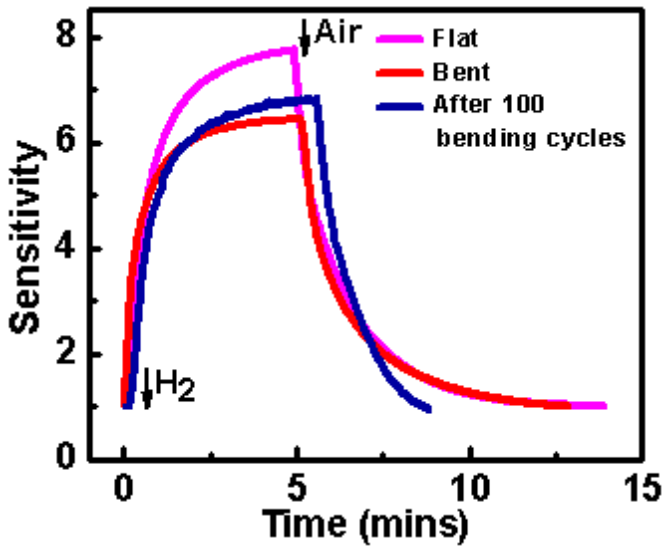

Figure 2.17: Comparative hydrogen sensing performance of the WS_2-Pd composite film in flat and bent geometry as well as after 100 bending cycles.

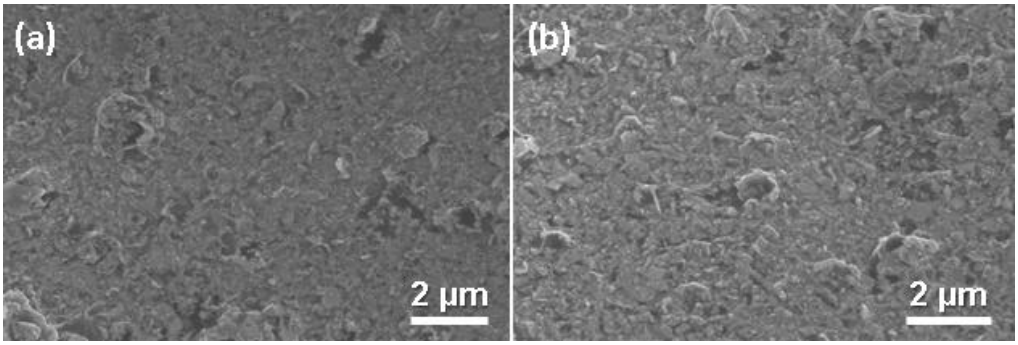

Figure 2.18: SEM images of the WS_2-Pd composite film (a) before and (b) after 100 bending-releasing cycles.

In order to evaluate the suitability of WS_2-Pd composite film as a flexible sensor, we tested its hydrogen sensing performance under mechanical deformations by wrapping it around a cylindrical surface. Figure 2.17 represents the sensor response to 50,000 ppm H_2 in flat and bent states and also after 100 bending cycles with corresponding sensitivities of 7.8, 6.4 and 6.8, respectively. Even though there are slight variations, no serious performance degradation occurred. We further examined the sensors' mechanical stability by SEM analysis before and after the bending cycles, in which no obvious structural change was observed in the WS_2-Pd composite film indicating that its high mechanical durability (Figure 2.18).

2.4 Summary

In conclusion, we demonstrated highly sensitive detection of hydrogen at room temperature by employing solution-processed MoS_2 nanosheet-Pd nanoparticle composite, which can be readily fabricated by a facile solvent exfoliation and drop casting method. In particular, the MoS_2-Pd composite sensor exhibits a sensor response of around 10 to 50,000 ppm H_2 with a response and recovery time of 40 s and 83 s, respectively. Pd NPs enable sensitivity to hydrogen based on work function modulation of Pd providing high sensitivity, fast response and recovery. The recovery time can be further decreased down to 28 s by increasing the annealing time. Moreover, we demonstrated a flexible hydrogen sensor by employing a WS_2 nanosheet-Pd nanoparticle composite film fabricated on a polyimide substrate. The sensor exhibits an excellent hydrogen sensing performance in flat and bent states and can sustain several bending cycles, proving its robustness. In addition, TMDs-based sensors show dramatically higher

sensitivity than that of graphene-based sensor, which was attributed to the low carrier densities in TMDs due to their large band gaps. These results indicate that chemically exfoliated TMDs hold great potantial for the inexpensive and scalable fabrication of high sensitivity, room temperature chemical sensors.

Chapter 2, in part, has been published in Advanced Science in 2015 by Cihan Kuru, Chulmin Choi, Alireza Kargar, Duyoung Choi, Young Jin Kim, Chin Hung Liu, Serdar Yavuz and Sungho Jin. Chapter 2, in part, has been submitted to Nanotechnology by Cihan Kuru, Duyoung Choi, Alireza Kargar, Chin Hung Liu, Serdar Yavuz, Edward Choi, Sungho Jin and Prabhakar R. Bandaru. The dissertation/thesis author was the primary investigator and author of these papers.

CHAPTER 3: GRAPHENE/SILICON HETEROJUNCTION SOLAR CELLS

3.1 Introduction

There has been a great interest to develop next generation solar cells by employing nanomaterials such as nanowires, quantum dots, carbon nanotubes (CNTs), and graphene. Recently, solar cells incorporating CNTs and silicon have been studied, in which the efficiencies in the range of 7-15% have been achieved by using carbon nanotubes (CNTs) as a top contact for n type silicon (n-Si) [130-132]. CNTs form a Schottky contact to n-Si due to their work function difference. The Schottky barrier height can be increased by chemical doping of CNTs enabling improved charge separation at the CNT/Si interface [133]. However, forming a CNT film on Si substrate is challenging due to cylindrical geometry of CNTs and a significant part of the surface remains uncovered; thus, reducing the junction area. In this regard, employing graphene is a more practical choice owing to its 2D nature. Graphene has drawn much attention since its discovery [134] owing to its exceptional electronic, optical and mechanical properties. Its atomic thickness, high carrier mobility, high transparency and flexibility make it attractive for solar cells. Graphene sheets can be grown by Chemical Vapor Deposition (CVD) on a copper foil and can be transferred onto Si readily. By combining graphene and n-Si, a Schottky type solar cell has been demonstrated [135], where graphene is used as a transparent electrode. When graphene is put in contact with n-Si, a built-in voltage is introduced near the interface of graphene/n-Si due to the p-type nature of graphene in air. Photons are absorbed in Si and generate electron-hole pairs, which are separated by the graphene/n-Si junction, where the holes are driven to the graphene and electrons to the Si.

However, the PCEs (power conversion efficiency) are reported to be in the range of 1-3% [136, 137] for the pristine graphene/n-Si solar cells, which is lower than those reported for CNTs/n-Si solar cells. The PCEs around 4.4% have been reported for pristine graphene/methyl terminated Si solar cells [138, 139]. Furthermore; a doping strategy has been used to increase the performance of graphene/Si heterojunction solar cells. Strong oxidizing agents such as HNO_3, $SOCl_2$ and H_2O_2 have been employed to hole dope graphene, leading to significant increase in the PCEs due to the increase in built-in voltage and the reduction in resistance losses [140-143].

3.2 Gold nanoparticle decorated graphene/silicon heterojunction solar cells

In this study, we have achieved an improvement in the PCE by a factor of ~12 through Au nanoparticle decoration on graphene combined with HNO_3 (nitric acid) doping. Au nanoparticles significantly reduce series resistance of the cell, in turn improving FF (fill factor). There is a trade-off between the reduction of R_s (series resistance) and the optical transmittance. The optimum thickness of Au was found to be around 1 nm for the maximum cell performance. On the other hand, HNO_3 doping enhances the V_{OC} (open circuit voltage) as well as further reducing the R_s. The cell behaviour was investigated by analysing the dark and light I-V curves of various cells and extracting the cell parameters such as PCE, V_{OC}, J_S (short circuit current) , FF, R_s, n (ideality factor) and $\emptyset$ (Schottky barrier height).

A. Experimental Methods

We constructed a Ti/Au window (2 mmx2 mm) on n-Si wafers (0.5-1 ohm-cm) covered with 300 nm SiO_2 layer by photolithography, following with sputter deposition

of Ti/Au (10/150 nm thickness). The backside of the wafer was Ar plasma treated inside the sputtering chamber to remove any native oxide and Ti/Au (10/150 nm) was deposited to form the back contact. A second photolithography step was performed to define a smaller window (0.0025 cm^2 area) inside the Ti/Au one. SiO_2 layer inside the smaller window, where graphene is put in contact with underlying n-Si, was then etched away by Buffered Oxide Etchant (BOE, NH_4F:HF in a 6:1 ratio) for 10 minutes. Before graphene transfer Si substrate was kept in ambient for 30 minutes in order to passivate the dangling bonds of Si. CVD grown graphene on Cu foil (from ACS materials) was spin coated with Poly(methyl methacrylate) (PMMA) and the backside graphene was removed by oxygen plasma etching. After that, the Cu foil was cut into 1 cmx1 cm pieces and the Cu foil was removed by dissolving with 0.1 M ammonium persulfate. Floating PMMA/graphene layer was transferred into deionized water to clean and remove residual chemicals. The floating PMMA/graphene layer was then picked up onto the target substrate and allowed to dry in air overnight. The PMMA layer was removed in acetone followed by annealing in N_2 environment for one hour at 400 °C to remove any trapped water between graphene and Si and promote a better contact. Finally, Au was evaporated on graphene with 0.2 A/s deposition rate in a Temescal e-beam evaporator, in which the thickness was monitored by a thickness sensor. Graphene/n-Si solar cell device was glued on a Cu foil and Cu wires were connected to the front and back Ti/Au contacts using silver epoxy for the J (current density)–V (voltage) measurements. Graphene was doped with HNO_3 vapor by placing it a few milimeters away from liquid HNO_3 in a glass beaker. J-V characteristics of the solar cell devices were evaluated with a solar simulator (Newport 66905) and a Keithley 2420 source meter under standard illumination conditions (AM 1.5, 100

mW/cm^2). Optical transmittance measurements were conducted with a Unico S1100 UV/Vis spectrophotometer. Scanning electron microscopy (SEM) images were taken with Phillips XL30 ESEM. The surface coverage of the Au nanoparticles was estimated by Image J software.

B. Results and Discussion

The optical image of the final solar cell device is shown in Figure 3.1. Graphene is visible on the Ti/Au frame as a light yellow region. Figure 3.2 displays the SEM images of 0.5 nm, 1 nm and 2 nm Au deposited on graphene, respectively. It is clearly seen that Au nanoparticles are formed at these thicknesses rather than a continuous film. The average diameter and surface coverage of the nanoparticles are 9 nm, 10 nm, 16 nm and 14%, 23%, 19% for the respective order. As the deposition thickness is increased, the diameter of the nanoparticles is increased. Surprisingly, the surface coverage shows a decrease for 2 nm Au deposition, which is most likely due to coalescence of the nanoparticles, resulting in less dense yet larger particles.

Figure 3.3 exhibits the optical transmittance spectra of Au deposited on glass substrates at various thicknesses, in which the transmittance is decreased as the thickness of the Au is increased. On the other hand, transmittance spectra exhibit dips at certain wavelengths, which are caused by the plasmonic effect of the Au nanoparticles. The incoming light interacts with the electrons in metal nanoparticles causing them oscillate at certain frequencies called plasmon frequency [144]. The plasmonic dips are located at 550 nm, 564 nm, 613 nm and 644 nm for 0.5 nm, 1 nm 2 nm 3 nm Au depositions, respectively.

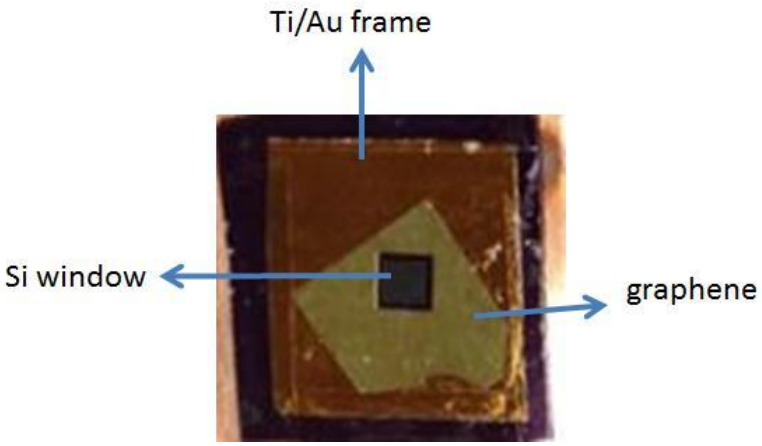

Figure 3.1: The optical image of the graphene/n-Si solar cell device.

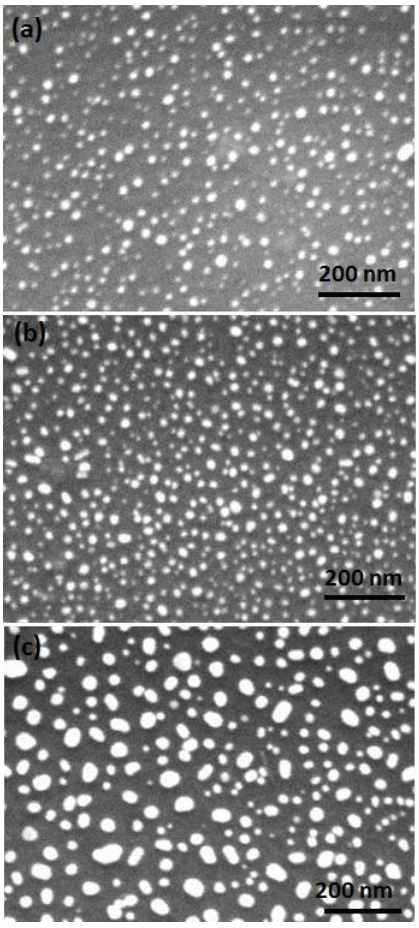

Figure 3.2: SEM images of (a) 0.5 nm, (b) 1 nm and (c) 2 nm Au deposited on graphene.

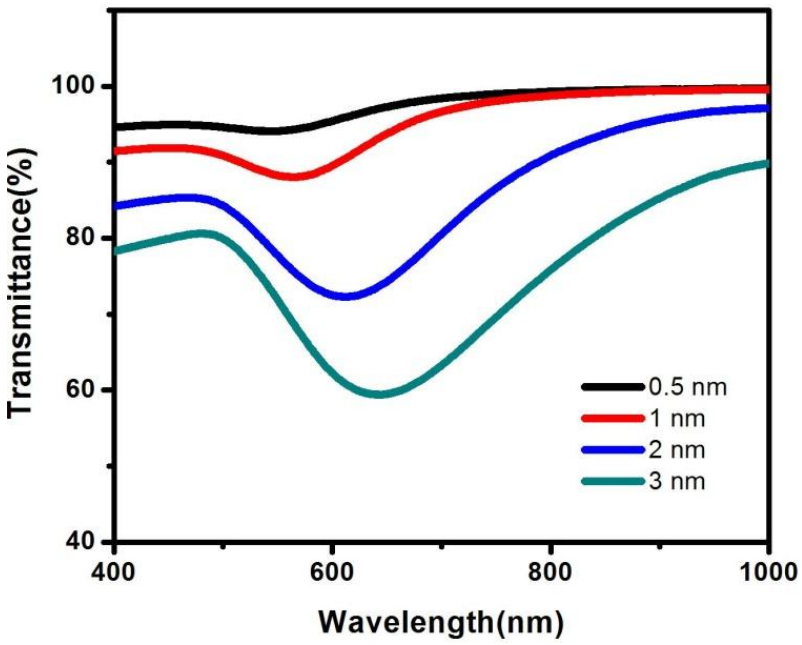

Figure 3.3: Transmittance spectra of 0.5 nm, 1 nm, 2 nm and 3 nm Au deposited on glass substrates.

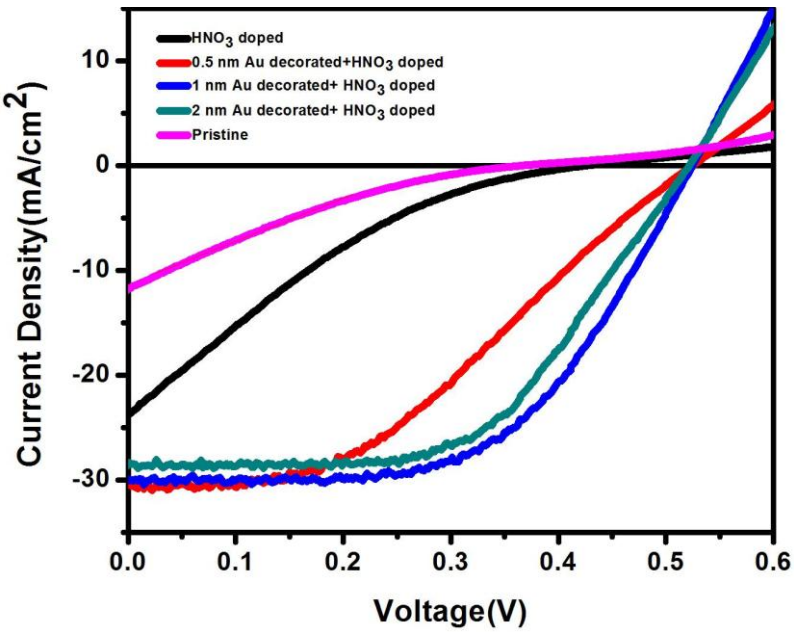

Figure 3.4: J-V characteristics of the pristine, HNO_3 doped, 0.5 nm Au deposited and HNO_3 doped, 1 nm Au deposited and HNO_3 doped and 2 nm Au deposited and HNO_3 doped graphene/n-Si solar cells.

The plasmon frequency is shifted to the longer wavelengths because of the increased nanoparticle size [145]. Furthermore, the dips are broadened for the increased Au thickness due to the averaging over the different size of nanoparticles [145].

J-V characteristics of the cells are compared in Figure 3.4 under illumination. Pristine graphene/n-Si cell shows a J_S of 11.7 mA/cm^2, V_{OC} of 0.36 V, FF of 17% and a PCE of 0.76%. The PCE is low for the pristine graphene/n-Si cell because of the high sheet resistance of graphene (~1.2 kohm), which results in dramatic resistance losses degrading the cell performance. The HNO_3 doped cells show slightly improved cell performance, in which the J_S, V_{OC}, FF and PCE are 23.7 mA/cm^2, 0.42 eV, 17% and 1.69%, respectively. HNO_3 induces p-type doping effect on graphene; therefore, increases the building potential at the interface of graphene/n-Si, which results in enhanced charge collection efficiency. As a result, J_S and V_{OC} are improved while FF remains unchanged. On the other hand, Au nanoparticle decorated and HNO_3 treated graphene/n-Si cells exhibit dramatically enhanced solar cell performance. A maximum PCE of 9% was achieved for 1 nm Au deposited and HNO_3 treated cells. The significant enhancement of PCE is mainly due to the increased FF and J_S, which stems from the reduced series losses. Au nanoparticles serve as conduction pathways for the charge carriers improving the conductivity of graphene considerably. Moreover, Au nanoparticles induces further p-type doping on graphene improving the V_{OC} to 0.52 eV. We extracted the R_s of the cells from J-V curves under illumination by using the following equation [146];

$$R_s = 2(V_{OC}/J_{SC} - A/J_{SC}^2 - k_B T/qJ_{SC}),$$

where R_s is the series resistance, A is the area of the J-V curve, k_B is the Boltzmann constant, T is the temperature and q is the elementary charge. The calculated R_s values are 25 ohm.cm^2, 14 ohm.cm^2, 10.2 ohm.cm^2, 6.2 ohm.cm^2 and 6.9 ohm.cm^2 for pristine, HNO_3 doped, 0.5 nm Au deposited and HNO_3 doped, 1 nm Au deposited and HNO_3 doped and 2 nm Au deposited and HNO_3 doped, respectively. Both HNO_3 doping and Au nanoparticle decoration significantly reduces the series resistance of the cells owing to the increased conductivity of graphene. Note that 1 nm Au deposition results in the maximum surface coverage and hence, it gives the minimumR_s. We also investigated the plasmonic effect of the Au nanoparticles on the solar cell performance through analysing the J in the reverse bias region in order to eliminate the drastic effect of the series resistance. The J value abruptly decays due to the high series resistance of the pristine graphene cell; therefore, comparing J_{SC} is not reliable to determine the plasmonic effect of the nanoparticles on the cell performance. Figure 3.5 compares the J-V curves of the pristine and Au nanoparticle decorated and HNO_3 doped graphene/n-Si cells under illumination in the reverse bias region, in which the average J value of pristine graphene/n-Si cell is around 30.1 mA/cm^2. After 0.5 nm Au deposition and HNO_3 doping J slightly increased to 30.7 mA/cm^2 while J decreased to 29.7 mA/cm^2 and 28.7 mA/cm^2 for the 1 nm and 2 nm Au deposited graphene/n-Si cells, respectively. The incident light is scattered into the Si or absorbed by the spherical metal nanoparticles [145].

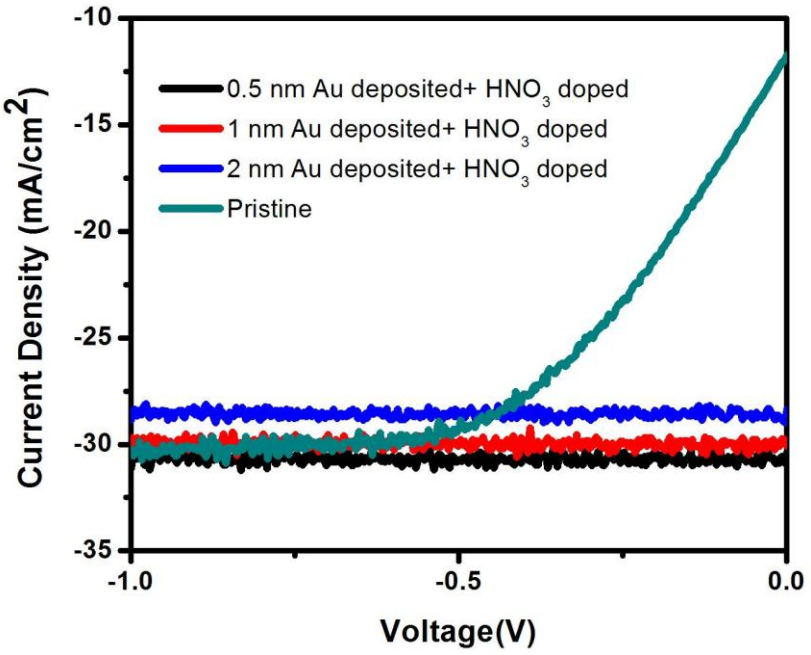

Figure 3.5: J-V curves the pristine, 0.5 nm Au deposited and HNO_3 doped, 1 nm Au deposited and HNO_3 doped and 2 nm Au deposited and HNO_3 doped graphene/n-Si solar cells in the reverse bias region.

The scattering and absorption of the light is given by [145];

$$C_{abs} = (2\pi/\lambda)Im[\alpha] \text{ and } C_{sc} = (1/6\pi)(2\pi/\lambda)^4|\alpha|^2,$$

where α is the given by $\alpha = 3V(\varepsilon - 1)/(\epsilon + 1)$, where V is the volume and ϵ is the permittivity of the particles. For 0.5 nm Au deposited cell, the scattering effect dominates while the absorption of the light by Au nanoparticles overrides for 1 nm and 2 nm Au deposited cells. In order to achieve the maximum scattering effect, the size and distribution of the nanoparticles needs to be adjusted to optimum values.

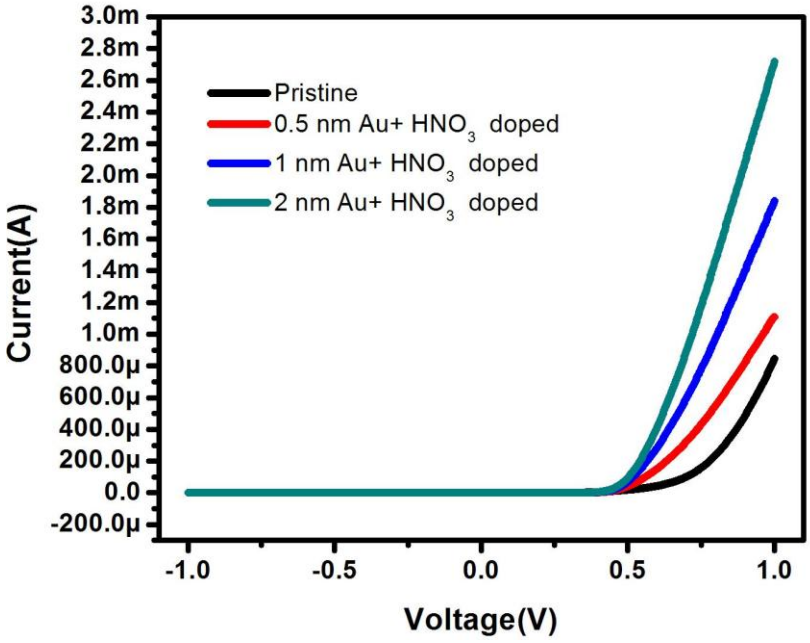

Figure 3.6: Dark I-V curves of the pristine, 0.5 nm Au deposited and HNO_3 doped, 1 nm Au deposited and HNO_3 doped and 2 nm Au deposited and HNO_3 doped graphene/n-Si solar cells.

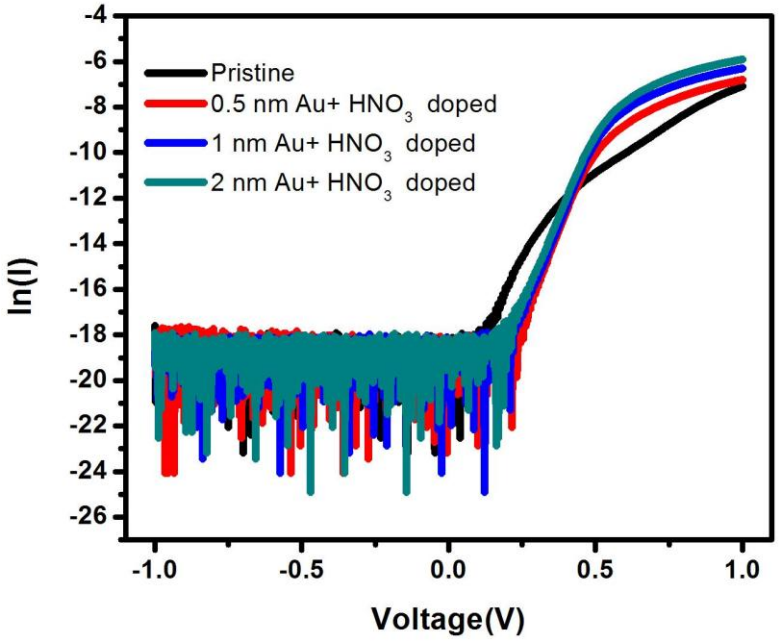

Figure 3.7: Dark ln(I)-V curves of the pristine, 0.5 nm Au deposited and HNO_3 doped, 1 nm Au deposited and HNO_3 doped and 2 nm Au deposited and HNO_3 doped graphene/n-Si solar cells.

The dark I-V curves of the cells are given in Figure 3.6, in which all the cells exhibit good diode behavior. The diode parameters such as n and $\emptyset$ can be used to evaluate the quality of the graphene/n-Si junction. I-V characteristics of a Schottky diode is given by

$$I = I_S[\exp((qV_a)/kT) - 1] \text{ and } I_S \text{ is expressed as } I_S = AA^*T^2\exp(-q\emptyset/kT),$$

where I_S is the reverse saturation current, A is the junction area, A^* is the Richardson constant and given as 112 A/cm^{2}K^2 for n type Si [147], T is absolute temperature, q is the elementary charge and k is the Boltzmann constant. The $\emptyset$ can be extracted from the from the intercept of the linear portion of ln(I) at zero voltage [148]. On the other hand, the ideality factor can be calculated using the slope of the linear portion of the ln(I) versus V curve (Figure 3.7) and placing it in the following equation [148].

$$n = (q/kT)/slope$$

The extracted diode parameters are given in Table 3.1 in which, the n values are 1.55, 1.24, 1.22 and 1.26 for the pristine, 0.5 nm Au deposited and HNO_3 doped, 1 nm Au deposited and HNO_3 doped and 2 nm Au deposited and HNO_3 doped cells, and the $\emptyset$ values are 0.80 eV, 0.90 eV, 0.90 eV and 0.89 eV for the respective order. Upon the Au nanoparticle deposition and HNO_3 doping, the ideality factor approaches to the ideal value of n =1 and the Schottky barrier height increases signifying that the quality of the graphene/n-Si junction is improved.

This study suggests that Au nanoparticle decoration on graphene along with HNO_3 doping significantly reduces the series resistance of the graphene/n-Si solar cells and increase the Schottky barrier height of graphene/n-Si junction, in turn improving the fill factor, short circuit current, open circuit voltage and power conversion efficiency.

Table 3.1: Diode parameters of the pristine, 0.5 nm Au deposited and HNO_3 doped, 1 nm Au deposited and HNO_3 doped and 2 nm Au deposited and HNO_3 doped graphene/n-Si solar cells.

Samples	Ideality Factor (n)	Schottky barrier height (Ø)
Pristine graphene/n-Si	1.55	0.80 eV
0.5 nm Au deposited and HNO_3 doped graphene/n-Si	1.24	0.90 eV
1 nm Au deposited and HNO_3 doped graphene/n-Si	1.22	0.90 eV
2 nm Au deposited and HNO_3 doped graphene/n-Si	1.26	0.89 eV

3.3 The effect of PMMA antireflection coating on the solar cell performance

Polished Si substrates have reflectance as high as about 40% in the wavelength range of 400 to 1100 nm; hence significant portion of the incoming light is reflected back yielding lower power conversion efficiencies. One strategy is to use an antireflection coating, which possesses a suitable refractive index and optimum thickness for the maximum performance. The optimum refractive index for the antireflection coating is given by [149];

$$n_{opt} = (n_{Si} n_{air})^{1/2},$$

where n_{Si} is the refractive index of Si (~4) [150] and n_{air} is the refractive index of air (~1), yielding n_{opt}= 2. The refractive index of PMMA is 1.49 [151], which is close to the optimum refractive index value of the antireflection coating for Si solar cells. The optimum thickness of the antireflection layer needs to be adjusted to a value, where the destructive interference of light occurs in the visible region since the intensity of the solar

spectrum is the maximum in this region. The destructive interference of the light should satisfy the following expression [152];

$$d = \lambda/4n,$$

where d is the thickness of the antireflection layer is, λ is the wavelength of the light and n is the refractive index of the antireflection layer. For 600 nm wavelength, d equals to 100 nm for the PMMA antireflection layer.

The graphene/n-Si solar cell devices were fabricated as described previously. For the antireflection coating, PMMA A2 (Micro Chem) was spin coated on graphene at 1000 rpm, resulting in a thickness of about 100 nm. The solar cell devices were tested under standard illumination conditions (AM 1.5, 100 mW/cm^2).

Figure 3.8 exhibits the J-V curves of 1 nm Au deposited and HNO_3 doped solar cell before and after the PMMA antireflection coating under illumination. Upon the PMMA coating, the J_{SC} is enhanced by 20%, clearly showing its antireflection effect. On the other hand, V_{OC} slightly decreased from 0.52 to 0.50 V due to desorption of HNO_3 molecules from the graphene surface during the spin coating of the PMMA. As a result, the amount of p-doping on graphene is decreased and therefore, the conductivity of graphene. This led to an increase in the series resistance of the cell from 6.2 to 10.3 ohm.cm^2 and a corresponding decrease in the FF from 57.8% to 32%, degrading the overall PCE from 9% to 5.7%.

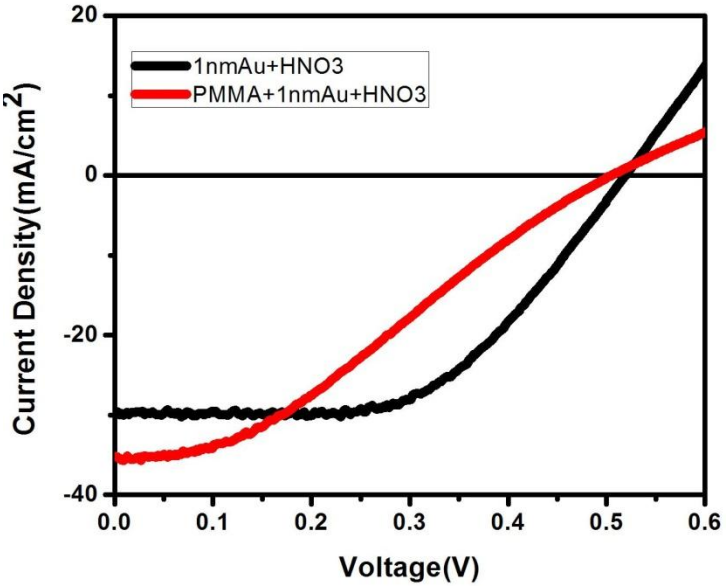

Figure 3.8: J-V characteristics of 1 nm Au deposited and HNO_3 doped graphene under illumination before and after PMMA antireflection coating.

In conclusion, we studied the antireflection effect of PMMA coating on graphene/n-Si solar cells, in which a noticeable improvement in the J_{SC} was achieved. However, PMMA coating degraded the p-doing effect of HNO_3, which resulted in a decrease in the PCE. If the degradation of the HNO_3 doping could be prevented, 20% improvement in the J_{SC} would yield a PCE of 10.8%.

3.4 Enhanced power conversion efficiency of graphene/silicon heterojunction solar cells through NiO induced doping

Doping graphene with strong oxidizers is an effective method to increase the V_{OC} and the conductivity of graphene, which results in significant performance increase in the graphene/Si solar cells. However, such molecules are extremely volatile, hence can desorb from graphene surface quickly diminishing the doping effect. For example, Lancellotti *et al.* reported that the PCE of nitric acid doped graphene/Si solar cell

decreased from 3.4% to 1.8% after 15 days [153]. On the other hand, Miao *et al.* have reported bis-(trifluoromethanesulfonyl) amide (TFSA) dopant for graphene, obtaining a PCE of 8.6%; however it is not clear whether the TFSA-doped graphene is stable over long time [154].

In this study, we present a novel doping strategy of using NiO nanoparticle film for the graphene/n-Si solar cells, achieving a substantial improvement in the solar cell performance. Metal oxides such as MoO_3, V_2O_5, WO_3 and NiO have been previously employed in organic solar cells as a hole transporting layer owing to their high work function [155, 156]. NiO, a wide-bandgap material, serves as a transparent hole doping agent for graphene/n-Si solar cells, improving the short circuit current (J_{SC}), V_{OC}, FF and PCE. We show that NiO doping reduces the series resistance as well as improving the junction quality of the cells. Furthermore, the stability of the cells is investigated by monitoring different solar cell parameters during 10 days.

A. Experimental Methods

We constructed a Ti/Au window (3.2 mmx3.2 mm) on n-Si wafers (0.5-1 ohm-cm) covered with 300 nm SiO_2 layer by photolithography, following with sputter deposition of Ti/Au (10/150 nm thickness). The backside of the wafer was Ar plasma treated inside the sputtering chamber to remove any native oxide and Ti/Au (10/150 nm) was deposited to form the back contact. A second photolithography step was performed to define a smaller window (0.09 cm^2 area) inside the Ti/Au one. SiO_2 layer inside the smaller window, where graphene is put in contact with underlying n-Si, was then etched away by Buffered Oxide Etchant (BOE, NH_4F:HF in a 6:1 ratio) for 10 minutes. Before

graphene transfer Si substrate was kept in ambient for 30 minutes in order to passivate the dangling bonds of Si. CVD grown graphene on Cu foil (from ACS materials) was spin coated with Poly(methyl methacrylate) (PMMA) and the backside graphene was removed by oxygen plasma etching. After that, the Cu foil was cut into 1 cmx1 cm pieces and the Cu foil was removed by dissolving with 0.1 M ammonium persulfate. Floating PMMA/graphene layer was transferred into deionized water to clean and remove residual chemicals. Finally, the floating PMMA/graphene layer was picked up onto the target substrate and allowed to dry in air overnight. PMMA layer was then removed in acetone followed by annealing in N_2 environment for one hour at 400 °C to remove any trapped water between graphene and Si and promote a better contact. Final structure of the solar cell device is schematically depicted in Figure 3.9a. NiO nanoparticles (Alfa Aesar, the particle size is less than 50 nm) were dispersed in ethanol with a concentration of 5 mg/mL and then NiO nanoparticle containing solution was spin coated onto the graphene at 1000 rpm for a few times until the NiO nanoparticles reach the maximum surface coverage. (Figure 3.9b) Graphene/n-Si solar cell device was glued on a Cu foil and Cu wires were connected to the front and back Ti/Au contacts using silver epoxy for the J (current density)–V (voltage) measurements. J-V characteristics of the solar cell devices were evaluated with a solar simulator (Newport 66905) and a Keithley 2420 source meter under standard illumination conditions (AM 1.5, 100 mW/cm^2). Optical transmittance measurements were conducted with a Unico S1100 UV/Vis spectrophotometer. Raman characterization was performed with a Renishaw RM1000 with a wavelength of 514 nm.

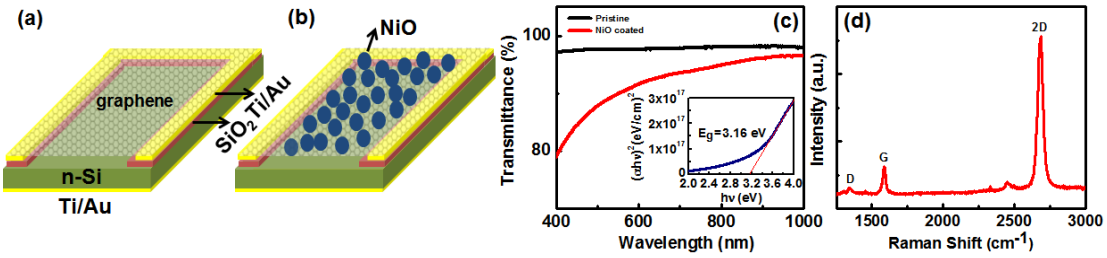

Figure 3.9: Schematic representations of graphene/n-Si solar cell device (a) before and (b) after NiO spin coating. (c) Optical transmittance spectra of pristine and NiO coated graphene (Inset shows the Tauc plot for NiO nanoparticles.). (d) Raman spectra of pristine graphene.

B. Results and Discussion

The optical transmittance of pristine and NiO coated graphene is shown in Figure 3.9c, in which pristine graphene has 97% transmittance at 550 nm wavelength while the NiO coated graphene exhibits 89% transmittance at the same wavelength. This indicates that NiO coating does not significantly block the incident light in the visible region due to the large band gap of NiO. In order to quantify the exact band gap value of NiO nanoparticles, Tauc plot ($\alpha^2h^2\nu^2$ vs $h\nu$), where α is the absorption coefficient and $h\nu$ is the photon energy, was obtained from the absorbance spectra of NiO nanoparticles dispersed in ethanol with a concentration of 0.3 mg/mL. The extrapolation of the linear portion of the curve to zero yields the band gap value [157], in which the obtained band gap value of NiO nanoparticles is 3.16 eV (Inset Figure 3.9c).

Figure 3.9d shows the Raman spectroscopy data of the pristine graphene sample utilized, which exhibits the main Raman features of pristine graphene; D (1341 cm^{-1}) peak related to defects, G (1586 cm^{-1}) peak associated with bond stretching of carbon atoms and 2D (2682 cm^{-1}) peak originated from the double resonance process [158]. As shown in the figure, the small intensity ratio of D peak to G peak (I_D/I_G of 0.28) indicates

a low defect density in graphene [159]. Also, the intensity of G peak is smaller than the half intensity of 2D peak (intensity ratio of 2D peak to peak, I_{2D}/I_G, 5.8), with the 2D peak being sharp and symmetric suggesting that graphene is predominantly single layer [160].

The J-V characteristics of pristine and NiO doped graphene/n-Si solar cell at dark and under illumination are shown in Figure 3.10. It is important to note that the presented data belongs to the same sample before and after NiO coating. Dark current of NiO doped graphene/n-Si solar cell has a higher turn-on potential than that of pristine graphene/n-Si cell because a higher built-in potential is formed at the graphene/Si interface as a result of NiO doping. The pristine and NiO doped graphene/n-Si solar cells exhibit J_{SC} of 17.2 mA/cm^2 and 19.4 mA/cm^2, V_{OC} of 0.40 V and 0.51 V, FF of 20 % and 49 % and PCE of 1.37 % and 4.91%, respectively, in which we clearly see the effect of NiO doping. The increase in the J_{SC} and FF is resulted from the reduction in the series resistance of the cells. It is worth noting that charge carrier injection from NiO nanoparticles have a negligible contribution to the J_{SC} as NiO has a large band gap and can't generate substantial amount of photo-excited charge carriers in the wavelength regions under investigation. In order to quantify the change in the series resistance upon NiO doping, the series resistance was calculated by computing the area under the J-V curves under illumination according to the method reported elsewhere [146]. $R_S = 2(V_{OC}/J_{SC} - A/J_{SC}^2 - k_BT/qJ_{SC})$, where R_S is the series resistance, A is the area of the J-V curve, k_B is the Boltzmann constant, T is the temperature and q is the elementary charge. We extracted a series resistance of 24 ohm.cm^2 and 10 ohm.cm^2 for pristine and NiO doped graphene/n-Si cells, respectively.

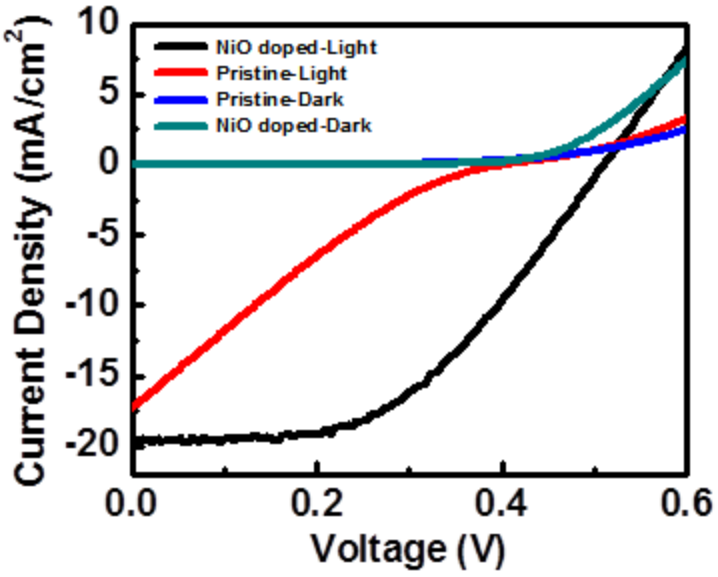

Figure 3.10: Dark and light J-V curves of pristine and NiO doped graphene/n-Si solar cells.

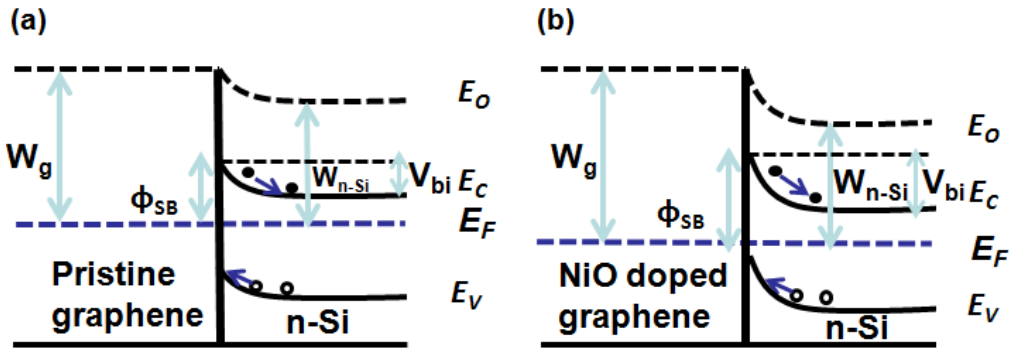

Figure 3.11: Energy-band diagram of (a) pristine and (b) NiO doped graphene/n-Si.

NiO doping also improves the V_{OC} of the cells due to the hole doping effect of NiO. A Schottky junction is formed near the interface of graphene/n-Si in accordance with $\phi = W_g - \chi_{Si}$, where W_g is the work function of graphene and χ_{Si} is the electron affinity of n-Si (Figure 3.11a). NiO is a p-type semiconductor with the reported work function values of between 5 and 6 eV [161-163]. Through considering the work function of pristine graphene (4.5 eV) [164], NiO leads to significant hole doping of graphene, which results in a higher Schottky barrier height (Figure 3.11b). In order to substantiate the hole doping effect of the NiO nanoparticles on graphene, we calculated the Schottky barrier height from $\phi = (kT/q)\ln(A^* T^2/J_0)$, where A^* is the effective Richardson constant, which is 112 A/cm^{2}K^2 for n-Si [147] and J_0 is the reverse saturation current density, which was extracted from the intercept of the linear portion of ln(I) at zero voltage [147].

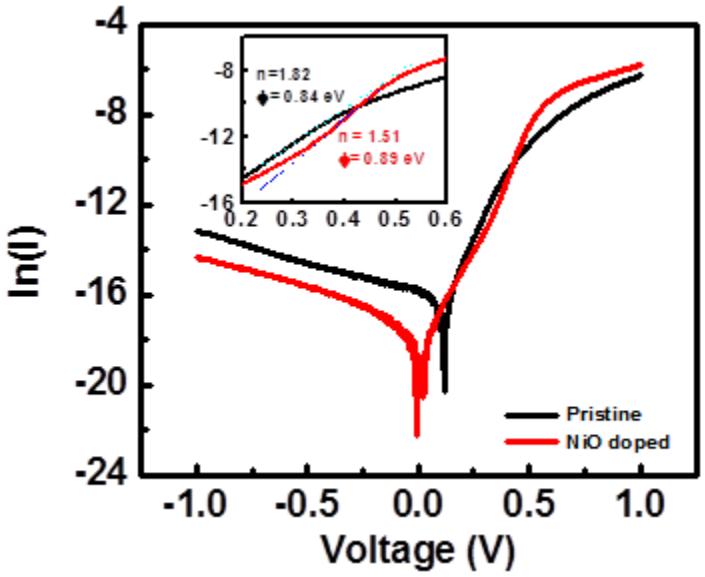

Figure 3.12: Dark ln(I)-V curves of pristine and NiO doped graphene/n-Si solar cells.(Inset shows the ideality factor and Schottky barrier height of the corresponding cells.)

The extracted J_0 and ϕ values are 0.73 x 10^{-7}, 0.84 x 10^{-8} A/cm^2 and 0.84 eV, 0.89 eV for pristine and NiO doped graphene/n-Si cells, respectively, translating to work function values of 4.89 eV and 4.94 eV. The increase in the work function of graphene upon NiO coating signifies that graphene is indeed hole doped by NiO nanoparticles. In order to evaluate the quality of the pristine and NiO doped graphene/n-Si Schottky junctions, we extracted ideality factor (n) from the slope of the linear portions of dark ln(I)-V curves [148] (Figure 3.12). We obtained the ideality factors of 1.82 for the pristine and 1.51 for NiO doped graphene cells, which clearly shows that NiO doping improves the quality of the junction.

The J-V curves of NiO doped graphene/n-Si cell under illumination were collected during 10 days (Figure 3.13a). During that time, the samples were not encapsulated with any additional materials and were stored in a laboratory under ambient conditions. The solar cell parameters were plotted in Figure 3.13b, in which the Voc, Jsc and FF and the PCE exhibit small fluctuations, however no significant performance drop was observed. The little variations could be explained by the changes in the laboratory ambient conditions such as humidity or unintentional doping from various gas molecules which exist in the laboratory air. In compared to the HNO_3 doped graphene/Si solar cells, in which the PCE drops significantly after a few days [153], the NiO doped graphene/Si solar cells exhibit highly stable solar cell performance owing to the stable doping effect of NiO on graphene.

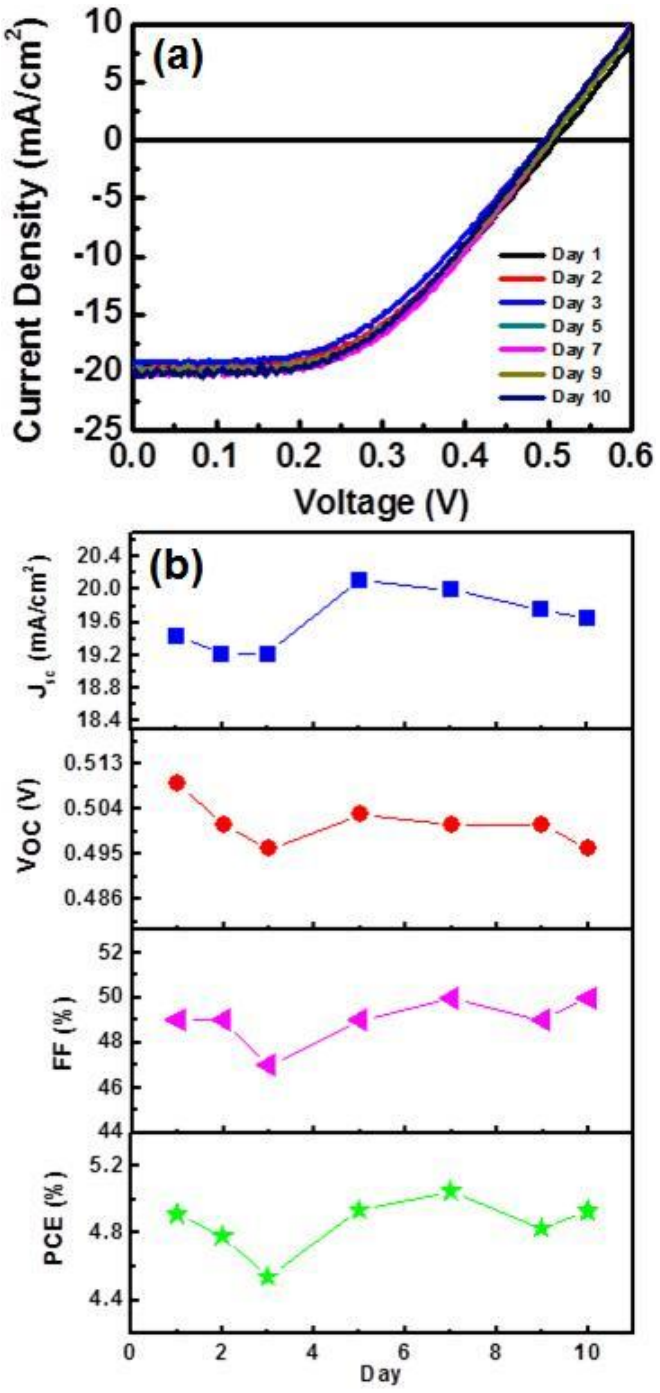

Figure 3.13: (a) J-V curves of the NiO doped graphene/n-Si solar cell under illumination during 10 days. (b) J_{SC}, V_{OC}, FF and PCE of the corresponding sample as a function of day.

In conclusion, we have shown enhanced PCE in the NiO doped graphene/n-Si solar cells, in which NiO nanoparticles are employed as a hole doping material for graphene owing to its high work function and optical transparency. The NiO doping increased the PCE from 1.37 to 4.91 % as a result of the improvements in the V_{OC}, J_{SC} and FF, which is attributed to the enhanced built-in voltage and reduced series resistance. Additionally, the NiO doping improves the ideality factor and increases the Schottky barrier height of the cells verifying the hole doping effect of NiO on graphene. Furthermore, we studied the stability of the solar cell devices stored under ambient conditions. After 10 days, the devices showed no performance degradations indicating that NiO is a promising material for stable p-type doping of graphene.

3.5 Summary

We have demonstrated graphene/n-Si heterojunction solar cells, in which graphene is employed as highly transparent and conductive electrode which forms a Schottky junction to n-Si. The power conversion efficiency of the cells was improved significantly through Au nanoparticle decoration in combination with HNO_3 doping. The Au nanoparticles dramatically lower the series resistance of the solar cell devices while HNO_3 doping improves the Schottky barrier height as a result of its hole doping effect on graphene, in turn enhancing the power conversion efficiency from 0.76% to 9%. We demonstrated PMMA as an efficient antireflection layer for the graphene/n-Si solar cells, in which the J_{SC} was improved by 20% due to the reduced reflection of incoming light from the Si surface. Moreover, we showed that NiO coating on graphene improves the PCE by a factor of ~ 3.5 owing to its hole doping effect on graphene. We observed no

degradation in the device performance over the 10 days of measurements indicating the stability of the NiO doping.

Chapter 3, in part, has been accepted for publication in Journal of Nanoscience and Nanotechnology. Cihan Kuru, Serdar Yavuz, Alireza Kargar, Duyoung Choi, Chulmin Choi, Cyrus Rustomji, Sungho Jin and Prabhakar R. Bandaru. The dissertation/thesis author was the primary investigator and author of this paper.

CHAPTER 4: MoS_2 NANOSHEET-Ru NANOPARTICLE COMPOSITE: AN ADVANCED CATALYST FOR HYDROGEN EVOLUTION

4.1 Introduction

Today, energy is an important part of our lives and the demand for energy has been increasing as the world population grows. Energy sources can be divided into three main categories: fossil fuels, nuclear energy and renewable energy. Fossil fuels are formed by decomposition of dead organisms, resulting in oil, coal and natural gas. They are considered as non-renewable energy sources as the formation of fossil fuels take millions of years. Fossil fuels contain high percentage of carbon; therefore, when burned they produce large amount of carbon dioxide, which is known to cause greenhouse effect and contribute to global warming. Nuclear energy is used to generate electricity through producing heat as a result of nuclear fission reactions. It causes small amount of carbon dioxide emission; however, the nuclear waste is a critical issue for the environmental safety. On the other hand, renewable energy is a clean and abundant energy source which includes sun, wind, hydropower and biofuels. Even though renewable energy is preferred, its usage is limited by the provincial distribution of wind power, sun illumination and hydropower. Figure 4.1 compares the amount of energy sources used worldwide in 2013, in which the fossil fuels are the main energy sources utilized to meet world's energy demand. The dependence on fossil fuels can be reduced by utilizing hydrogen as an energy source. Fuel cells can burn hydrogen producing electricity according to the following reaction [165]:

$$2H_2 + O_2 \rightarrow 2H_2O, \qquad \Delta H = -286\ kJ/mol$$

1 mol of hydrogen can produce 286 kJ energy, which is equivalent to 143 kJ/g indicating the largest energy density among the chemical fuels. Having high power density and being lightweight makes hydrogen very attractive as a fuel, especially for transportation and space applications.

Hydrogen can be produced from hydrocarbons through reacting them with water steam at high temperatures [167]. This reaction also produces carbon dioxide. For hydrogen to be an alternative to fossil fuels, it needs to be produced from clean and abundant energy sources such as water. Indeed, electrolysis [168] and thermolysis [169] of water and photo-catalytic water splitting [170] can produce hydrogen, whose byproduct is only water when burned with oxygen. At elevated temperatures, water molecules can be split into atomic hydrogen and oxygen. For example, half of the water molecules can be dissociated at 3000 ^{o}C [169].

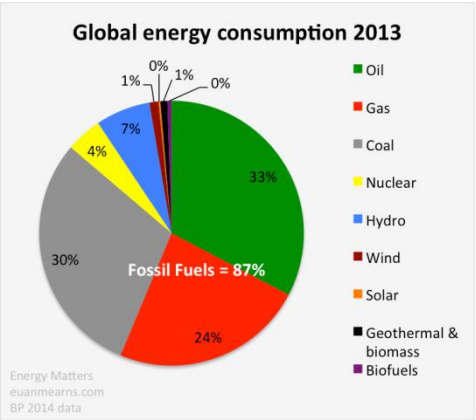

Figure 4.1: Global energy consumption in 2013 [166].

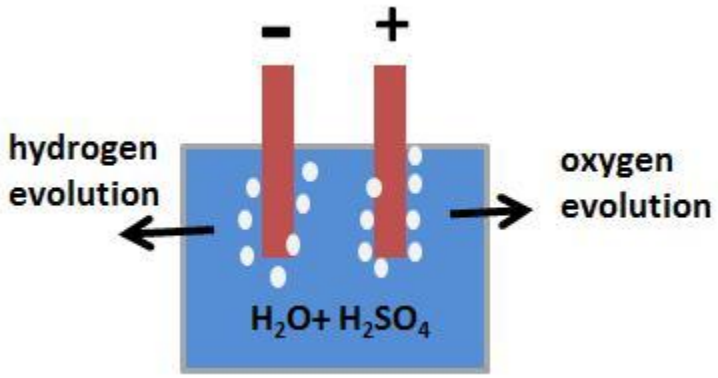

Figure 4.2: Schematic depiction of electrolysis of water.

This method requires harsh conditions and is not practical for commercial applications. Water molecules can be also dissociated by passing an electrical current through it as shown schematically in Figure 4.2 [168]. At negatively charged cathode, electrons are given to hydrogen cations, forming hydrogen gas according to the following reaction:

$$2H^+(aq) + 2e^- \rightarrow H_2(g)$$

At the positively charged anode, water oxidation occurs:

$$2H_2O \rightarrow O_2 + 4H^+(aq) + 4e^-$$

The overall reaction is:

$$2H_2O(l) \rightarrow 2H_2(g) + O_2(g)$$

The hydrogen and oxygen evolution reactions are dictated by the catalytic properties of the cathode and anode materials used. For hydrogen evolution, Pt, Ir, Rh and Pd are known to be the good catalysts [171]; however, they are highly expensive and not abundant. Therefore, there is an urgent need to find earth abundant materials to replace

the precious metals. Recently, MoS_2 has been shown to be an excellent catalyst for the hydrogen evolution reaction. For the hydrogen evolution reaction to proceed, hydrogen atoms first have to bind to the catalyst. For a good hydrogen catalyst, the free energy of hydrogen atom bound to the catalyst should be close to zero ($\Delta G \approx 0$) [172]. DFT calculations showed that the free energy of hydrogen adsorbed on the edges of MoS_2 is on the order of 0.1 V, which is equivalent to Pt [173]. Studies have shown that only the edges of MoS_2 are active sites for hydrogen evolution since the basal plane is thermodynamically unfavorable for hydrogen adsorption [173]. Dai reported the synthesis of MoS_2 nanoparticles on reduced graphene oxide and showed a high hydrogen evolution activity with small overpotentials and small Tafel slopes, which was attributed to the existence of rich edge sites and good electronic coupling of MoS_2 and reduced graphene oxide [174]. It was also reported that 1T phase metallic MoS_2 nanosheets produced by lithium intercalation method show a better hydrogen evolution performance compared to the 2H phase semiconducting MoS_2 owing to their high conductivity [175]. 3D MoS_2-graphene composites have been demonstrated as efficient catalysts for hydrogen evolution with high hydrogen production rate and excellent stability [176]. In addition, Li demonstrated a 3D MoS_2 sponge on Ni foam fabricated by thermolysis of ammonium tetrathiomolybdate at high temperatures [177].

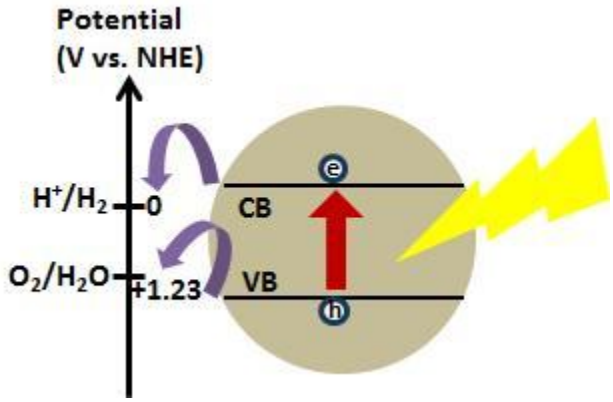

Figure 4.3: Schematic depiction of photocatalytic water splitting event.

On the other hand, hydrogen can be produced through photo-catalytic water splitting, in which semiconductor materials are used as electrodes. The photocatalytic water splitting is shown schematically in Figure 4.3. Under illumination, photons are absorbed by the semiconductor generating electron-hole pairs. The excited electrons in the conduction band of the semiconductor reduce water to form hydrogen gas while the holes generated in the valance band oxidize water to form oxygen gas. For the mentioned charge transfer to occur between the semiconductor electrodes and the water, the conduction band minimum has to be higher than hydrogen evolution potential (0V vs. NHE) whereas the valance band maximum has to be lower than oxygen evolution potential (1.23V vs. NHE) [178]. Therefore, the band gap value of the semiconductor, hence the energy of the photons absorbed has to be larger than 1.23 eV.

In this study, we show enhanced hydrogen evolution performance of MoS_2 nanosheets with Ru nanoparticle decoration. We prepared the MoS_2-Ru composite films by solution processing, which is desirable for inexpensive and mass scale fabrication. The electrocatalytic hydrogen evolution performance of the MoS_2-Ru composite was

compared to pristine MoS_2 and Ru, in which the MoS_2-Ru composite exhibits the best performance. This study indicates that hydrogen evolution performance of the MoS_2 nanosheets can be significantly enhanced by loading a metal cocatalyst on the basal plane of the MoS_2 nanosheets, which provides additional active sites for hydrogen evolution as well as improving the charge transfer.

4.2 Experimental methods

MoS_2 nanosheets in NMP were prepared as described in Chapter 2. Subsequently, NMP was evaporated in a vacuum oven, followed by redispersion of MoS_2 nanosheets in H_2O with a concentration of 1.5 mg/mL. 15 mg of $RuCl_2$ was added into 10 mL of MoS_2/H_2O solution and then the resultant solution was sonicated for 30 minutes. The unbound Ru salt was removed by centrifuging the solution at 15000 rpm for 20 minutes. The working electrodes were prepared by drop casting of the resultant solution on FTO substrates, followed by annealing in N_2 environment at 400 ^oC to reduce $RuCl_2$. In order to make a comparison, we also prepared working electrodes made of pristine MoS_2 nanosheets by drop casting the same amount of MoS_2 solution. On the other hand, Ru working electrode was prepared by drop casting of $RuCl_2$ solution (1.5mg/mL $RuCl_2$ in H_2O) and a subsequent annealing in N_2 at 400 ^oC to reduce $RuCl_2$. SEM images were taken with Philips XL30 ESEM. The EDX characterization was conducted with Oxford EDX and Inca software. The electrochemical measurements were conducted in a 0.5 M H_2SO_4 solution with a three electrodes configuration, which includes a working electrode, Pt counter electrode and an Ag/AgCl reference electrode. The electrochemical measurements were collected using a potentiostat (Digi-Ivy, DY2300) with a scan rate of

0.01 V/s. During the measurements, a constant agitation was applied using a magnetic stirrer bar and the solution was purged with N_2. The area of the samples was determined with Image J software.

4.3 Results and discussion

Figure 4.4a and b shows the SEM images of the drop casted MoS_2-Ru film and a single MoS_2 flake decorated with Ru nanoparticles, respectively. It is clearly seen that Ru nanoparticles (5- 10 nm in diameter) are adhered on the surface of the MoS_2 flake. On the other hand, the MoS_2-Ru composite film exhibits a good uniformity with a porous structure, which is advantageous for water splitting owing to the increased surface area. The presence of Ru was confirmed by EDX measurements, which is given in Figure 4.5.

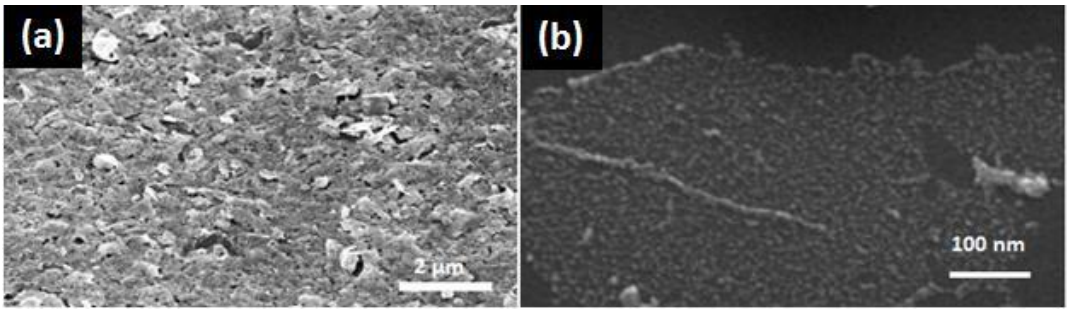

Figure 4.4: SEM images of (a) MoS_2-Ru composite and (b) single MoS_2 nanosheet decorated with Ru nanoparticles.

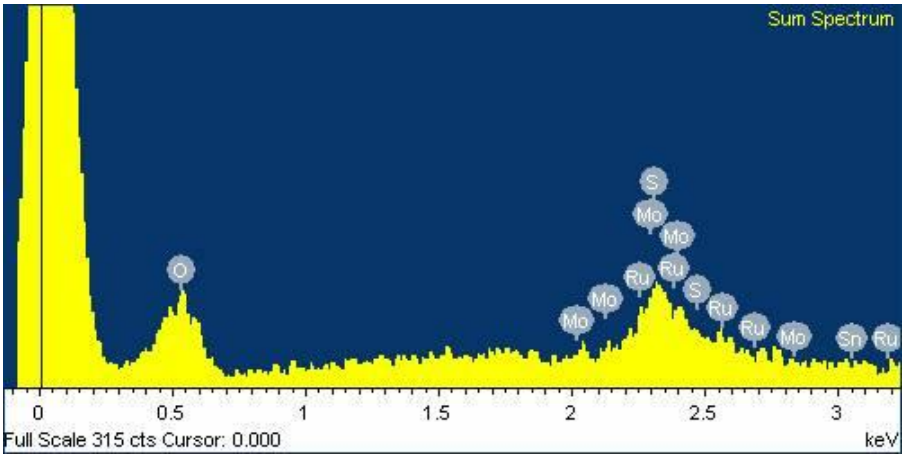

Figure 4.5: EDX spectra of the MoS_2-Ru composite.

The electrochemical hydrogen evolution performance of the pristine MoS_2, Ru and MoS_2-Ru composite is compared in Figure 4.6a. The potential versus Ag/AgCl was converted to RHE (reversible hydrogen electrode) by using the following equation [179]:

$$E_{RHE}=E_{Ag/AgCl}+0.059pH+0.199$$

The pristine MoS_2 exhibits a high onset potential of 500 mV. The onset potential is the potential value at which hydrogen evolution starts. Hence, a small onset potential is desired for practical applications. On the other hand, the Ru and MoS_2-Ru composite show onset potentials of ~200 mV and ~100 mV, respectively (Table 4.1). Even though pure Ru shows good hydrogen evolution performance, the combination of the MoS_2 and Ru gives the best performance owing to the smaller onset potential. We also compared the current densities at -0.2V vs RHE, in which the pristine MoS_2, pure Ru and MoS_2-Ru composite possess current densities of 0.02 mA/cm^2, 4.34 mA/cm^2 and 35.4 mA/cm^2, respectively.

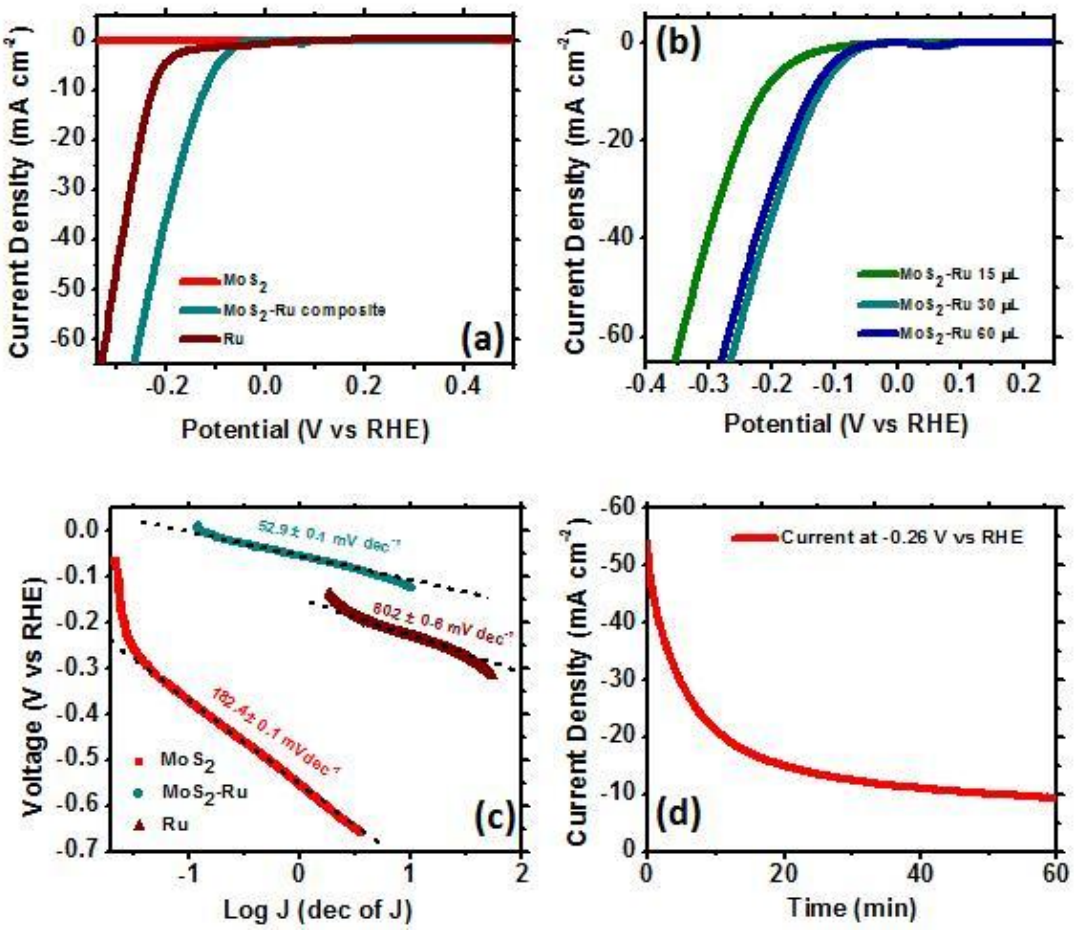

Figure 4.6: (a) Electrochemical hydrogen evolution performance of the MoS_2, Ru and MoS_2-Ru composite. (b) Electrochemical hydrogen evolution performance of the MoS_2-Ru composite films prepared by drop casting of different amounts of the MoS_2-$RuCl_2$ solution. (c) Tafel plots of the MoS_2, Ru and MoS_2-Ru composite. (d) Stability test of the MoS_2-Ru composite at -0.26 V vs RHE over 60 minutes.

Table 4.1: The extracted onset potential, Tafel slope and current density at -0.2 V vs RHE values of the pristine MoS_2, Ru and MoS_2-Ru composite.

Samples	Onset potential (mV)	Tafel slope (mV/dec)	Current density (mA/cm^2) at -0.2 V
MoS_2	500	182	0.02
Ru	200	80	4.34
MoS_2-Ru	100	53	35.4

The significant improvement is mainly attributed to the improved charge transfer of the MoS_2 nanosheets. It was shown that Au nanoparticles decrease the charge transfer resistance between the MoS_2 nanosheets [180]. It is also expected that the Ru nanoparticles dope the MoS_2 nanosheets improving their conductivity. Furthermore, the Ru nanoparticles provide additional active sites for hydrogen evolution. It was reported that only the edges of the MoS_2 nanosheets are active for hydrogen evolution since hydrogen atoms can't bind to the basal plane of the MoS_2 nanosheets due to the lack of dangling bonds [173]. Figure 4.6b shows the J-V curves of the MoS_2-Ru composites prepared by drop casting different amounts of MoS_2-$RuCl_2$ solution. Increasing the amount of the solution from 15 μL to 30 μL resulted in a significant improvement in the performance (the onset potential decreased from ~200 mV to ~100 mV), which can be attributed to the increased surface area. Further increase in the amount of the solution results in a performance degradation as the onset potential becomes higher (~120 mV). It appears that the thickness of the composite film is a limiting factor for the hydrogen evolution because the distance which electrons have to travel to reach to the water interface is increased causing a larger potential drop across the composite film; therefore, the potential required to start hydrogen evolution is increased. The Tafel plots of the samples are shown in Figure 4.6c. The Tafel slopes were obtained by fitting the linear portion of the plots to the Tafel equation:

$$\eta = a + b\log j,$$

where η is the overpotential, a is the exchange current density, b is the Tafel slope and j is the current density, yielding Tafel slopes of 182 mV/dec, 80 mV/dec and 53 mV/dec for

the pristine MoS_2, Ru and MoS_2-Ru composite, respectively. The smallest Tafel slope of the MoS_2-Ru composite indicates that the MoS_2-Ru exhibits superior catalytic activity over the pristine MoS_2 and pure Ru for hydrogen evolution. Lastly, we studied the stability of the MoS_2-Ru composite at a potential of -0.26 Vvs RHE over 60 minutes, in which an abrupt decrease of current density was observed initially followed by a slower decrease, resulting in an overall degradation from 55 mA/cm^2 to 10 mA/cm^2 (Figure 4.6d). The decrease of the current density is due to the dissolution of Ru into the acidic solution at high potentials followed by deposition on the surface of the Pt counter electrode, which is consistent with the observed color change of the Pt electrode.

4.4 Summary

In summary, we demonstrated a significant enhancement in the hydrogen evolution performance of the MoS_2 nanosheets with the decoration of Ru nanoparticles. The Ru nanoparticles not only provide additional active sites for hydrogen evolution but also reduce the charge transfer resistance. The highest performance was achieved for the sample fabricated by drop casting of 30 μL of the MoS_2-$RuCl_2$ solution. However, we observed performance degradation over 60 minutes due to the poor stability of the Ru nanoparticles in the H_2SO_4 solution. This study shows that adding conductive cocatalysts on the basal plane of MoS_2 nanosheets dramatically enhances the hydrogen evolution.

REFERENCES

[1] A. K. Geim, K. S. Novoselov, *Nature Materials.* **2007**, 6, 183.

[2] R. R. Nair, P. Blake, A. N. Grigorenko, K. S. Novoselov, T. J. Booth, T. Stauber, N. M. Peres, A. K. Geim, *Science.* **2008**, 320, 1308.

[3] C. Lee, X. Wei, J. W. Kysar, J. Hone, *Science.* **2008**, 321, 385.

[4] K. Novoselov, A. K. Geim, S. Morozov, D. Jiang, M. Katsnelson, I. Grigorieva, S. Dubonos, A. Firsov, *Nature.* **2005**, 438, 197.

[5] A. C. Neto, F. Guinea, N. Peres, K. S. Novoselov, A. K. Geim, *Reviews of Modern Physics.* **2009**, 81, 109.

[6] K. I. Bolotin, K. Sikes, Z. Jiang, M. Klima, G. Fudenberg, J. Hone, P. Kim, H. Stormer, *Solid State Communications.* **2008**, 146, 351.

[7] S. Kim, J. Nah, I. Jo, D. Shahrjerdi, L. Colombo, Z. Yao, E. Tutuc, S. K. Banerjee, *Applied Physics Letters.* **2009**, 94, 062107.

[8] X. Du, I. Skachko, A. Barker, E. Y. Andrei, *Nature Nanotechnology.* **2008**, 3, 491.

[9] X. Li, X. Wang, L. Zhang, S. Lee, H. Dai, *Science.* **2008**, 319, 1229.

[10] J. Bai, X. Zhong, S. Jiang, Y. Huang, X. Duan, *Nature nanotechnology.* **2010**, 5, 190.

[11] F. Schwierz, *Nature Nanotechnology.* **2010**, 5, 487.

[12] Y. Lu, B. Goldsmith, D. R. Strachan, J. H. Lim, Z. Luo, A. Johnson, *Small.* **2010**, 6, 2748.

[13] M. Wang, L. Fu, L. Gan, C. Zhang, M. Rümmeli, A. Bachmatiuk, K. Huang, Y. Fang, Z. Liu, *Scientific Reports.* **2013**, 3.

[14] L. Jiao, X. Wang, G. Diankov, H. Wang, H. Dai, *Nature Nanotechnology.* **2010**, 5, 321.

[15] K. S. Novoselov, A. K. Geim, S. V. Morozov, D. Jiang, Y. Zhang, S. V. Dubonos, I. V. Grigorieva, A. A. Firsov, *Science.* **2004**, 306, 666.

[16] Y. Lin, K. A. Jenkins, A. Valdes-Garcia, J. P. Small, D. B. Farmer, P. Avouris, *Nano Letters.* **2008**, 9, 422.

[17] C. Dean, A. Young, I. Meric, C. Lee, L. Wang, S. Sorgenfrei, K. Watanabe, T. Taniguchi, P. Kim, K. Shepard, *Nature Nanotechnology.* **2010**, 5, 722.

[18] A. Reina, X. Jia, J. Ho, D. Nezich, H. Son, V. Bulovic, M. S. Dresselhaus, J. Kong, *Nano Letters.* **2008**, 9, 30.

[19] X. Li, W. Cai, J. An, S. Kim, J. Nah, D. Yang, R. Piner, A. Velamakanni, I. Jung, E. Tutuc, S. K. Banerjee, L. Colombo, R. S. Ruoff, *Science.* **2009**, 324, 1312.

[20] S. Stankovich, D. A. Dikin, R. D. Piner, K. A. Kohlhaas, A. Kleinhammes, Y. Jia, Y. Wu, S. T. Nguyen, R. S. Ruoff, *Carbon.* **2007**, 45, 1558.

[21] X. Gao, J. Jang, S. Nagase, *The Journal of Physical Chemistry C.* **2009**, 114, 832.

[22] S. Pei, H. Cheng, *Carbon.* **2012**, 50, 3210.

[23] Y. Hernandez, V. Nicolosi, M. Lotya, F. M. Blighe, Z. Sun, S. De, I. McGovern, B. Holland, M. Byrne, Y. K. Gun'Ko, *Nature Nanotechnology.* **2008**, 3, 563.

[24] M. E. Spahr, T. Palladino, H. Wilhelm, A. Würsig, D. Goers, H. Buqa, M. Holzapfel, P. Novák, *Journal of Electrochemical Society.* **2004**, 151, A1383.

[25] C. Su, A. Lu, Y. Xu, F. Chen, A. N. Khlobystov, L. Li, *Acs Nano.* **2011**, 5, 2332.

[26] F. Schedin, A. Geim, S. Morozov, E. Hill, P. Blake, M. Katsnelson, K. Novoselov, *Nature Materials.* **2007**, 6, 652.

[27] S. Basu, P. Bhattacharyya, *Sensors and Actuators B: Chemical.* **2012**, 173, 1.

[28] H. Y. Jeong, D. Lee, H. K. Choi, D. H. Lee, J. Kim, J. Yong Lee, W. J. Lee, S. O. Kim, S. Choi, *Applied Physics Letters.* **2010**, 96, 213105.

[29] G. Ko, H. Kim, J. Ahn, Y. Park, K. Lee, J. Kim, *Current Applied Physics.* **2010**, 10, 1002.

[30] M. Gautam, A. H. Jayatissa, *Materials Science and Engineering: C.* **2011**, 31, 1405.

[31] G. Lu, L. E. Ocola, J. Chen, *Nanotechnology.* **2009**, 20, 445502.

[32] J. T. Robinson, F. K. Perkins, E. S. Snow, Z. Wei, P. E. Sheehan, *Nano Letters.* **2008**, 8, 3137.

[33] G. Lu, S. Park, K. Yu, R. S. Ruoff, L. E. Ocola, D. Rosenmann, J. Chen, *ACS Nano.* **2011**, 5, 1154.

[34] V. Dua, S. P. Surwade, S. Ammu, S. R. Agnihotra, S. Jain, K. E. Roberts, S. Park, R. S. Ruoff, S. K. Manohar, *Angewandte Chemie International Edition.* **2010**, 49, 2154.

[35] W. Wu, Z. Liu, L. A. Jauregui, Q. Yu, R. Pillai, H. Cao, J. Bao, Y. P. Chen, S. Pei, *Sensors and Actuators B: Chemical.* **2010**, 150, 296.

[36] M. G. Chung, D. Kim, D. K. Seo, T. Kim, H. U. Im, H. M. Lee, J. Yoo, S. Hong, T. J. Kang, Y. H. Kim, *Sensors and Actuators B: Chemical.* **2012**, 169, 387.

[37] P. A. Russo, N. Donato, S. G. Leonardi, S. Baek, D. E. Conte, G. Neri, N. Pinna, *Angewandte Chemie International Edition.* **2012**, 51, 11053.

[38] J. Qin, M. Cao, N. Li, C. Hu, *Journal of Materials Chemistry.* **2011**, 21, 17167.

[39] F. Yavari, Z. Chen, A. V. Thomas, W. Ren, H. Cheng, N. Koratkar, *Scientific Reports.* **2011**, 1.

[40] K. Yu, Z. Bo, G. Lu, S. Mao, S. Cui, Y. Zhu, X. Chen, R. S. Ruoff, J. Chen, *Nanoscale Research Letters.* **2011**, 6, 1.

[41] B. Huang, Z. Li, Z. Liu, G. Zhou, S. Hao, J. Wu, B. Gu, W. Duan, *The Journal of Physical Chemistry C.* **2008**, 112, 13442.

[42] R. K. Paul, S. Badhulika, N. M. Saucedo, A. Mulchandani, *Analytical Chemistry.* **2012**, 84, 8171.

[43] D. Leduc, P. Gris, P. Lheureux, P. A. Gevenois, P. De Vuyst, J. C. Yernault, *Thorax.* **1992**, 47, 755.

[44] J. I. Steinfeld, J. Wormhoudt, *Annual Review of Physical Chemistry.* **1998**, 49, 203.

[45] A. D. Aguilar, E. S. Forzani, L. A. Nagahara, I. Amlani, R. Tsui, N. Tao, *Sensors Journal, IEEE.* **2008**, 8, 269.

[46] A. Ferrari, J. Meyer, V. Scardaci, C. Casiraghi, M. Lazzeri, F. Mauri, S. Piscanec, D. Jiang, K. Novoselov, S. Roth, *Physical Review Letters.* **2006**, 97, 187401.

[47] Z. Shi, R. Yang, L. Zhang, Y. Wang, D. Liu, D. Shi, E. Wang, G. Zhang, *Advanced Materials.* **2011**, 23, 3061.

[48] D. Graf, F. Molitor, K. Ensslin, C. Stampfer, A. Jungen, C. Hierold, L. Wirtz, *Nano Letters.* **2007**, 7, 238.

[49] X. Wang, Y. Ouyang, X. Li, H. Wang, J. Guo, H. Dai, *Physical Review Letters.* **2008**, 100, 206803.

[50] Z. Zanolli, J. Charlier, *Physical Review B.* **2009**, 80, 155447.

[51] B. Karunagaran, P. Uthirakumar, S. Chung, S. Velumani, E. Suh, *Materials Characterization.* **2007**, 58, 680.

[52] D. Eastman, *Physical Review B.* **1970**, 2, 1.

[53] Q. Yan, B. Huang, J. Yu, F. Zheng, J. Zang, J. Wu, B. Gu, F. Liu, W. Duan, *Nano Letters.* **2007**, 7, 1469.

[54] C. V. Thompson, *Annual Review of Materials Research.* **2012**, 42, 399.

[55] J. Kwon, T. Yoon, K. Kim, S. Min, *Journal of Applied Physics.* **2003**, 93, 3270.

[56] G. Paulson, A. Friedberg, *Thin Solid Films.* **1970**, 5, 47.

[57] D. J. Srolovitz, M. G. Goldiner, *JOM.* **1995**, 47, 31.

[58] J. Petersen, S. Mayr, *Journal of Applied Physics.* **2008**, 103, 023520.

[59] E. Bussmann, F. Cheynis, F. Leroy, P. Müller, O. Pierre-Louis, *New Journal of Physics.* **2011**, 13, 043017.

[60] A. Geissler, M. He, J. Benoit, P. Petit, *The Journal of Physical Chemistry C.* **2009**, 114, 89.

[61] L. G. Cançado, A. Jorio, E. M. Ferreira, F. Stavale, C. Achete, R. Capaz, M. Moutinho, A. Lombardo, T. Kulmala, A. Ferrari, *Nano Letters.* **2011**, 11, 3190.

[62] A. Das, S. Pisana, B. Chakraborty, S. Piscanec, S. Saha, U. Waghmare, K. Novoselov, H. Krishnamurthy, A. Geim, A. Ferrari, *Nature Nanotechnology.* **2008**, 3, 210.

[63] X. Dong, D. Fu, W. Fang, Y. Shi, P. Chen, L. Li, *Small.* **2009**, 5, 1422.

[64] J. G. Son, M. Son, K. Moon, B. H. Lee, J. Myoung, M. S. Strano, M. Ham, C. A. Ross, *Advenced Materials.* **2013**, 25, 4723.

[65] V. Barone, O. Hod, G. E. Scuseria, *Nano Letters.* **2006**, 6, 2748.

[66] L. Boon-Brett, J. Bousek, G. Black, P. Moretto, P. Castello, T. Hübert, U. Banach, *International Journal of Hydrogen Energy.* **2010**, *35*, 373.

[67] W. J. Buttner, M. B. Post, R. Burgess, C. Rivkin, *International Journal of Hydrogen Energy.* **2011**, *36*, 2462.

[68] G. Lu, N. Miura and N. Yamazoe, *Sensors and Actuators B: Chemical.* 1996, **35**, 130.

[69] O. K. Varghese, D. Gong, M. Paulose, K. G. Ong and C. A. Grimes, *Sensors and Actuators B: Chemical.* 2003, **93**, 338.

[70] S. Shukla, S. Patil, S. Kuiry, Z. Rahman, T. Du, L. Ludwig, C. Parish and S. Seal, *Sensors and Actuators B: Chemical.* 2003, **96**, 343.

[71] R. K. Joshi, S. Krishnan, M. Yoshimura and A. Kumar, *Nanoscale Research Letters.* 2009, **4**, 1191.

[72] Y. Im, C. Lee, R. P. Vasquez, M. A. Bangar, N. V. Myung, E. J. Menke, R. M. Penner and M. Yun, *Small.* 2006, **2**, 356.

[73] R. Hughes, W. Schubert, T. Zipperian, J. Rodriguez and T. Plut, *Journal of Applied Physics.* 1987, **62**, 1074.

[74] M. G. Chung, D. Kim, D. K. Seo, T. Kim, H. U. Im, H. M. Lee, J. Yoo, S. Hong, T. J. Kang and Y. H. Kim *Sensors and Actuators B: Chemical.* 2012, **169**, 387.

[75] W. Wu, Z. Liu, L. A. Jauregui, Q. Yu, R. Pillai, H. Cao, J. Bao, Y. P. Chen and S. Pei, *Sensors and Actuators B: Chemical* .2010, **150**, 296.

[76] Z. Chen, J. Jie, L. Luo, H. Wang, C. Lee and S. Lee, *Nanotechnology.* 2007, **18**, 345502.

[77] Y. Sun and H. H. Wang, *Advanced Matererials.* 2007, **19**, 2818.

[78] S. Mubeen, T. Zhang, B. Yoo, M. A. Deshusses and N. V. Myung, *Journal of Physical Chemistry C.* 2007, **111**, 6321.

[79] K. S. Novoselov, A. K. Geim, S. V. Morozov, D. Jiang, Y. Zhang, S. V. Dubonos, I. V. Grigorieva, A. A. Firsov, *Science.* **2004**, *306*, 666.

[80] H. Ramakrishna Matte, A. Gomathi, A. K. Manna, D. J. Late, R. Datta, S. K. Pati, C. Rao, *Angewandte Chemie.* **2010**, *122*, 4153.

[81] Y. Lee, X. Zhang, W. Zhang, M. Chang, C. Lin, K. Chang, Y. Yu, J. T. Wang, C. Chang, L. Li, *Advanced Materials.* **2012**, *24*, 2320.

[82] W. Li, X. Geng, Y. Guo, J. Rong, Y. Gong, L. Wu, X. Zhang, P. Li, J. Xu, G. Cheng, *ACS Nano.* **2011**, *5*, 6955.

[83] H. E. Romero, P. Joshi, A. K. Gupta, H. R. Gutierrez, M. W. Cole, S. A. Tadigadapa, P. C. Eklund, *Nanotechnology.* **2009**, *20*, 245501.

[84] G. Lu, L. E. Ocola, J. Chen, *Nanotechnology.* **2009**, *20*, 445502.

[85] M. G. Chung, D. H. Kim, H. M. Lee, T. Kim, J. H. Choi, J. Yoo, S. Hong, T. J. Kang, Y. H. Kim, *Sensors and Actuators B: Chemical***. 2012**, *166*, 172.

[86] A. Gut´es, B. Hsia, A. Sussman, W. Mickelson, A. Zettl, C. Carraro, R. Maboudian, *Nanoscale.* **2012**, *4*, 438.

[87] H. Vedala, D. C. Sorescu, G. P. Kotchey, A. Star, *Nano Letters.* **2011**, *11*, 2342.

[88] W. Wu, Z. Liu, L. A. Jauregui, Q. Yu, R. Pillai, H. Cao, J. Bao, Y. P. Chen, S. Pei, *Sensors and Actuators B: Chemical.* **2010**, *150*, 296.

[89] M. G. Chung, D. Kim, D. K. Seo, T. Kim, H. U. Im, H. M. Lee, J. Yoo, S. Hong, T. J. Kang, Y. H. Kim, *Sensors and Actuators B: Chemical.* **2012**, *169*, 387.

[90] K. F. Mak, C. Lee, J. Hone, J. Shan, T. F. Heinz, *Physical Review Letters.* **2010**, *105*, 136805.

[91] B. Radisavljevic, A. Radenovic, J. Brivio, V. Giacometti, A. Kis, *Nature Nanotechnology.* **2011**, *6*, 147.

[92] G. Eda, H. Yamaguchi, D. Voiry, T. Fujita, M. Chen, M. Chhowalla, *Nano Letters.* **2011**, *11*, 5111.

[93] Z. Yin, H. Li, H. Li, L. Jiang, Y. Shi, Y. Sun, G. Lu, Q. Zhang, X. Chen, H. Zhang, *ACS Nano.* **2011**, *6*, 74.

[94] Y. Zhan, Z. Liu, S. Najmaei, P. M. Ajayan, J. Lou, *Small.* **2012**, *8*, 966.

[95] J. Xiao, D. Choi, L. Cosimbescu, P. Koech, J. Liu, J. P. Lemmon, *Chemistry of Materials.* **2010**, *22*, 4522.

[96] F. K. Perkins, A. L. Friedman, E. Cobas, P. Campbell, G. Jernigan, B. T. Jonker, *Nano Letters.* **2013**, *13*, 668.

[97] K. Lee, R. Gatensby, N. McEvoy, T. Hallam, G. S. Duesberg, *Advanced Materials.* **2013**, *25*, 6699.

[98] M. B. Dines, *Materials Research Bulletin.* **1975**, *10*, 287.

[99] V. Pachauri, K. Kern, K. Balasubramanian, *APL. Materials.* **2013**, *1*, 032102.

[100] U. Khan, A. O'Neill, M. Lotya, S. De, J. N. Coleman, *Small.* **2010**, *6*, 864.

[101] J. N. Coleman, M. Lotya, A. O'Neill, S. D. Bergin, P. J. King, U. Khan, K. Young, A. Gaucher, S. De, R. J. Smith, I. V. Shvets, S. K. Arora, G. Stanton, H. Y. Kim, K. Lee, G. T. Kim, G. S. Duesberg, T. Hallam, J. J. Boland, J. J. Wang, J. F. Donegan, J. C. Grunlan, G. Moriarty, A. Shmeliov, R. J. Nicholls, J. M. Perkins, E. M. Grieveson, K. Theuwissen, D. W. McComb, P. D. Nellist, V. Nicolosi, *Science.* **2011**, *331*, 568.

[102] A. O'Neill, U. Khan, J. N. Coleman, *Chemistry of Materials.* **2012**, *24*, 2414.

[103] B. Radisavljevic, A. Radenovic, J. Brivio, V. Giacometti, A. Kis, *Nature Nanotechnology.* **2011**, *6*, 147.

[104] V. Štengl, J. Henych, *Nanoscale.* **2013**, *5*, 3387.

[105] D. Gopalakrishnan, D. Damien, M. M. Shaijumon, *ACS Nano.* **2014**, *8*, 5297.

[106] N. Liu, P. Kim, J. H. Kim, J. H. Ye, S. Kim, C. J. Lee, *ACS Nano.* **2014**, *8*, 6902.

[107] H. Li, Q. Zhang, C. C. R. Yap, B. K. Tay, T. H. T. Edwin, A. Olivier, D. Baillargeat, *Advanced Functional Materials.* **2012**, *22*, 1385.

[108] Z. H. Ni, H. M. Wang, Z. Q. Luo, Y. Y. Wang, T. Yu, Y. H. Wu, Z. X. Shen, *Journal of Raman Spectroscopy.* **2010**, *41*, 479.

[109] Y. Sun, H. H. Wang, *Advanced Materials.* **2007**, *19*, 2818.

[110] B. D. Kay, C. H. Peden, D. W. Goodman, *Physical Review B.* **1986**, *34*, 817.

[111] P. A. Pandey, N. R. Wilson, J. Covington, *Sensors and Actuators B: Chemical.* **2013**, *183*, 478.

[112] R. Kumar, D. Varandani, B. Mehta, V. Singh, Z. Wen, X. Feng, K. Müllen, *Nanotechnology.* **2011**, *22*, 275719.

[113] H. B. Michaelson, *Journal of Applied Physics.* **1977**, *48*, 4729.

[114] Y. Wong, W. Kang, J. Davidson, A. Wisitsora-At, K. Soh, *Sensors and Actuators B: Chemical.* **2003**, *93*, 327.

[115] J. Yun, Y. Noh, J. Yeo, Y. Go, S. Na, H. Jeong, J. Kim, S. Lee, S. Kim, H. Y. Koo, *Journal of Materials Chemistry C.* **2013**, *1*, 3777.

[116] Y. Li, C. Xu, L. Zhen, **2013**, *Nanophotonics, Nanoelectronics and Nanosensor*. 09.

[117] M. Chhowalla, H. S. Shin, G. Eda, L. Li, K. P. Loh and H. Zhang, *Nature Chemistry.* 2013, **5**, 263.

[118] H. R. Gutiérrez, N. Perea-López, A. L. Elías, A. Berkdemir, B. Wang, R. Lv, F. López-Urías, V. H. Crespi, H. Terrones and M. Terrones, *Nano Letters.* 2012, **13**, 3447.

[119] M. A. Lukowski, A. S. Daniel, C. R. English, F. Meng, A. Forticaux, R. J. Hamers and S. Jin, *Energy and Environmental Science.* 2014, **7**, 2608.

[120] T. Sreeprasad, P. Nguyen, N. Kim and V. Berry, *Nano Letters.* 2013, **13**, 4434.

[121] A. Molina-Sanchez and L. Wirtz, *Physical Review B.* 2011, **84**, 155413.

[122] A. Berkdemir, H. R. Gutiérrez, A. R. Botello-Méndez, N. Perea-López, A. L. Elías, C. Chia, B. Wang, V. H. Crespi, F. López-Urías and J. Charlier, *Scientific Reports.* 2013, **3,** 1755.

[123] M. Ahn, K. Park, J. Heo, J. Park, D. Kim, K. J. Choi, J. Lee and S. Hong, *Applied Physics Letters.* 2008, **93**, 263103.

[124] M. C. Steele, J. W. Hile and B. A. MacIver, *Journal of Applied Physics* 1976, **47**, 2537.

[125] S. Trasatti, *Journal of Electroanalitical Chemistry and Interfacial Electrochemistry* . 1971, **33**, 351.

[126] C. S. Rout, P. D. Joshi, R. V. Kashid, D. S. Joag, M. A. More, A. J. Simbeck, M. Washington, S. K. Nayak and D. J. Late, *Scientific Reports.* 2013, **3**.

[127] K. Lundström, M. Shivaraman and C. Svensson, *Journal of Applied Physics.* 1975, **46**, 3876.

[128] C. Sachs, A. Pundt, R. Kirchheim, M. Winter, M. Reetz and D. Fritsch, *Physical Review B.* 2001, **64**, 075408.

[129] Y. Sun, H. H. Wang and M. Xia, *Journal of Physical Chemistry C.* 2008, **112**, 1250.

[130] Y. Jia, P. Li, X. Gui, J. Wei, K. Wang, H. Zhu, D. Wu, L. Zhang, A. Cao and Y. Xu, *Applied Physics Letters*. 2011, **98**, 133115.

[131] Y. Jung, X. Li, N. K. Rajan, A. D. Taylor and M. A. Reed, *Nano Letters*. 2012, 13, 95.

[132] E. Shi, L. Zhang, Z. Li, P. Li, Y. Shang, Y. Jia, J. Wei, K. Wang, H. Zhu and D. Wu, *Nano Letters*. 2013 **13**, 1776.

[133] Y. Jia, A. Cao, X. Bai, Z. Li, L. Zhang, N. Guo, J. Wei, K. Wang, H. Zhu and D. Wu, *Nano Letters*. 2011, **11**, 1901.

[134] K. S. Novoselov, A. K. Geim, S. V. Morozov, D. Jiang, Y. Zhang, S. V. Dubonos, I. V. Grigorieva and A. A. Firsov, *Science*. 2004, **306**, 666.

[135] X. Li, H. Zhu, K. Wang, A. Cao, J. Wei, C. Li, Y. Jia, Z. Li, X. Li and D. Wu, *Advanced Materials*. 2010, **22**, 2743.

[136] Y. Lin, X. Li, D. Xie, T. Feng, Y. Chen, R. Song, H. Tian, T. Ren, M. Zhong and K. Wang, *Energy and Environmental Science.* 2013, **6**, 108.

[137] Y. F. Li, W. Yang, Z. Q. Tu, Z. C. Liu, F. Yang, L. Q. Zhang and R. Hatakeyama, *Applied Physics Letters*. 2014, **104**, 043903.

[138] C. Xie, X. Zhang, Y. Wu, X. Zhang, X. Zhang, Y. Wang, W. Zhang, P. Gao, Y. Han and J. Jie, *Journal of Materials Chemistry A*. 2013, **1**, 8567.

[139] V. V. Brus, M. A. Gluba, X. Zhang, K. Hinrichs, J. Rappich and N. H. Nickel, *Physica Status Solidi (a)*. 2014, **211**, 843.

[140] T. Cui, R. Lv, Z. Huang, S. Chen, Z. Zhang, X. Gan, Y. Jia, X. Li, K. Wang and D. Wu, *Journal of Materials Chemistry A*. 2013, **1**, 5736.

[141] T. Helená Zeng, *Nanoscale.* 2013, **5**, 1945.

[142] C. Xie, P. Lv, B. Nie, J. Jie, X. Zhang, Z. Wang, P. Jiang, Z. Hu, L. Luo and Z. Zhu, *Applied Physics Letters*. 2011, **99**, 133113.

[143] T. Feng, D. Xie, Y. Lin, H. Zhao, Y. Chen, H. Tian, T. Ren, X. Li, Z. Li and K. Wang, *Nanoscale*. 2012, **4**, 2130.

[144] H. A. Atwater and A. Polman, *Nature Materials,* 2010, **9**, 205.

[145] S. Pillai, K. Catchpole, T. Trupke and M. Green, *Journal of Applied Physics.* 2007, **101**, 093105.

[146] G. L. Araujo and E. Sanchez, *IEEE Transactions on Electron Devices.* 1982, **29**, 1511.

[147] C. A. Dimitriadis, S. Logothetidis and I. Alexandrou, *Applied Physics Letters*. 1995, **66**, 502.

[148] S. K. Cheung and N. W. Cheung, *Applied Physics Letters*. 1986, **49**, 85.

[149] E. Shi, H. Li, L. Yang, L. Zhang, Z. Li, P. Li, Y. Shang, S. Wu, X. Li and J. Wei, *Nano Letters,* 2013, **13**, 1776.

[150] M. A. Green and M. J. Keevers, *Progress in Photovoltaics: Research and Applications,* 1995, **3**, 189.

[151] J. Cariou, J. Dugas, L. Martin and P. Michel, *Applied Optoelectronics.* 1986, **25**, 334.

[152] R. Li, J. Di, Z. Yong, B. Sun and Q. Li, *Journal of Materials Chemistry A,* 2014, **2**, 4140.

[153] L. Lancellotti, E. Bobeico, A. Capasso, M. Della Noce, T. Dikonimos, N. Lisi and P. Delli Veneri, *Photonics Technologies, 2014 Fotonica AEIT Italian Conference*. *IEEE*. 2014, **1**.

[154] X. Miao, S. Tongay, M. K. Petterson, K. Berke, A. G. Rinzler, B. R. Appleton and A. F. Hebard, *Nano Letters*. 2012, **12**, 2745.

[155] N. Sun, G. Fang, P. Qin, Q. Zheng, M. Wang, X. Fan, F. Cheng, J. Wan, X. Zhao and J. Liu, *Journal of Physics D*. 2010, **43**, 445101.

[156] H. Yang, C. Gong, G. Hong Guai and C. Ming Li, *Solar Energy Materials and Solar Cells*. 2012, **101**, 256.

[157] A. C. Ferrari, *Solid State Communications*. 2007, **143**, 47.

[158] L. G. Cançado, A. Jorio, E. M. Ferreira, F. Stavale, C. A. Achete, R. B. Capaz, M. Moutinho, A. Lombardo, T. S. Kulmala and A. C. Ferrari, *Nano Letters*. 2011, **11**, 3190.

[159] D. Graf, F. Molitor, K. Ensslin, C. Stampfer, A. Jungen, C. Hierold and L. Wirtz, *Nano Letters.* 2007, **7**, 238.

[160] M. Taguchi, S. Takami, T. Naka and T. Adschiri, *Crystal Growth and Design.* 2009, **9**, 5297.

[161] I. Chan, T. Hsu and F. C. Hong, *Applied Physics Letters*. 2002, **81**, 1899.

[162] B. Wei, S. Yamamoto, M. Ichikawa, C. Li, T. Fukuda and Y. Taniguchi, *Semiconductor Science and Technology*. 2007, **22**, 788.

[163] J. S. Anderson and D. F. Klemperer, *Proceedings of Royal Society of London A: Mathematical, Physical and Engineering Sciences.* 1960, **258**, 350.

[164] C. Christodoulou, A. Giannakopoulos, M. V. Nardi, G. Ligorio, M. Oehzelt, L. Chen, L. Pasquali, M. Timpel, A. Giglia and S. Nannarone, *Journal of Physical Chemistry C*. 2014, **118**, 4784.

[165] S. Baykara, *Int J Hydrogen Energy.* **2004**, 29, 1459.

[166] Global energy consumption in 2013. Retrieved from http://www.euanmearns.com/wp-content/uploads/2014/06/global_energy_2013.png.

[167] Y. Chang, F. Wu, T. Chen, C. Hsu, C. Chen, F. Wiryo, K. Wei, C. Chiang, L. Li, *Small.* **2014**, 10, 895.

[168] Y. Chen, Y. Wang, H. Xu, G. Xiong, *Applied Catalysis B: Environmental.* **2008**, 81, 283.

[169] G. W. Crabtree, M. S. Dresselhaus, M. V. Buchanan, *Phys Today.* **2004**, 57, 39.

[170] P. Du, R. Eisenberg, *Energy & Environmental Science.* **2012**, 5, 6012.

[171] B. Hinnemann, P. G. Moses, J. Bonde, K. P. Jørgensen, J. H. Nielsen, S. Horch, I. Chorkendorff, J. K. Nørskov, *J. Am. Chem. Soc.* **2005**, 127, 5308.

[172] T. F. Jaramillo, K. P. Jorgensen, J. Bonde, J. H. Nielsen, S. Horch, I. Chorkendorff, *Science.* **2007**, 317, 100.

[173] A. Kudo, Y. Miseki, *Chem. Soc. Rev.* **2009**, 38, 253.

[174] Y. Li, H. Wang, L. Xie, Y. Liang, G. Hong, H. Dai, *J. Am. Chem. Soc.* **2011**, 133, 7296.

[175] K. Maeda, K. Domen, *The Journal of Physical Chemistry Letters.* **2010**, 1, 2655.

[176] J. Rossmeisl, Z. Qu, H. Zhu, G. Kroes, J. K. Nørskov, *J Electroanal Chem.* **2007**, 607, 83.

[177] D. Voiry, M. Salehi, R. Silva, T. Fujita, M. Chen, T. Asefa, V. B. Shenoy, G. Eda, M. Chhowalla, *Nano letters.* **2013**, 13, 6222.

[178] Y. Zhao, X. Xie, J. Zhang, H. Liu, H. Ahn, K. Sun, G. Wang, *Chemistry–A European Journal.* **2015**, 21, 15908.

[179] R. Saito, Y. Miseki, K. Sayama, *Chemical Communications.* **2012**, 48, 3833.

[180] J. Kim, S. Byun, A. J. Smith, J. Yu, J. Huang, *The Journal of Physical Chemistry Letters.* **2013**, 4, 1227.